

Diss. ETH No. 22053

ON HARVESTING, CONFINEMENT
AND CONVERSION
OF THE ENERGY OF LIGHT
WITH FACILE PLASMONIC
NANOSTRUCTURES

A dissertation submitted to
ETH ZURICH

for the degree
DOCTOR OF SCIENCES

presented by

Giulia Tagliabue

MSc. Mech. Eng. University of Udine

born June 21, 1985
citizen of Italy

accepted on the recommendation of

Prof. Dr. Dimos Poulikakos, examiner

Prof. Dr. Aldo Steinfeld, co-examiner

Dr. Hadi Eghlidi, co-examiner

2014

Document typeset by the author using L^AT_EX 2_ε with the document class `book`. Figures were prepared with Matlab and Adobe Illustrator.

©Giulia Tagliabue, Zurich (2014).

*To my grandfather,
who would have enjoyed listening to this story*

Padova, 1610

Sagredo: So wäre kein Unterschied zwischen Mond und Erde?

Galilei: Offenbar nein.

Sagredo: Vor noch nicht zehn Jahren ist ein Mensch in Rom verbrannt worden. Er hieß Giordano Bruno und hatte eben das behauptet.

Galilei: Gewiß. Und wir sehen es. Laß dein Auge am Rohr, Sagredo. Was du siehst, ist, daß es keinen Unterschied zwischen Himmel und Erde gibt. Heute ist der 10 Januar 1610. Die Menschheit trägt in ihr Journal ein: Himmel abgeschafft.

Sagredo: Das ist furchtbar.

Bertold Brecht,
Das Leben des Galilei

Abstract

Efficient light harvesting and confinement in deeply sub-wavelength dimensions is very challenging but offers simultaneously exciting possibilities which can impact a variety of important applications from biological sample analysis to electronic circuits and to solar energy harvesting technologies. Indeed, light interaction with ultra-thin or nano-sized objects is inherently poor and it constitutes the bottleneck for the miniaturization of many devices. In recent years metallic nano-structures supporting surface plasmons have been proposed as a viable solution to this problem. In fact, they have been shown to enable effective coupling, focusing and manipulation of light at the nanoscale, finally overcoming the diffraction limit.

Light-conversion technologies, such as photovoltaic, solar-thermoelectric and photocatalytic cells, would highly benefit from a nearly ideal light harvesting in ultra-thin structures due to the associated decrease in material costs and increase in efficiencies. Nevertheless, sunlight harvesting poses several challenges to the design of plasmonics-based structures due to its broad-spectrum and variable angle of incidence. In the first part of this thesis (Chapter 3) we addressed these aspects by investigating, designing and fabricating a facile, ultra-thin (260 nm) plasmonic sunlight absorber which is capable of harvesting on average 88 % of the Sun energy in the spectral range 380 – 980 nm. Our approach is inherently polarization insensitive and preserves its performances for incident angles up to 48° . In addition, the fabrication of our structure is compatible with large-scale, roll-to-roll processes and the used multilayer design could be easily implemented in a real devices where additional functionalities (e.g. electrical access) are required.

Light collection is only the first step toward light-energy exploitation and in the second part of the thesis (Chapters 4 – 5) we thus focused on extreme confinement of the collected light. We performed a general study on a class of plasmonic multilayer (metal-insulator-metal) structures, with a dielectric spacer of only few nanometers (7 – 13 nm). As front pattern we used facile hexagonal arrays of tapered gold triangles which eventually connect forming an electrically communicating network. We show that, in the disconnected

0. Abstract

condition, every single element of the array is almost completely isolated from the neighboring ones, light being tightly confined in the dielectric layer underneath each tapered triangle. In the connected configuration, an even more extreme confinement can be achieved locally. Indeed, exploiting the non-uniform lateral width of the considered front metal layer and the symmetric arrangement, we prove that light can be guided and confined in a nanocavity whose physical area is almost 20 times smaller than its optical area.

Following the above, in the last two Chapters, we investigate two important light-energy conversion processes: light-to-heat and light-to-hot electron conversion, to be exploited in thermoelectric (e.g. radiation sensors) and photocatalytic applications respectively. In Chapter 6, after fabricating a broadband absorber as a 10 nm free standing membrane, we performed infrared thermography measurements and determined its thermal response. We showed that, due to the ultra-low thickness, the plasmonic absorber has a characteristic time of less than 13 ns, more than one of magnitude faster than a comparable system based on an absorbing black spray. Finally, in Chapter 7, we used x-ray spectroscopy to measure in-situ the change in the density of states of gold nanoparticles during the excitation of a plasmonic resonance and showed that a significant 1 eV shift in the Fermi level occurs. This result confirms the great potential of plasmonic nanostructures to act as sensitizers, not only improving light collection, but actively contributing to the increased performance of a catalyst.

Sommario

Assorbire e focalizzare la luce in modo efficiente in volumi di dimensioni molto piu' piccole della lunghezza d'onda è una grande sfida che al tempo stesso offre allettanti prospettive per la variet di importanti applicazioni che potrebbero beneficiarne, dall'analisi di campioni biologici ai circuiti elettronici alle tecnologie solari per la produzione di energia. Tuttavia, l'interazione della luce con oggetti ultra-sottili o nanoscopici è molto limitata e costituisce il fattore limitante verso la miniaturizzazione di molti dispositivi. Recentemente l'uso di nano-strutture metalliche capaci di sostenere risonanze plasmoniche è stato proposto come una soluzione percorribile per questo problema. Infatti è stato dimostrato che queste strutture sono in grado di oltrepassare il limite di diffrazione, permettendo un'efficace interazione, focalizzazione e manipolazione della luce alla nano-scala.

Tecnologie come le celle fotovoltaiche, il solare termoelettrico e le celle fotocatalitiche trarrebbero grande beneficio dalla possibilità di un assorbimento quasi perfetto della luce solare tramite strutture ultra-sottili, grazie alle conseguenti riduzioni dei costi dei materiali e all'aumento delle prestazioni. Tuttavia, l'assorbimento della luce solare tramite strutture plasmoniche è problematico a causa dell'ampio contenuto in lunghezze d'onda e della variabilità dell'angolo di incidenza. Nella prima parte di questa tesi (Capitolo 3) abbiamo affrontato questi aspetti, studiando, progettando e realizzando un assorbitore solare plasmonico semplice e ultra-sottile, capace di assorbire in media l'88% dell'energia solare nell'intervallo di lunghezze d'onda 380 – 980 nm. Inoltre, la nostra struttura è insensibile allo stato di polarizzazione della luce e mantiene pressoché inalterate le proprie prestazioni per angoli di incidenza fino a 48°. Per di più, il processo di fabbricazione è compatibile con procedure di larga scala come quelle *roll-to-roll* e l'utilizzo di una struttura multistrato rende il design compatibile con un vero dispositivo dove altre funzionalità (ad esempio l'accesso elettrico) sono richieste.

L'assorbimento della luce è solo il primo passo verso l'utilizzo effettivo della sua energia e nella seconda parte della tesi (Capitoli 4 – 5) ci siamo focalizzati sulla concentrazione della luce assorbita. Abbiamo infatti effettuato uno

0. Sommario

studio piu' generale su di una classe di strutture plasmoniche multistrato (metallo-isolante-metallo) caratterizzate da un dielettrico spesso solo pochi nanometri (7 – 13 nm). Come struttura frontale, abbiamo utilizzato un arrangiamento periodico esagonale di triangoli d'oro curvi le cui dimensioni venivano variate fino ad ottenere un contatto, formando cosi' una rete elettricamente conduttiva. Abbiamo cosi' mostrato come, nel caso di strutture separate, la luce venga fortemente confinata nel materiale dielettrico al di sotto di ogni single triangolo. Nella configurazione connessa, stato possibile ottenere un effetto di concentrazione anche maggiore. Infatti, sfruttando la non-uniformita della sezione laterale dello strato frontale, possibile guidare la luce e confinarla in una nano-cavita' le cui dimensioni fisiche sono 20 volte inferiori a quelle ottiche.

Come continuazione del lavoro precedente, negli ultimi due capitoli, abbiamo studiato due importanti processi di conversione dell'energia della luce: da un lato la conversione in calore e dall'altro la conversione in elettroni energetici, processi che potrebbero essere sfruttati in elementi termoelettrici (ad esempio sensori di radiazione) o applicazioni fotocatalitiche, rispettivamente. Nel Capitolo 6, abbiamo eseguito delle misure di temperatura con una telecamera ad infrarossi determinando la risposta termica di un assorbitore plasmonico che avevamo precedentemente fabbricato come membrana. Abbiamo mostrato come, grazie al ridottissimo spessore, questo assorbitore abbia un tempo caratteristico di risposta di soli 13 ms, inferiore di piu' di un ordine di grandezza rispetto a un sistema equivalente basato su di uno spray nero. Infine, nel Capitolo 7, abbiamo utilizzato la spettroscopia a raggi x per determinare il cambiamento della densita degli stati in nano-particelle d'oro soggette all'eccitazione di una risonanza plasmonica e abbiamo mostrato che il livello di energia di Fermi viene innalzato di circa 1 eV. Questo risultato conferma il grande potenziale delle strutture plasmoniche di agire da *sensitizer*, non solo migliorando l'assorbimento della luce, ma partecipando in modo attivo al miglioramento delle prestazioni del catalizzatore.

Acknowledgements

First and foremost, I would like to express my most sincere gratitude to Professor Poulidakos for accepting me in his lab and supporting me at all moments throughout this long PhD journey. His unwavering confidence in me getting to the end of this work has been of great help in the troubled times of non-working experiments, failed attempts and rejected papers.

Special thanks to Hadi Eghlidi who gave an invaluable contribution to this thesis, guiding me in the last couple of years and sharing both successes and defeats in this time. Your expertise, patience and rigor have been fundamental for the progress of this work. Indeed, our long and sometimes harsh discussions always lead to a significant improvement of the result. Thanks for sharing your knowledge and your time with me, I did enjoy it and I am grateful to you.

Many thanks to Jacinto Sa' for the enthusiasm with which he got involved and then lead the plasmonic-catalysis work. Without your tireless efforts and perseverance it wouldn't have been possible to bring it to an end. I really enjoyed talking with you about anything, from science to politics, and I must thank you for explaining me so many things about chemistry and x-ray spectroscopy.

I would also like to thank Professor Steinfeld for his support and for being my co-supervisor.

Thanks also to Majid Nabavi who supervised me at the beginning of the project, initiating me to the nano-fabrication world and to Jakub Szlachetko, who performed the synchrotron measurements.

Thanks to Adrienne Nelson and Lucio Isa for helping me with the tedious dip-coating procedures. Moreover, thanks to Susanne Droescher for giving me the possibility to pursue a real application of my work.

Moreover, thanks to the students who directly worked with me, Olivier, Thomas, Leander, Christian, Carmen and Patrick, and to different staff people of ETH, Bruno Kramer, Daniel Jans and the whole staff of FIRST.

This PhD would have been much more difficult without the support of my colleagues, friends and family.

0. Acknowledgements

Therefore, a global thank to the entire LTNT group where everyone really contributes in creating a relaxing and constructive environment which makes the working days much easier. I cannot-not reserve a special mention to those people who shared endless coffee breaks (and even longer post-coffee-break chats) with me, my rock-stars-friends Daniele and Simone, who always found a good word to cheer me up and drove me crazy talking about Italian politics. Thanks also to the other member of the Guatemala trip, Alejandro and Davide as well as my office mates, above all Farhad, with whom I shared my days for nearly 4 years, and also Julian and Ying. Thanks also to Sandra, Nada (earlier) and Patrizia (later) for the LTNT-women-lunch and for attempting to speak German with me. I count on this interconnected world to hear all of your voices from time to time, wherever we will be.

Leaving ETH, I would like to thank my friend Sepideh for the unfortunately rare but intense reunions and for the delicious food that always accompanies our dinners. I really miss our Rhodanie's daily routine.

Thanks to Daniele and Stefania for sharing so many experiences and so much food in the last two years. Our home will be always your home.

Almost at the end, vorrei ringraziare i miei genitori e tutta la mia famiglia per essermi stati sempre vicini ed avermi spronato in questi quattro anni ed in tutti quelli precedenti; questo dottorato e' un traguardo che arriva da molto lontano. Grazie anche per sopportare la mia lontananza.

Last but for sure not least, thanks to my soul-mate, Pablo, because there are no words to reward you for your infinite patience and for being at my side at all times.

Contents

Abstract	ix
Sommario	xi
Acknowledgements	xiii
1 Introduction	1
1.1 Thesis Outline	3
2 Fundamentals	5
2.1 Plasmons	5
2.2 Surface Plasmons Polaritons	6
2.2.1 Dispersion Curve for a Single Interface	6
2.2.2 Multiple Interfaces and Mode Splitting	9
2.2.3 Effective Refractive Index and Nanofocusing	11
2.2.4 Gap Plasmons in Truncated MIM Structures	12
2.3 Localized surface plasmons	13
2.3.1 Absorption and Scattering Cross Sections	13
2.3.2 Coupling between Nanostructures	15
3 Facile Multifunctional Plasmonic Sunlight Harvesting with Tapered Triangle Nanopatterning of Thin Films	19
3.1 Abstract	19
3.2 Introduction	20
3.3 Methods	21
3.3.1 Sample Fabrication	21
3.3.2 Optical Measurements	21
3.3.3 Numerical Model	22
3.4 Results and Discussion	23
3.5 Conclusions	29

4	Proximal Gap Plasmon Nanoresonators in the Limit of Vanishing Inter-Cavity Separation	31
4.1	Abstract	31
4.2	Introduction	32
4.3	Methods	33
4.3.1	Sample Fabrication	33
4.3.2	Optical Measurements	34
4.3.3	Numerical Modeling	34
4.4	Results and Discussion	36
4.5	Conclusions	46
5	Three-dimensional Confinement of Light in Deeply Subwavelength Gap-plasmon Nanocavities	47
5.1	Abstract	47
5.2	Introduction	48
5.3	Methods	49
5.3.1	Numerical Modeling	49
5.4	Results and Discussion	50
5.5	Conclusions	57
6	Macro-Scale Thermal Response of a Broadband Plasmonic Absorber	59
6.1	Abstract	59
6.2	Introduction	60
6.3	Methods	61
6.3.1	Sample Fabrication	61
6.3.2	Infrared Thermography Measurements	62
6.3.3	Area Coverage Calculation	67
6.3.4	Numerical Simulations	67
6.4	Results and Discussion	68
6.5	Conclusions	73
7	Direct Observation of Charge Separation on Au Localized Surface Plasmon	75
7.1	Abstract	75
7.2	Introduction	75
7.3	Methods	77
7.3.1	HR-XAS Measurements	77
7.3.2	IR Measurements	79
7.4	Results and Discussion	81
7.5	Conclusions	86

8	Conclusions and Outlook	87
	Appendices	89
A	Evolution of Plasmonic Crystal Modes from Plasmonic Atomic Modes	91
A.1	Abstract	91
A.2	Introduction	91
A.3	Methods	92
	A.3.1 Numerical Modeling	92
	A.3.2 Absorption Cross Section Computation	92
A.4	Results and Discussion	93
A.5	Conclusions	94
	Curriculum Vitae	121

Chapter 1

Introduction

When, at the beginning of the 17th century, for the first time Galileo looked into the universe with his own eyes through a telescope, the progress of science and humanity started to change drastically. Indeed, direct *observation* of natural phenomena had been the basis of any *scientific* investigation for centuries but only the inventions of the telescope and the microscope could give access to two fields of research which completely changed our way of thinking about the world: astronomy and microscale-sciences.

Since Galileo's telescope [1] and Hooke's microscope [2], these optical instruments have been used and improved throughout the centuries, supplying experimental evidence for a countless number of scientific discoveries [3]. However, though more powerful than our eyes, light-based optical devices are limited in resolution due to the wave nature of light. As discussed by Abbe already in 1873, the *diffraction limit* fixes the maximum achievable resolution to a value close to half the wavelength of the used light. For this reason, in the last half a century, parallel to the progressive miniaturization of the specimens, new instruments such as the scanning electron microscope (SEM) or the scanning tunneling microscope (STM) were invented, extending our imaging capabilities down to the atomic scale.

If on the one hand diffraction restricts the size of the smallest resolvable object, on the other hand it constraints the possibility to focus light to an arbitrarily small spot. This fact has direct consequences on the possibility of efficiently coupling light with nanoscale objects, e.g. molecules or nano-particles, which then remain almost *invisible* to a light wave. With the development of nanotechnology, this aspect has become especially crucial as many important applications, from electronics to energy conversion and storage, would highly benefit from the possibility of capturing, focusing and concentrating light at the nanoscale. For example, electronic circuits could be operated at much higher frequencies with a significant increase in the sup-

1. Introduction

ported bandwidth or solar-cells could be made much thinner with beneficial effects both on their price and efficiency. However, contrary to the case of microscopy, very few solutions have been proposed to achieve efficient light manipulation at the nanoscale.

Metallic nanostructures supporting surface plasmon resonances (resonant oscillations of their electron cloud) are, to date, the most promising solution to this problem. Surface plasmons, in fact, are electromagnetic waves supported at a metal-dielectric interface which are strongly bound to that interface. An important consequence of plasmon excitation is the large enhancement of the apparent size of the involved metallic nanostructure which can thus efficiently couple with the incoming light-wave despite its deeply subwavelength dimensions. Moreover, depending on the materials and the geometry of the system, the excited wave will have different characteristics in terms of spectral position, field profile and degree of confinement as well as propagation distance. Engineered plasmonic structures can then be designed to achieve the desired combination of these parameters depending on the application. For example, surface plasmons with long propagation distances are necessary to transport the signal in electronic circuits while configurations with strong field enhancements are required for Raman spectroscopy substrates or ultra-sensitive sensors.

Efficient light capture and tunable working wavelength are interesting properties to be exploited in sunlight (or more generally white light) harvesting applications where the light characteristics and the optical properties of the active components (e.g. semiconductor band-gap in solar cells) cannot be manipulated at will and where a significant reduction in the system thickness would reduce costs and increase performances. Nevertheless, the broadband spectrum of sunlight as well as its unpolarized nature and the variable incident direction pose serious challenges to the design of optimal plasmonic structures.

Furthermore, for most applications, e.g. photovoltaic cells, thermoelectric radiation sensors or photocatalytic fuel generation, light capture is only the first step in the conversion process. In fact, the *absorbed* light has to be further converted into electricity, heat or chemical products respectively. Therefore, the chosen plasmonic design should not only absorb but also confine light in the required volumes (i.e. in the active material) or directly contribute to the final conversion process.

Lastly, realistic proposals for several applications, above all sunlight energy conversion, require the possibility of significantly up-scaling of the system, a challenging step for many designed nano-structures.

The ultimate scope of this thesis is to investigate the potential of plasmonic structures in light conversion technologies with a preferential attention

to sunlight related applications such as solar thermoelectric and photocatalysis. For this reason we mainly focused on a facile plasmonic design which can potentially be up-scaled. Performing a combination of optical, thermal and eventually x-ray studies we elucidate the properties and potentialities of the considered plasmonic design in terms of light absorption, confinement and finally conversion.

1.1 Thesis Outline

This thesis is organized in eight chapters including this introductory part. The core chapters (from 3 to 7) are conceptually divided into three parts concerning the absorption of light (Chapter 3), its confinement in nanoscale volumes (Chapters 4 – 5) and finally the use of the concentrated light for energy applications (Chapter 6 – 7).

Chapter 2 introduces the fundamental concepts of plasmonics and the most important formulations used in the rest of the thesis. In particular, we present the full mathematical derivation of the equations describing the surface plasmon waves from which all their essential features can be derived. Moreover, we introduce the notation and the sign convention of the most important physical quantities related to surface plasmons.

Chapter 3 presents the design and experimental realization of an ultrathin (260 nm), broadband plasmonic absorber with average absorption of 88% within the spectral range 380 – 980 nm. The novelty of our design is based on the exploitation of four distinct plasmonic absorption phenomena within the same structure. We show how, through the optimization of the geometrical parameters, we were able to combine the collective benefit of these resonances and piece together a continuous absorption band. Furthermore, the chosen fabrication process is compatible with large scale, roll-to-roll procedures, and its multilayer design could be easily adapted to include an active (e.g. semiconductor) material. Therefore, our design is a valuable candidate for white/sunlight light harvesting applications. Finally, during the optimization process we highlight an anomalous behavior which we investigate more deeply in the second part of this thesis.

Chapter 4 investigates the properties of arrays of proximal, ultrathin gap plasmon nanocavities before and after the establishment of an electrical contact between them. We experimentally and numerically investigate the characteristics of each of the two metasurfaces (array of disconnected and connected nanocavities) as well as the reasons underlying the abrupt change in optical properties of the system between these two states.

Chapter 5 expands the study of the network of gap plasmon waveguides

1. Introduction

presented in Chapter 4. In particular, we consider the confinement capabilities of this system. Due to the ultrathin dielectric spacer, the non-uniform cross-section of the waveguide and the symmetry constraints, we prove that this structure can nano-confine light in a deeply sub-wavelength nanocavity, without requiring cumbersome fabrication procedures.

Chapter 6 illustrates the light-to-heat conversion capabilities of the structure presented in Chapter 3. After fabricating the ultra-thin absorber as a free standing membrane, we used an infrared camera to quantify its stationary as well as transient thermal response upon illumination. When compared to a commercial, flat, blackening spray, the ultrathin plasmonic absorber shows a considerably lower response time and a comparable temperature raising capability. In addition, its low emissivity would be advantageous for high-temperature applications.

Chapter 7 elucidates the origin of the photocatalytic/sensitizer properties of plasmonic structures. Using x-rays we prove that the density of states of a gold nanoparticle changes during steady state plasmonic excitation and in particular we show that the Fermi level shifts to higher energies. This elucidates how plasmonic nanostructures can play an important role as sensitizers in photocatalytic process, providing hot electrons to neighboring semiconductor catalysts. We used transient mid-IR spectroscopy to prove this second statement.

Chapter 8 concludes this thesis summarizing the main achievements and findings and proposing further direction of investigation.

Chapter 2

Fundamentals

2.1 Plasmons

In a metal, free conduction electrons behave like a gas and are thus able to sustain collective coherent oscillations (plasma waves). The quasi particle associated with a quanta of these oscillations is called *plasmon*. Plasmons can be differentiated into *volume* plasmons and *surface* plasmons. Volume plasmons are coherent longitudinal oscillations of the conduction electron against the ionic cores and cannot couple to a transverse electromagnetic wave. On the other hand, surface plasmons can couple directly to a light wave and this interaction confer exceptional optical properties to the excited metal nanostructures. Surface plasmon can have two forms:

- *Surface Plasmon Polaritons (SPPs)*. Originating by the coupling of a plasmon with a photon (polariton), they are electromagnetic waves propagating along the interface between a conductor and a dielectric and strongly bound to it (exponentially decaying in both materials).
- *Localized Surface Plasmons (LSPs)*. These are non-propagating surface plasmons strongly bound to a finite metallic nanostructure.

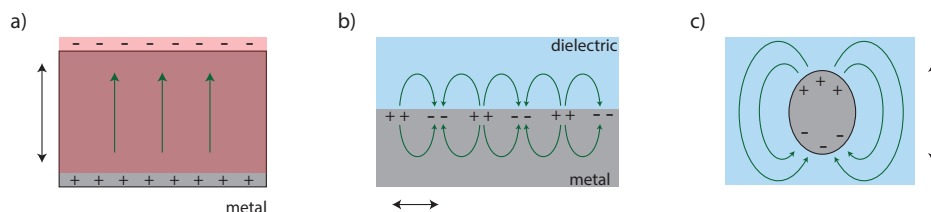


Figure 2.1: Type of Plasmons a) Volume plasmons. b) Surface plasmon polaritons. c) Localized surface plasmons. The green arrow represent schematically the electric field in the different situations.

2. Fundamentals

In the following, we briefly introduce the most important concepts and mathematical formulas which characterize these two types of surface plasmon and are frequently used in the rest of the thesis.

2.2 Surface Plasmons Polaritons

2.2.1 Dispersion Curve for a Single Interface

For any propagating electromagnetic wave, the angular frequency, ω , and the propagation wavevector magnitude, k , are related through a more or less complicated function which is called *dispersion relation*. For example, for planar light waves propagating in a homogeneous medium of refractive index n such relation is $k = \omega \frac{n}{c}$. This function, in a ω versus k graph, defines a line which is commonly called *light-line*.

SPPs are also characterized by a dispersion relation whose expression we derive in the following [4].

We consider the system illustrated in Figure 2.2 where the metal-dielectric interface corresponds to the $x - y$ plane and the dielectric constant only varies along z , $\epsilon(z)$, being equal to the metal permittivity, ϵ_m , for $z < 0$, and to the dielectric permittivity, ϵ_d , for $z > 0$. We further simplify the problem assuming a wave propagating only along the x -direction with no spatial variation in the y -direction. Assuming a harmonic time dependence $e^{i\omega t}$, the spatial term of the electric field can be written as:

$$\mathbf{E}(x, y, z) = \mathbf{E}(z)e^{i\beta x} \quad (2.1)$$

where $\beta = k_x$ is the wavevector component in the propagation direction.

This wave must satisfy the Helmholtz equation, $\nabla^2 \mathbf{E} + k_0^2 \epsilon \mathbf{E} = 0$, which leads to two distinct set of equations describing a transverse magnetic (TM) and a transverse electric (TE) mode respectively:

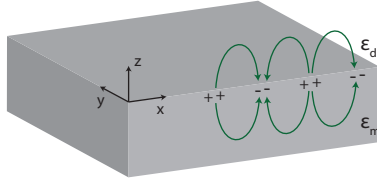


Figure 2.2: Coordinate system for the derivation of the SPP dispersion relation

2.2. Surface Plasmons Polaritons

$$TM : \begin{cases} \frac{\partial^2 H_y}{\partial z^2} + (k_0^2 \epsilon - \beta^2) H_y = 0 \\ E_x = -i \frac{1}{\omega \epsilon_0 \epsilon} \frac{\partial H_y}{\partial z} \\ E_z = -\frac{\beta}{\omega \epsilon_0 \epsilon} H_y \end{cases} \quad TE : \begin{cases} \frac{\partial^2 E_y}{\partial z^2} + (k_0^2 \epsilon - \beta^2) E_y = 0 \\ H_x = i \frac{1}{\omega \mu_0} \frac{\partial E_y}{\partial z} \\ H_z = \frac{\beta}{\omega \mu_0} E_y \end{cases} \quad (2.2)$$

As mentioned earlier, SPPs are a special class of waves which exponentially decay perpendicular to the interface both in the metal and the dielectric. Considering a TM wave, we can write the equation of the three field components, H_y, E_x, E_z , as:

$$z > 0 \begin{cases} H_y(z) = A_d e^{i\beta x} e^{-k_d z} \\ E_x(z) = i A_d \frac{1}{\omega \epsilon_0 \epsilon_d} k_d e^{i\beta x} e^{-k_d z} \\ E_z(z) = -A_d \frac{\beta}{\omega \epsilon_0 \epsilon_d} e^{i\beta x} e^{-k_d z} \end{cases} \quad (2.3)$$

$$z < 0 \begin{cases} H_y(z) = A_m e^{i\beta x} e^{k_m z} \\ E_x(z) = -i A_m \frac{1}{\omega \epsilon_0 \epsilon_m(\omega)} k_m e^{i\beta x} e^{k_m z} \\ E_z(z) = -A_m \frac{\beta}{\omega \epsilon_0 \epsilon_m(\omega)} e^{i\beta x} e^{k_m z} \end{cases}$$

where $k_{d,m} = k_{z_d, z_m}$ are the real and positive components of the wavevector perpendicular to the interface which ensure the exponential decay behavior required by SPPs.

Continuity of H_y and $D_z = \epsilon_{d,m} E_z$ lead to the conditions:

$$\begin{aligned} A_d &= A_m \\ \frac{k_d}{k_m} &= -\frac{\epsilon_d}{\epsilon_m(\omega)} \end{aligned} \quad (2.4)$$

As $k_{d,m} > 0$ (see above), a SPP can be only supported when the permittivity of the two materials have opposite sign, as in the case of a dielectric-metal interface for frequencies below the metal bulk plasmon frequency.

The momentum conservation condition requires:

$$\begin{aligned} k_m^2 &= \beta^2 - k_0^2 \epsilon_m(\omega) \\ k_d^2 &= \beta^2 - k_0^2 \epsilon_d \end{aligned} \quad (2.5)$$

and combining equations 2.4 and 2.5 we obtain the SPP dispersion relation (the ω dependence is implicit in the frequency dispersion of the metal permittivity, ϵ_m):

$$\beta = \sqrt{\frac{\epsilon_m(\omega) \epsilon_d}{\epsilon_m(\omega) + \epsilon_d}} \quad (2.6)$$

2. Fundamentals

Applying the same reasoning to the TE solution leads to a condition equivalent to equation 2.4 but which cannot be satisfied if an exponentially decaying wave is assumed. Thus, SPPs can exist only as TM polarization. Furthermore, we observe that SPPs are electromagnetic waves with a mixed transversal and longitudinal nature as both E_x (along the propagation direction) and E_z (perpendicular to the propagation direction) components are non-zero (see equation 2.3) .

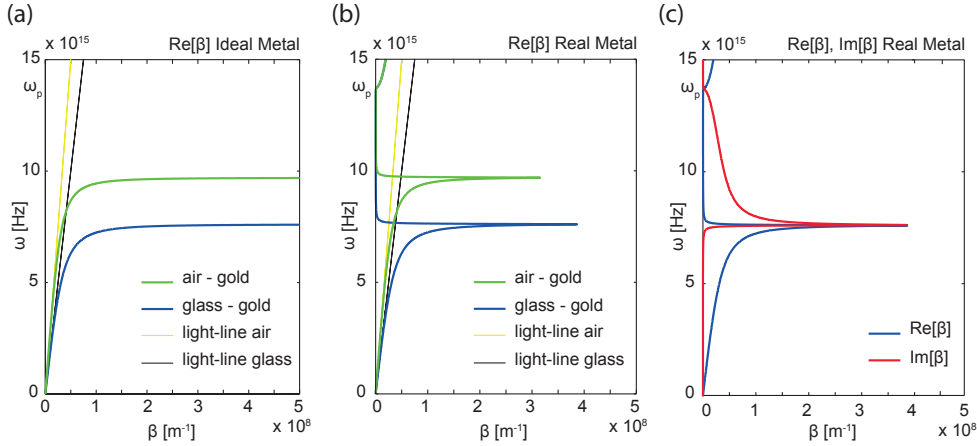


Figure 2.3: Dispersion Curve for a SPP Propagating on a Dielectric-Metal Interface (a) Dispersion curve calculated with equation 2.6 for a air-gold (green line) and glass-gold (blue line) interface in the case of an ideal metal (Drude model without losses, $\omega_p = 2\pi \cdot 2.183 \cdot 10^{15}$ Hz [4]) (b) Same as (a) but calculated for a real metal using $\tau = 3 \cdot 10^{-14}$ s [5] (c) Real and imaginary part of the propagation wavevector calculated for the case of a glass-gold interface and a real metal (see (b)).

The dispersion curves for an idealized metal (without losses, real ϵ_m) is represented in Figure 2.3.a. We observe that the SPP curve always lies on the right side of the light-line ($\beta > k_d > k_{vacuum}$) thus implying that SPP excitation requires special momentum matching techniques (e.g. grating coupling, prism coupling etc.). For low frequencies the SPP curve is very close to the light-line and the wave has a low degree of confinement (decay length $l_{dec} = 1/k_d$ where k_d is obtained from equation 2.5). As the frequency increases the SPP wavevector increases dramatically and it asymptotically tends to infinity for $\omega \approx \omega_{sp}$, corresponding to the condition $\omega_{sp} : \epsilon_m(\omega_{sp}) = -\epsilon_d$. Concurrently, the field gets strongly confined at the interface. Furthermore, the SPP group velocity $v_g = \frac{\partial \omega}{\partial \beta}$ steadily decreases as β increases and in the limit of $\omega \approx \omega_{sp}$ the SPP assumes an electrostatic character, similar to a localized surface plasmon (LSP).

Real metals, however, present a complex dielectric permittivity $\epsilon_m = \epsilon'_m + i\epsilon''_m$ and, due to the damping term, the SPP wavevector does not go to infinity (see Figure 2.3.b). Moreover, if for a perfect metal no wave is

allowed to propagate for $\omega > \omega_{sp}$ due to a purely imaginary β , for real metals a so called *quasibound, leaky* wave can be supported at the metal dielectric interface for these frequencies.

The complex ϵ_m of real metals has also important consequences on the SPP propagation distance. In fact, while for ideal metals SPPs can propagate indefinitely without losses ($Im[\beta] = 0$), for real metals β is always a complex value implying that SPPs are damped as they propagate. We can observe in Figure 2.3.c that as $Re[\beta]$ increases (as the frequency approaches ω_{sp}), $Im[\beta]$ also increases. Therefore, in real cases, a strong field confinement and a very slow wave come at the expenses of large losses in the metal which limit the propagation of such a wave over large distances.

2.2.2 Multiple Interfaces and Mode Splitting

So far we discussed the SPP supported by a single metal-dielectric interface. We now consider the case of multiple metal-dielectric interfaces which, as will be shown, present a richer solution space. For simplicity we study the case of only two parallel interfaces oriented along the $x - y$ plane and separated by a distance h (see [6] for a general derivation). Two cases are then possible, either a metal layer of thickness h surrounded by two dielectrics (Insulator-Metal-Insulator - IMI - case) or a dielectric layer of thickness h surrounded by two metals (Metal-Insulator-Metal - MIM - case).

In both situations, similarly to the case of a single interface, the TM

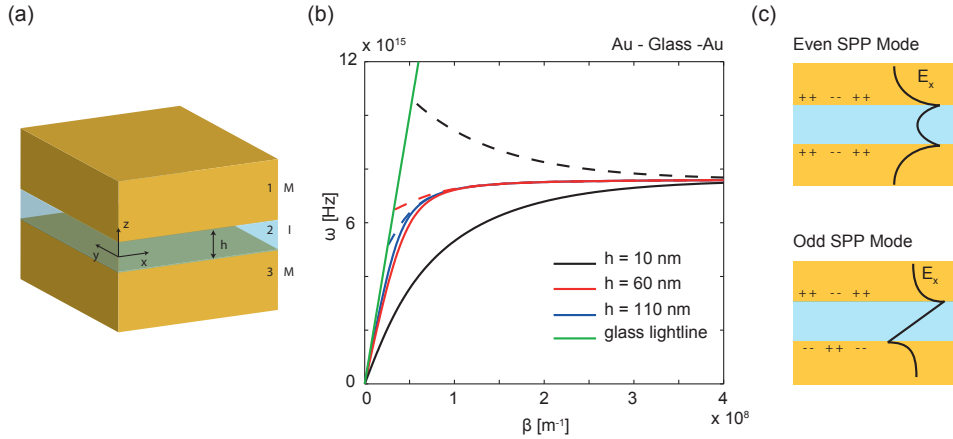


Figure 2.4: Dispersion Curve for a MIM Structure (a) Schematics of the geometry (b) Dispersion curves calculated with equation 2.8 for a gold-glass-gold MIM structure for a dielectric thickness of $h = 10$ nm (black line), $h = 60$ nm (red line), $h = 110$ nm (blue line) and an idealized metal (Drude model without losses, $\omega_p = 2\pi 2.183 \cdot 10^{15}$ Hz[4]). The continuous lines represent the *odd mode* without cut-off while the dashed line represent the *even mode* for the same dielectric thickness. (c) Schematic representation of the even (upper panel) and odd (lower panel) modes in a MIM structure.

2. Fundamentals

equations for a wave propagating in the x -direction and evanescent along the y -direction can be written separately for each layer (see Figure 2.4.a). However, for the middle layer the wave will be a linear combination of the two waves propagating at the upper and lower interfaces respectively. Indeed, we write:

$$\begin{aligned}
 z > h/2 & \begin{cases} H_y(z) = Ae^{i\beta x} e^{-k_1 z} \\ E_x(z) = iA \frac{1}{\omega \epsilon_0 \epsilon_1} k_1 e^{i\beta x} e^{-k_1 z} \\ E_z(z) = -A \frac{\beta}{\omega \epsilon_0 \epsilon_1} e^{i\beta x} e^{-k_1 z} \end{cases} \\
 -h/2 < z < h/2 & \begin{cases} H_y(z) = Be^{i\beta x} e^{k_2 z} + Ce^{i\beta x} e^{-k_2 z} \\ E_x(z) = -iB \frac{1}{\omega \epsilon_0 \epsilon_2} k_2 e^{i\beta x} e^{k_2 z} + iC \frac{1}{\omega \epsilon_0 \epsilon_2} k_2 e^{i\beta x} e^{-k_2 z} \\ E_z(z) = B \frac{\beta}{\omega \epsilon_0 \epsilon_2} e^{i\beta x} e^{k_2 z} + C \frac{\beta}{\omega \epsilon_0 \epsilon_2} e^{i\beta x} e^{-k_2 z} \end{cases} \\
 z < -h/2 & \begin{cases} H_y(z) = De^{i\beta x} e^{k_3 z} \\ E_x(z) = -iD \frac{1}{\omega \epsilon_0 \epsilon_3} k_3 e^{i\beta x} e^{k_3 z} \\ E_z(z) = -D \frac{\beta}{\omega \epsilon_0 \epsilon_3} e^{i\beta x} e^{k_3 z} \end{cases}
 \end{aligned} \tag{2.7}$$

Applying the continuity of H_y and E_x at the two interfaces we obtain an implicit expression for the SPP dispersion curve:

$$e^{-4k_2 h/2} = \frac{\frac{k_2}{\epsilon_2} + \frac{k_3}{\epsilon_3} \frac{k_2}{\epsilon_2} + \frac{k_1}{\epsilon_1}}{\frac{k_2}{\epsilon_2} - \frac{k_3}{\epsilon_3} \frac{k_2}{\epsilon_2} - \frac{k_1}{\epsilon_1}} \tag{2.8}$$

where $k_i^2 = \beta^2 - k_0^2 \epsilon_i$ for $i = 1, 2, 3$.

Furthermore, we will have $\epsilon_{1,3} = \epsilon_m$ and $\epsilon_2 = \epsilon_d$ for an MIM structure and viceversa for a IMI structure.

With respect to the single interface case, we observe two aspects. Firstly, the relation includes the geometrical parameter h which becomes an extra degree of freedom (in addition to the materials forming the interface) in the definition of the dispersion curve. Secondly, depending on the ratio between the dielectric constants of the different materials, one or two solutions can be found, some of which with a lower or upper cut-off [7]. The presence of multiple solutions is due to the coupling between the two interfaces which leads to mode splitting. For increasingly large values of h the coupling weakens and eventually disappears and the solution is the same of the single interface case. Due to the dispersive optical properties of the metals ($\epsilon(\omega)$), the type of solution depends on the considered frequency as well.

Figure 2.4.b illustrates the mode splitting for a gold-glass-gold (MIM) system for decreasing thickness of the dielectric core (ideal metal). Already

for core thicknesses ≈ 100 nm two distinct branches are visible. The upper branch is the so-called *even* or *symmetric* mode because E_x , the electric field component in the propagation direction, has equal signs at the two interfaces (see Figure 2.4.c, upper panel). The lower branch, instead, is the so-called *odd* or *asymmetric* mode as E_x has opposite sign at two interfaces¹ (see Figure 2.4.c, lower panel). The even mode in the MIM configuration has a lower cut-off thickness and is not supported for very thin dielectric spacers.

In this thesis we mainly work with MIM structures composed of gold (Au) or silver (Ag) layers separated by a glass spacer with thicknesses between $h = 7$ nm and $h = 100$ nm. In particular, in chapters 3 – 5, we extensively study asymmetric MIM structures (mixed Au-Ag) with ultra-thin dielectric cores, investigating the extreme confinement properties of the supported odd SPP modes. In these structures, the SPP modes are also called *gap plasmon modes* due to their confinement in the dielectric layer (*gap*).

2.2.3 Effective Refractive Index and Nanofocusing

The SPP propagation wavevector β can be expressed as a function of the vacuum wavelength λ_0 introducing an *effective refractive index* n_{eff} of the mode:

$$\beta = \frac{2\pi}{\lambda_0} n_{eff} \quad (2.9)$$

Like the refractive index of a material, n_{eff} is related to the speed of the SPP wave in the waveguide and to the optical length of the covered path. From equation 2.9 we observe that the larger β the higher n_{eff} and the slower the SPP wave.

We know that the SPP mode wavevector at a given wavelength strongly depends on the dielectric spacer thickness. Therefore, a SPP mode propagating in a MIM waveguide with decreasing dielectric thickness would be progressively slowed down and compressed along the direction of propagation due to the increase in n_{eff} . This process is called *nanofocusing*. A complete mathematical derivation of this nanofocusing concept can be found in [6] and several experimental implementations of this idea can be found in the literature (e.g. [8]).

¹Special care has to be taken concerning the definition of *odd* and *even* SPP modes. In fact, H_y and E_z have opposite parity compared to E_x . Therefore the mode which is defined as *odd* with respect to E_x would be defined as *even* with respect to H_y or E_z . In the literature both conventions are used even though the first one, which we follow in this thesis, is more common.

2. Fundamentals

2.2.4 Gap Plasmons in Truncated MIM Structures

So far we discussed multilayer structures only composed of continuous layers. A different system can be obtained truncating one or more layers in one or two dimensions, as illustrated in Figure 2.5.a. While the continuous layer structure is characterized by a continuous dispersion curve (*non-resonant* phenomenon), the truncated system behaves like an optical nanocavity and exhibits a discrete dispersion spectrum (*resonant* system, Figure 2.5.b).

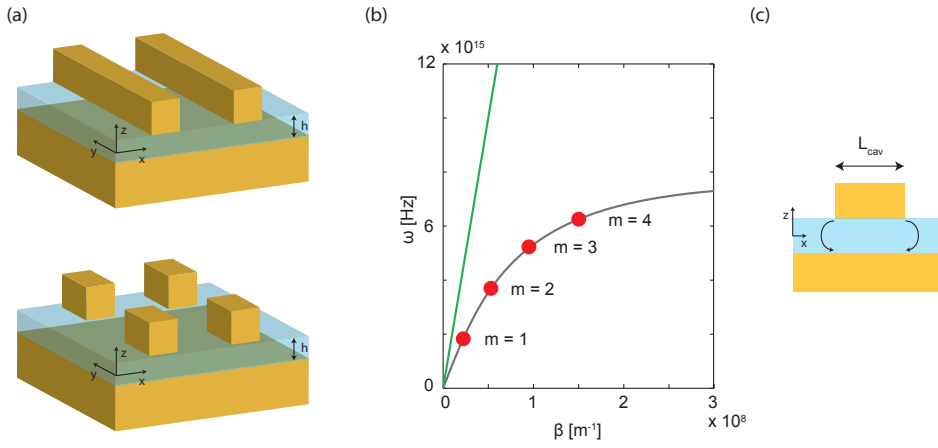


Figure 2.5: Truncated MIM Structures (a) MIM structure truncated in one dimension (MIM strip, upper panel) and in two dimensions (MIM patch or nanoresonator, lower panel) (b) Discrete dispersion spectrum of a truncated MIM structure (red-dots) compared to the corresponding continuous curve of the infinite MIM waveguide (c) Mode reflection at the terminations of the truncated MIM structure

As shown first by Nielsen [9] and more recently by Moreau [10], the terminations of the truncated metal layer cause the reflection of the gap plasmon (GP) modes (see Figure 2.5.c) into the cavity leading to the interference between counter-propagating modes. The resonance frequencies of the nanocavity are then defined by the constructive interference condition (also called *Fabry-Perot interferometer* condition):

$$L_{cav} \cdot \beta = m\pi + \varphi \quad (2.10)$$

where L_{cav} is the physical cavity length, β is the GP mode wavevector, m is the order of the resonance mode and φ is the phase acquired upon reflection.

Generally, the mode reflection at the cavity termination is not perfect. Therefore, φ is different from zero and the mode extends outside of the nanocavity. However, as the thickness of the dielectric core decreases, the wavevector of the GP mode increases and the same does its effective refractive

index. Consequently, the refractive index mismatch between the nanocavity and its surroundings increases with a beneficial effect on φ which becomes closer to zero. Therefore, ultra-thin MIM structures are characterized by a large confinement of the mode in the nanocavity.

2.3 Localized surface plasmons

2.3.1 Absorption and Scattering Cross Sections

The interaction of a finite metallic nanostructure, e.g. a nano-sphere, with an electromagnetic wave leads to a modification of the incident field in two ways (see Figure 2.6.a) [11]:

- *scattering* of the incident field: the incoming wave is partially redirected in directions different from the initial propagation direction
- *absorption* of the incident field: the incoming wave is attenuated due to dissipation within the metallic structure

Together, these two mechanisms are responsible of the *extinction* of the incident wave.

The ratio of the scattered energy versus the incident irradiance is called *scattering cross-section*, C_{sca} , the ratio of the absorbed energy versus the incident irradiance is called *absorption cross-section*, C_{abs} , and the sum of these two is called *extinction cross-section*, C_{ext} . The quantities $C_{sca,abs,ext}$ have dimensions of m^2 and can be regarded as the apparent size of the structure with respect to any of these processes (see Figure 2.6.c).

For a sphere much smaller than the wavelength of light (*electrostatic approximation*, see Figure 2.6.b), the total external field can be shown [11], [4] to be equal to the superposition of the incident field E_0 and the field of an ideal dipole located at the origin which has a moment p :

$$p = \epsilon_0 \epsilon_d \alpha E_0 \quad (2.11)$$

where

$$\alpha = 4\pi a^3 \frac{\epsilon_m(\omega) - \epsilon_d}{\epsilon_m(\omega) + 2\epsilon_d} \quad (2.12)$$

is the *polarizability* of the nano-sphere, a is the radius of the sphere, ϵ_d is the surrounding medium permittivity and $\epsilon_m(\omega)$ is the complex, frequency dependent dielectric constant of the metal.

2. Fundamentals

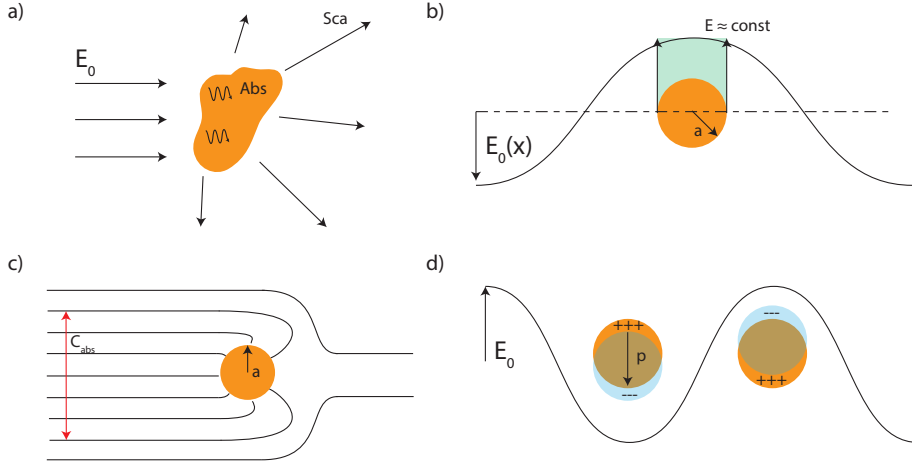


Figure 2.6: Truncated MIM Structures (a) Schematics of absorption and scattering processes (b) Schematic representation of the electrostatic approximation. The size of the particle, a , is much smaller than the wavelength of the incoming light so that the electric field across the nanostructure is almost constant at any instant of time (c) Schematic representation for the enhancement in absorption cross section due to the plasmonic effect. The lines represent energy flux lines. At resonance the particle interact with much more light than the one directly impinging onto it (d) Schematic representation of the dipolar plasmonic resonance. At two instant of time, the electron cloud is displaced with respect to the crystal ionic cores following the oscillating electric field. This leads to charge separation and therefore a dipolar polarization characterized by the dipole moment p .

For such a system, through the knowledge of the Poynting vector, it is possible to calculate:

$$\begin{aligned}
 C_{sca} &= \frac{k^4}{6\pi} |\alpha|^2 = \frac{8\pi}{3} k^4 a^6 \left| \frac{\epsilon_m(\omega) - \epsilon_d}{\epsilon_m(\omega) + 2\epsilon_d} \right|^2 \\
 C_{abs} &= k \text{Im}[\alpha] = 4\pi k a^3 \text{Im} \left[\frac{\epsilon_m(\omega) - \epsilon_d}{\epsilon_m(\omega) + 2\epsilon_d} \right] \\
 C_{ext} &= C_{sca} + C_{abs}
 \end{aligned} \tag{2.13}$$

Immediately we observe that the absorption and scattering cross section scale differently with the radius of the particle, a , absorption being dominant for smaller particles. Furthermore, we observe that all of the calculated cross-section exhibit a resonance condition corresponding to the frequency for which the denominator of the polarizability vanishes. At the resonance condition, therefore, all the effective cross-sections become much larger than the physical cross-section A_{geom} and the structure interacts with much more light than the one directly impinging on it. Normalizing $C_{sca,abs,ext}$ to the physical cross-section, A_{geom} of the considered nanoparticle, we can then define the *scattering*, *absorption* and *extinction efficiencies*, respectively:

2.3. Localized surface plasmons

$$Q_{sca,abs,ext} = \frac{C_{sca,abs,ext}}{A_{geom}} \quad (2.14)$$

As stated previously, in the electrostatic approximation, the nanoparticle is equivalent to a dipole. Therefore, the frequency upon which the resonance is excited correspond to the dipolar resonance condition which is also the fundamental localized plasmon resonance (see Figure 2.6.d). Larger nanostructures are characterized by retardation effects; also, they can support higher energy oscillation modes/LSPs which, for a sphere, can be calculated from the Mie coefficients [11], [4].

From the expression of the polarizability (see equation 2.12), we can infer all the relevant parameters affecting the LSP resonance condition which are:

- nanoparticle metal ($\epsilon_m(\omega)$)
- surrounding dielectric metal (ϵ_d)
- geometry of the nanoparticle: indeed the derived polarizability expression refers to a sphere; different shapes would lead to different expressions (see for example the ellipsoid in [11]).

Therefore LSP resonances have a high degree of tunability, considered that any variation of these parameters would cause a change in their spectral position. In particular, the dependance on the surrounding dielectric constant, ϵ_d , is widely exploited to design ultra-sensitive sensors. Indeed, due to the high degree of localization of the electric field in the proximity of the nanostructure, even a small perturbations of the surrounding environment happening directly at the nanoparticle surface, e.g. even a molecule binding to it, immediately changes ϵ_d so that, in far field, this event can be detected through the shift in the plasmonic resonance frequency.

Finally, we observe that, contrary to SPPs, LSPs are non-propagating waves (zero group velocity). Therefore, they are characterized by an almost purely electric character and do not require any phase matching technique to be excited.

2.3.2 Coupling between Nanostructures

We just saw that a plasmonic system resonating at its fundamental frequency is equivalent to a dipole with polarizability α . Therefore, two plasmonic nanoparticles separated by a distance l can interact through either near or far field, the same way two dipoles would interact [4]. Nevertheless, the complex dependance of the plasmon resonance modes on the geometry of the

2. Fundamentals

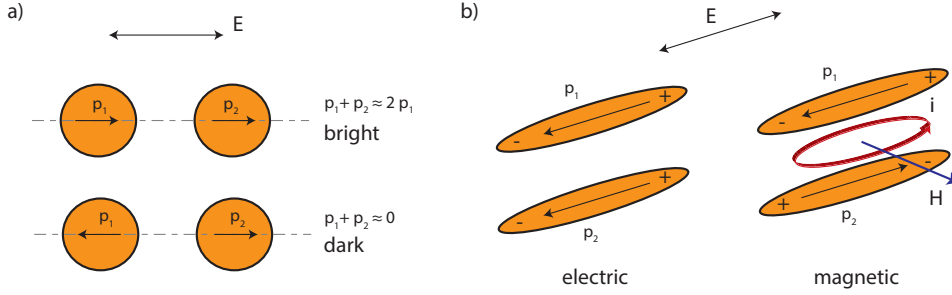


Figure 2.7: Truncated MIM Structures (a) Schematics of the resonance modes of a dimer illuminated with light polarized along the inter-particle axis (b) Schematics of the resonance modes of two long aligned with their long axis parallel and illuminated from top with polarization along the same axis

system allow for a much richer variety of interactions [12]. Similarly to the case of molecular orbital, the plasmonic resonances of interacting plasmonic nanostructures can be described as coupled plasmonic modes of the original entities which located at different wavelengths (energies) according to the hybridization rules [12]. In the following we briefly report some important examples of interacting plasmonic systems [12].

Dimers: Bright and Dark Modes

When two equal plasmonic nanostructures interact with each other we have a so-called dimer. When the incident light is polarized along the axis separating the two nanostructures (see Figure 2.7.a), coupling of the original dipolar resonances leads to two new modes, one at lower energy (red-shifted, *bonding mode*) and one at higher energy (blue-shifted, *anti-bonding mode*). The low energy mode has a dipole moment which is close to the sum of the original dipole moments, p , and is thus stronger than the isolated structure resonance. This mode is also called *bright mode* due to its effective coupling with far-field radiation. On the other hand, the high energy mode is characterized by the anti-parallel alignment of the original dipole moments, leading to an almost zero dimer moment. This mode is then called *dark mode* due to the fact that it cannot be excited with far-field radiation but only through near-field excitation techniques. If higher order LSP resonances are present, the dimer will present a complex spectrum with multiple resonances originating from the coupling of modes of different order. Finally, if the excitation is polarized perpendicular to the inter-particle axis, the coupling is minimal, eventually characterized by a small blue-shift of the resonance position.

Nanorods: Electric and Magnetic Resonances

Nanorods are elongated plasmonic nanoparticles characterized by a longitudinal and a transversal plasmonic resonance happening at long and short wavelength respectively. When two nanorods aligned with their long axis parallel to each other are excited with light polarized parallel to this same axis, two resonances can occur, similarly to the dimer case. Interestingly, in this case the low energy mode is characterized by the anti-phase coupling of the dipole moments. As shown in Figure 2.7.b, the opposite currents excited in the two nanorods, together with the displacement currents at the extremities of the system, give rise to a current circulation and therefore to the formation of a magnetic field. Such resonance is thus called *magnetic resonance*. On the other hand, the high energy mode is characterized by the parallel alignment of the dipole moments and is called *electric resonance*.

Particle over a Film

When a metallic nanoparticle is brought close to a metallic surface two types of interactions can occur. On the one hand the nanoparticle can interact with its own image. This coupling has characteristics similar to the dimer case with the restriction that the image charge is always the mirror of the particle charge. On the other hand, it can couple with the propagating surface plasmons supported by the continuous metallic interfaces. The effect of such coupling is more complex leading to either a blue-shift or a red-shift of the modes depending on the relative energies of the SPP and LSP resonances as well as the particle-surface distances. For example, for an infinitely thick film of the same metal of the nanoparticle, a strong red-shift of the system resonances can be observed upon reduction of the film-particle distance.

Chapter 3

Facile Multifunctional Plasmonic Sunlight Harvesting with Tapered Triangle Nanopatterning of Thin Films

Part of this chapter has been published in *Nanoscale*, 2013, 5(20), pp. 9957–62.

3.1 Abstract

Plasmonic absorbers have recently become important for a broad spectrum of sunlight-harvesting applications exploiting either heat generation, such as in thermal photovoltaics and solar thermoelectric, or hot-electron generation, such as in photochemical and solid state devices. So far, despite impressive progress, combining the needed high performance with fabrication simplicity and scalability remains a serious challenge. Here, we report on a novel solar absorber concept, where we demonstrate and exploit simultaneously a host of absorption phenomena in tapered triangle arrays integrated in a metal-insulator-metal configuration to achieve ultrabroadband (88% average absorption in the range 380–980 nm), wide-angle and polarization-insensitive absorption. Furthermore, this absorber is subwavelength in thickness (260 nm) and its fabrication is based on a facile, low-cost and potentially scalable method. In addition, the geometry of our design makes it compatible for both heat and hot electron generation.

3.2 Introduction

During the past few years, plasmonic structures have been increasingly employed in various solar light harvesting applications, e.g. as light management structures in solar cells [13, 14], nano-scale heat sources in thermal photovoltaic or thermoelectric systems [15, 16], and hot-electrons generators for photochemical reactions [17, 18], or solid-state devices [19, 20]. The main promise of plasmonics is the unique capability to fulfill demanding requirements of such devices which need to be broadband as well as insensitive to light polarization and angle of incidence, and for several novel applications, sub-wavelength in thickness [21]. In addition, a facile [10] and controllable nanofabrication technique is required on the way to realistic applications. Unlike polymer-metal nano-composites [22, 23, 24], which can fulfill some of these requirements, well-defined nanopatterns usually provide access to hot-spots where energy is strongly concentrated and subsequently exploited [19, 17, 20]. Aydin et al. [25] first introduced a plasmonic broadband absorber taking advantage of multiple resonances in a metal-insulator-metal (MIM) stack with a top silver film consisting of crossed trapezoidal arrays and achieved 71% average absorption within the visible spectrum (400-700 nm).

While different geometries showed further improvements [26] their small scale structuring is attained with difficult and improbable to upscale fabrication methods. A different theoretical approach based on conformal transformations has exploited non-resonant nano-focusing at the end of sharp tips or grooves to achieve plasmonic nanostructures with very large absorption cross-sections over a broad spectral range [27, 28, 29]. Following a similar principle, Sondergaard et al. [30, 31], realized a broadband absorber consisting of an array of ultra-sharp convex grooves. Despite impressive results ($\geq 87\%$ absorption over 450-850 nm) their design requires extremely narrow features, which are achieved by a cumbersome combination of electron-beam lithography and focused ion-beam milling (also practically impossible to upscale). Moreover, the structure is not subwavelength and the focusing hot-spots are deeply buried into the structure, therefore inaccessible for several light harvesting applications. In this chapter, we address these issues by a concept, which exploits various plasmonic absorption phenomena in an array of tapered triangles within an MIM structure. While achieving a near-ideal solar absorber, we are able to fabricate the device with a potentially low-cost and easily accessible method, a must if plasmonic solar harvesting is to become a reality outside the research laboratory.

3.3 Methods

3.3.1 Sample Fabrication

The MIM structure is composed of three layers (see Figure 3.2.a). A 100 nm gold back-reflector and a 60 nm SiO_2 layer were coated successively on a clean glass coverslip (18×18 mm) using electron-beam evaporation and plasma-enhanced chemical vapor deposition, respectively. The thickness of the dielectric spacer and optical properties of SiO_2 and gold layers were always measured using ellipsometry. After cleaning with a 6 : 1 : 1 solution of H_2O : NH_4OH : H_2O_2 in ultrasonic bath for 10min, the samples were stored for 24h in ethanol to ensure full hydrophilicity of the glass surface. A front hexagonal gold pattern was fabricated using nano-sphere lithography (NSL) [32, 33, 34, 35] and reactive ion etching (RIE). First, a closely packed monolayer of polystyrene beads (Sigma Aldrich, diameter 300 nm) is created using dip-coating. The core of the dip-coating set-up is the linear micro stage (M-112.1DG, PI-Physik Instrumente) controlled by a DC servo motor (C-863.11, PI-Physik Instrumente). These two components ensure a smooth movement even at very low speeds, preventing disturbances of the meniscus motion due to uneven displacements. The dip-coating set-up is placed inside a closed plexiglass chamber which is equipped with humidity and temperature sensors. The humidity can be actively controlled and set to a desired value: a flow of dry nitrogen is passed through a glass bottle containing an ultrasonic vaporizer which can produce variable amounts of fine water fog. The sample is quickly immersed into a diluted bead solution (1% wt, 10^{-3} M SDS) contained in a square home-made glass well and then withdrawn with controlled velocity ($2.5 \mu\text{m/s}$). The humidity is kept constant at 50%. Then, reactive ion etching is used to reduce the bead size (100 sccm Ar, 10 sccm O_2 , 50 W, 100 μbar). The bead size is controlled by adjusting the etching time. The final pattern is created by evaporating 100 nm of gold (after 2 nm Cr adhesion layer) through the bead mask and by successively removing the beads by low power ultrasonication.

3.3.2 Optical Measurements

Experimentally, we measured the absorption properties of the fabricated absorber. Absorption measurements are performed using a home-built inverted microscope equipped with an air objective (numerical aperture, NA, 0.75) for exciting the sample and collecting the reflected and scattered light and a spectrometer (Princeton Instruments) (Figure 3.1.right). White light is generated by a Xenon lamp and is brought to the set-up with an optical

3. Facile Multifunctional Plasmonic Sunlight Harvesting ...

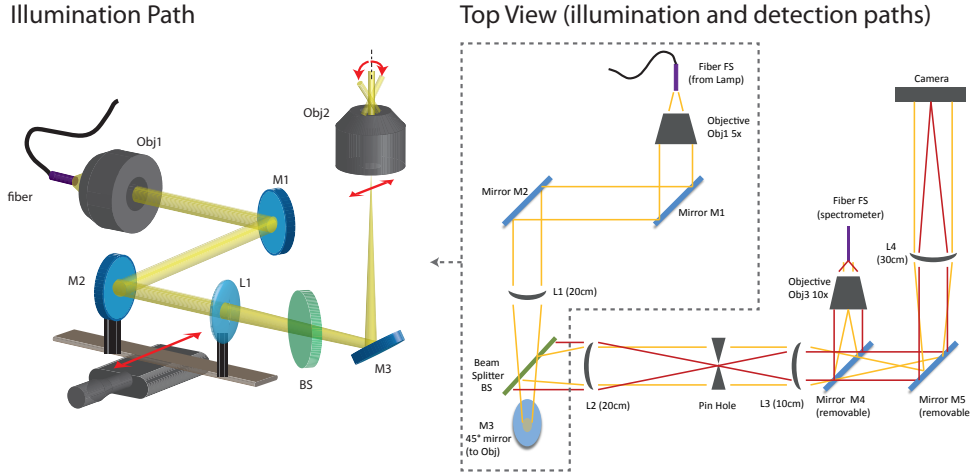


Figure 3.1: Optical Set-up. Schematic representation of the optical set-up. Left - Detail of the illumination path. Right - Top view of the entire set-up. The yellow lines represent the incident and reflected light while the red lines represent the light scattered by the sample.

fiber (105 μm core size) in order to improve its spatial coherence. Plane wave excitations with different angles of incidence (up to 48° , NA 0.75) are achieved by focusing the light beam at different positions on the back focal plane of the objective (Figure 3.1.left). The relation $A = (I - R)/I$ was used to calculate the absorption spectrum, where A, I and R are the absorption, incident (excitation) and reflected spectra, respectively. The light transmitted through the absorber was negligible. I was measured using the reflected spectrum from a broadband silver mirror. This ensures accounting for excitation spectral non-uniformities and losses along the detection path. Furthermore, dark counts of the spectrometer and background spectra were subtracted from all the measured spectra.

3.3.3 Numerical Model

Primary estimation of optimal dimensions was achieved by performing a large series of full-wave simulations with Lumerical, a commercially available finite-difference time-domain (FDTD) software package, which is very efficient for broadband simulations. However, due to the staircasing errors of FDTD at sharp edges, all of the final simulations presented in this chapter were performed using COMSOL Multiphysics package (RF module), which is based on the finite element method (FEM). By using symmetry and periodic (for normal excitation) boundary conditions the computational domain was reduced to one-fourth of a unit-cell. To model gold in the simulations, we used the optical properties tabulated in Paliks Handbook [36] which agree

3.4. Results and Discussion

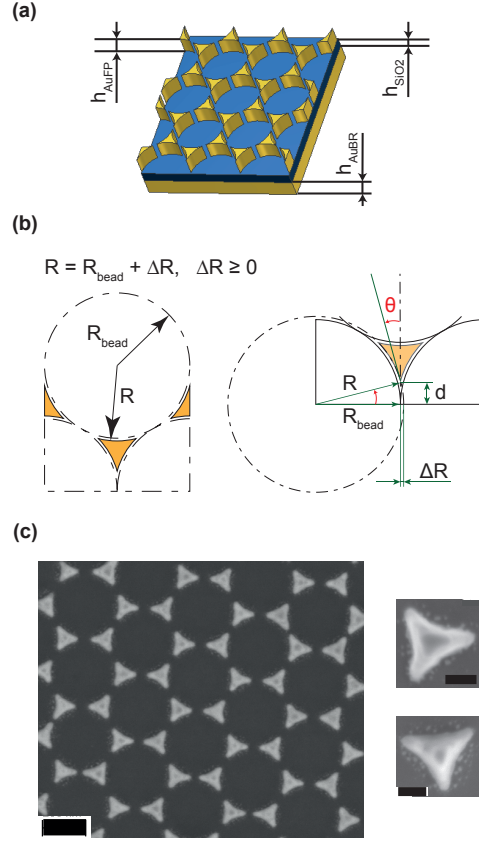


Figure 3.2: Geometry of the proposed absorber. (a) Schematic representation of the MIM absorber consisting of a gold back reflector, SiO_2 dielectric spacer, and patterned gold front layer with thicknesses h_{AuBR} , h_{SiO_2} , and h_{AuFP} , respectively. (b) Definition of the in-plane geometrical parameters of the front gold pattern: R_{bead} is the radius of the spherical beads used in the NSL, and R is defined as the radius of curvature of the pattern, ΔR represents the difference between R and R_{bead} and can be adjusted in the fabrication. 2θ and $2d$ are the tip tapering angle and the distance between two neighboring tips, respectively. (c) Left: top-view scanning electron micrograph of a fabricated structure. Scale bar is 200 nm. Right: magnified top views of single tapered triangles. Scale bars are 50 nm.

well with our ellipsometry measurements (see Sample Fabrication).

3.4 Results and Discussion

The schematic representation of the absorber is given in Figure 3.2.a,b where all the relevant geometrical parameters are introduced. In particular, the schematic top-view of the front pattern is shown in Figure 3.2.b. R is defined as the radius of curvature of the pattern, and R_{bead} is the radius of the spheres (beads) which are used in the NSL and constitute a closely-packed hexagonal array. ΔR is defined as the difference between R and R_{bead} . For $\Delta R > 0$, the

3. Facile Multifunctional Plasmonic Sunlight Harvesting ...

front pattern consists of an array of disconnected gold triangles with curved sides. The neighbouring tapered triangles touch each other at a single point when $\Delta R = 0$. Due to overshadowing [35], experimentally $\Delta R > 0$ can be obtained and fine-adjusted by varying the etching time of the RIE process mentioned above. By doing this we can vary the size of the triangles and the tapering of their tips (2Θ , see Figure 3.2.b). A top view scanning electron micrograph of a created structure is shown in Figure 3.2.c.

The performance of the proposed absorber is illustrated in Figure 3.3.b-j where the measured and calculated absorption spectra are plotted for different values of ΔR (see Methods). The other geometrical parameters are fixed at $R_{bead} = 150$ nm, $h_{SiO_2} = 60$ nm (see Figure 3.3.a), and the thickness of the back reflector and the gold triangles are both equal to 100 nm. The overall structure is only 260 nm thick.

Both simulation and experimental data suggest that decreasing ΔR (equivalently decreasing 2Θ) increases the absorption bandwidth while maintaining a reasonably large absorption within the bandwidth. The best experimental result in terms of broadness is obtained at $\Delta R \approx 2$ nm (see Figure 3.3.j), for which the neighbouring tapered triangles tips are at the closest distance but still separated. Here, absorption stays above 85% within the spectral range 380 – 850 nm and slowly drops to 70% at 980 nm. We reach an average absorption slightly larger than 88% within the spectral range 380 – 980 nm. The numerical results in Figure 3.3.b show a rapid increase in the absorption bandwidth as ΔR approaches zero (equivalently, the distance between the tips of neighbouring triangles as well as Θ decrease). As explained in the Method section, ΔR can be controlled with nanometer resolution by using a slow enough etching process. While the fabrication relies on a facile method, the results show the potential of the proposed concept to easily adjust the absorption bandwidth and achieve a near-ideal absorber. Angular insensitivity is one of the important properties of an ideal absorber. The measured absorption spectra for the best experimental case (Figure 3.3.j) for incidence angles from 0 to 45° are summarized in Figure 3.3.k. The results show that a broad absorption spectrum is preserved even at large angles of incidence [37]. Finally, our design concept is inherently polarization insensitive at normal incidence. This is due to the geometrical planar symmetries that it contains. In addition, the measurements, which are performed with unpolarized light and the simulations confirm a similar insensitivity for angles away from the normal.

The broadband absorption behaviour of our design is the collective result of a number of plasmonic absorption events. These events occur at different locations of the spectrum and, after proper choice of the geometrical dimensions, piece together a continuous absorption band. To assess the impact of

3.4. Results and Discussion

the dielectric spacer thickness, in Figure 3.4.a we show the calculated absorption spectra for different values of h_{SiO_2} . All of the other geometrical parameters are kept constant ($R_{bead} = 150$ nm, $h_{AuFP} = 100$ nm, $\Delta R = 2$ nm, see Figure 3.3.a). The horizontal dashed line shows the situation that we have in the experiment, $h_{SiO_2} = 60$ nm (Figure 3.3.j), which leads to very high absorption over the entire absorption spectrum. Moving away from this optimal thickness leads to the appearance of spectral bands with high reflection in the visible range. To understand the origin of the broadband

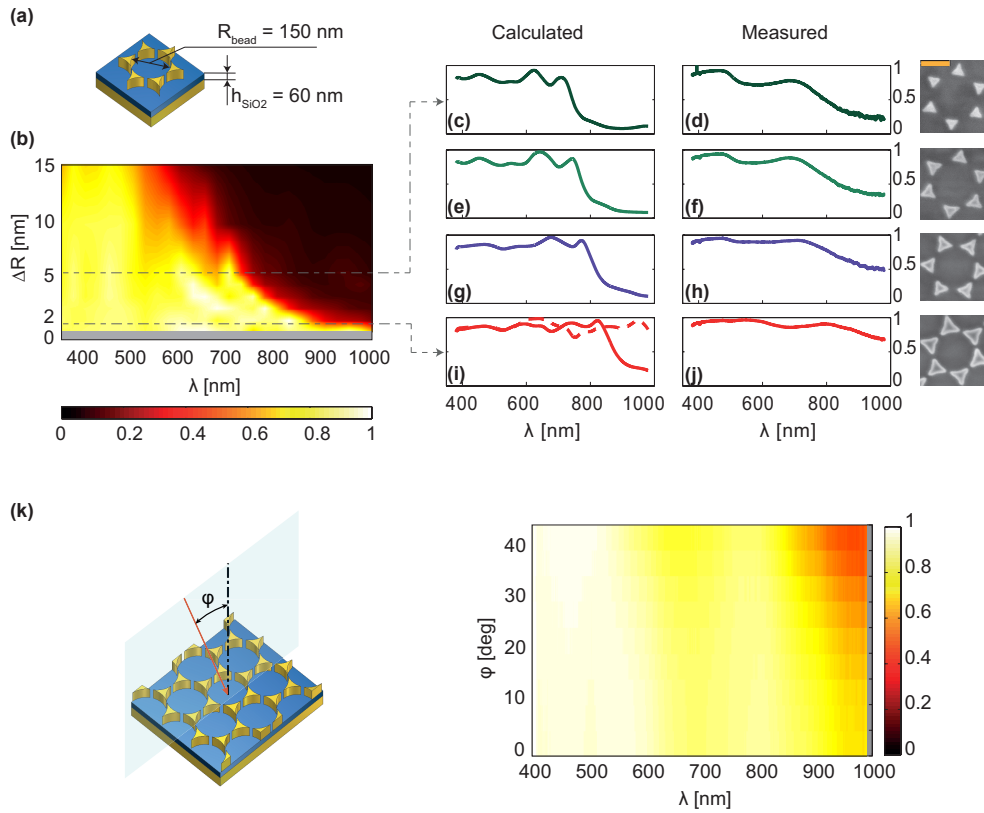


Figure 3.3: Measured and calculated absorption spectra of the absorbers. (a) Schematic representation of a unit cell of the absorber. In all studied cases R_{bead} and h_{SiO_2} are kept constant while ΔR is varied. (b) Simulated absorption plotted as a function of wavelength λ and ΔR . The absorption bandwidth is very large for small positive ΔR s. Simulations for ΔR between 0 nm and 1 nm turned out to be very challenging and beyond our capabilities (gray area). (c-j) Calculated (left column) and measured (right column) absorption spectra for different values of ΔR ; from top to bottom: $\Delta R = 6$ nm (c,d), 4 nm (e,f), 3 nm (g,h), 2 and 1 nm (i,j). The spectral response for the case of small ΔR becomes very sensitive to slight changes in this value. Therefore, the ultra-broadband absorption behavior observed in (j) can be viewed as the result of a superposition of different cases with slightly different ΔR values, two typical values of which are calculated in (i): solid ($\Delta R = 2$ nm) and dashed ($\Delta R = 1$ nm) lines. The SEM pictures on the right show unit cells of the fabricated structure for each case. Scale bar is 200 nm. (k) Left: schematic drawing of the absorber with light incident at an angle ϕ . Right: experimentally measured absorption plotted as a function of wavelength λ and angle of incidence ϕ . The objective used for excitation ($NA = 0.75$) allowed excitation angles up to $\phi = 48^\circ$.

3. Facile Multifunctional Plasmonic Sunlight Harvesting ...

absorption, we studied the field distributions inside the dielectric layer on two horizontal cross-sections, close to the top pattern and close to the back reflector. Figure 3.4.d shows magnetic field enhancement profiles at four absorption peaks indicated by P1P4 in Figure 3.4.a.

At P1 ($\lambda = 470$ nm) we note that the electromagnetic energy is concentrated close to the back-reflector. This indicates that the absorption at this wavelength originates from the grating-mediated coupling of electromagnetic field into the surface plasmon polariton (SPP) excited at the interface between SiO_2 layer and gold back reflector [38]. Our analytical calculations for the simplified three-layer (air- SiO_2 -gold) structure predicts the grating coupled SPP (corresponding to the grating period = $2R_{bead} = 300$ nm) at $\lambda = 498$ nm (see Figure 3.5.a,b), which is close to the observed resonance. This absorption resonance only slightly blue-shifts as the value of h_{SiO_2} increases. The absorption peak at P2 ($\lambda = 590$ nm) is substantially influenced by h_{SiO_2} and becomes weaker for SiO_2 thicknesses away from 60 nm. This peak red-shifts as h_{SiO_2} increases and is a result of a dipole-dipole interaction between the triangles and the gold back reflector [39]. The field profiles in Figure 3.4.d (P2) verify the contribution of both triangles and back reflector for this resonance. The absorption event at P3 is mainly originating from the localized surface plasmon (LSP) resonance of the individual tapered triangles. Our simulations of an isolated tapered triangle on a glass substrate reveal a dominant absorption peak for λ close to 720 nm (see Figure 3.5.c) which complies with the observed resonance at P3. The position of this absorption peak is only slightly influenced by h_{SiO_2} and the weak field enhancement on the back reflector confirms the dominant contribution of the individual triangles in the resonance (see Figure 3.4.d (P3)). Absorption at P4 originates from the presence of the tips where energy is accumulated and dissipated. This is evident from the strong field enhancement at the tips shown in Figure 3.4.d (P4). Further evidence for the above-mentioned attributes is given in Figure 3.4.b where calculated absorption spectra are plotted as function of R_{bead} . Here, by maintaining the ratio $\Delta R/R_{bead}$ constant, we are able to keep the tip angle, 2Θ , constant and equal to 18.6° . In fact, as illustrated in Figure 3.2.b, the angle Θ is half of the opening angle of the tips of the triangles. Employing the definition of similar triangles in Euclidian geometry, we define similar concave triangles having the same tip opening angle, 2Θ . It can be easily observed that keeping the ratio $\Delta R/R_{bead}$ constant leads to a constant Θ and therefore, similar curved triangles. On the other hand, decreasing ΔR for a given R_{bead} , leads to smaller Θ values and therefore, sharper tips. Decreasing ΔR also yields smaller d values (closer tips). Other geometrical values are $h_{SiO_2} = 60$ nm, and $h_{AuFP} = 100$ nm. The two eye-guiding lines show the variation of the position of the resonances

3.4. Results and Discussion

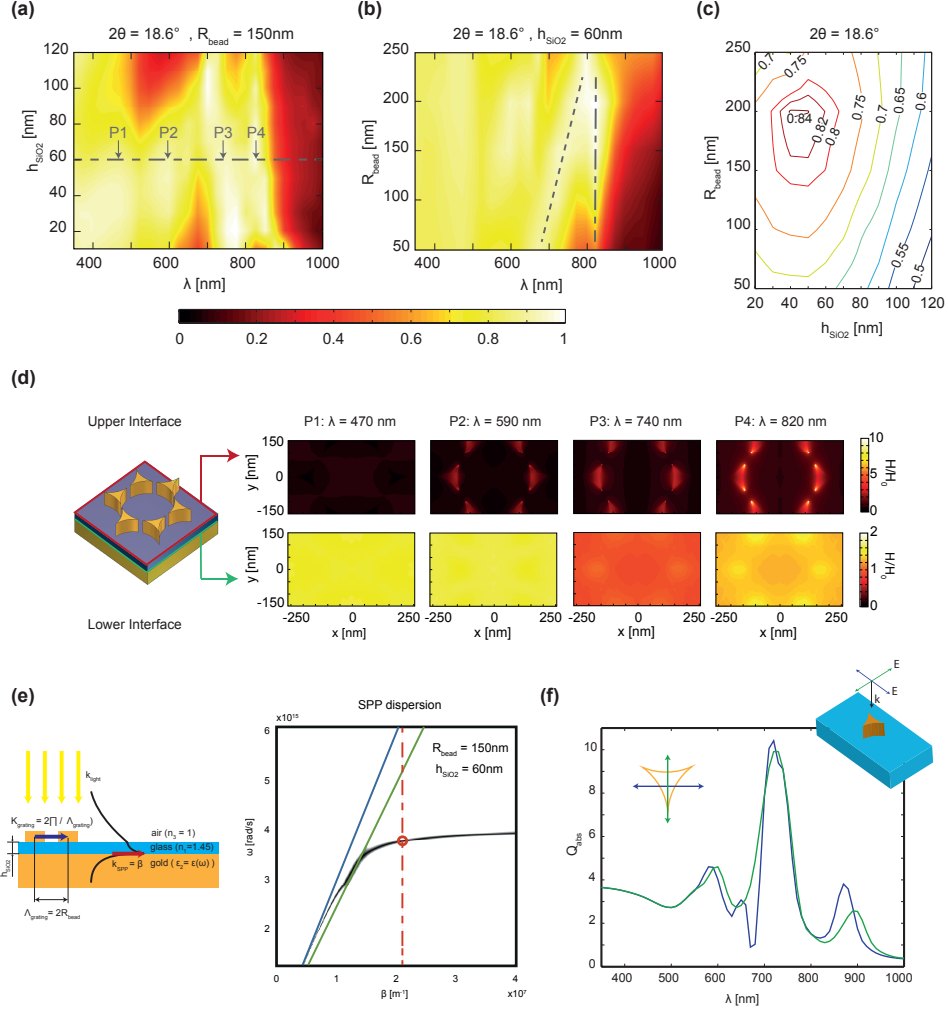


Figure 3.4: Absorption spectra vs. geometrical parameters and field profiles. (a) Simulated absorption spectrum as a function of h_{SiO_2} for $R_{bead} = 150$ nm, $h_{AuBR} = h_{AuFP} = 100$ nm. The dashed line indicates the best case, which also corresponds to the experimentally realized absorber. The arrows P1–P4 indicate the position of the main absorption peaks. (b) Simulated absorption spectrum as a function of R_{bead} for $h_{SiO_2} = 60$ nm, $h_{AuBR} = h_{AuFP} = 100$ nm. The eye-guiding dotted and dotted-dashed lines show the change in the absorption peaks corresponding to P3 and P4, respectively. (c) Contour plot showing total absorption of sunlight, A_{tot} , as a function of geometrical parameters R_{bead} and h_{SiO_2} . In order to compare similar tip geometries, $\Delta R/R_{bead}$ is kept constant and equal to 0.0133 ($2\theta = 18.6^\circ$). Absorption is calculated within the spectral range 350 – 1000 nm assuming the solar irradiance for the standard AM1.5 (air mass) spectrum. (d) Normalized magnetic field (H) profiles at two cross-sections within the SiO_2 layer for the cases specified by P1–P4 in (a) (upper cross-section: interface between the front Au pattern and the SiO_2 layer; lower cross-section: interface between the SiO_2 layer and the gold back reflector) (e) Schematic representation of grating-coupled SPP excitation for the multilayer air-glass-gold system. In the case of normal incidence the condition $\beta = K_{grating}$ has to be satisfied. Black curve: SPP dispersion curve for the multilayer system illustrated in part (a). Blue line: air light line. Green line: glass light line. Dash-dotted vertical line: $\beta = K_{grating}$ for the case of $R_{bead} = 150$ nm. The frequency ω is the intersection of the black curve and the vertical line (red circle, $\omega = 3.779e15$ rad/s corresponding to $\lambda = 498$ nm). (f) Calculated absorption efficiency, Q_{abs} , for an isolated tapered triangle on glass, excited with two different polarizations. The tapered triangle has the same dimensions as the triangles in an array with $R_{bead} = 150$ nm, $\Delta R = 2$ nm and $h_{AuFP} = 100$ nm. Inset: 3D graphical representation of the simulated geometry.

3. Facile Multifunctional Plasmonic Sunlight Harvesting ...

corresponding to P3 and P4 (see Figure 3.4.a). The resonance corresponding to P3 (dotted line) red-shifts as R_{bead} increases. This is in agreement with the expected red-shift of the LSP resonance of the triangles as their size (or equivalently R_{bead}) increases [40]. On the other hand, the invariance of 2Θ ensures a practically unchanged spectral position of the absorption peak corresponding to P4 (dashed-dotted line), although R_{bead} and $2d$ (see Figure 3.2.b) vary over a large range. As expected from previous studies [41], the focusing of the electromagnetic energy at the end of tapered tips is sensitive only to the tip opening angle. The spectral position of this absorption peak determines the upper cut-off of the absorption band and as seen in Figure 3.3.b can be greatly increased by decreasing the tip angle, 2Θ .

To conclude our study, we briefly consider the effect of a negative ΔR , that, as illustrated in Figure 3.5.a, implies a physical connection between the neighboring triangles and therefore the disappearance of the tips. Similarly to Figure 3.3.b, in Figure 3.5.b we show the absorption spectrum as a function of the wavelength and $\Delta R \leq 2$ nm, being $\Delta R = 2$ nm the best result we could obtain experimentally. Also, in Figure 3.5.c-h we directly compare the numerical and experimental results obtained at different values of ΔR . We immediately observe that the absorption bandwidth abruptly drops as soon as the tips of the gold tapered triangles merge ($\Delta R < 0$). Indeed, more than 250 nm drop in bandwidth at longer wavelengths occurs as ΔR is varied from 1 nm to -1 nm. This result is in agreement with

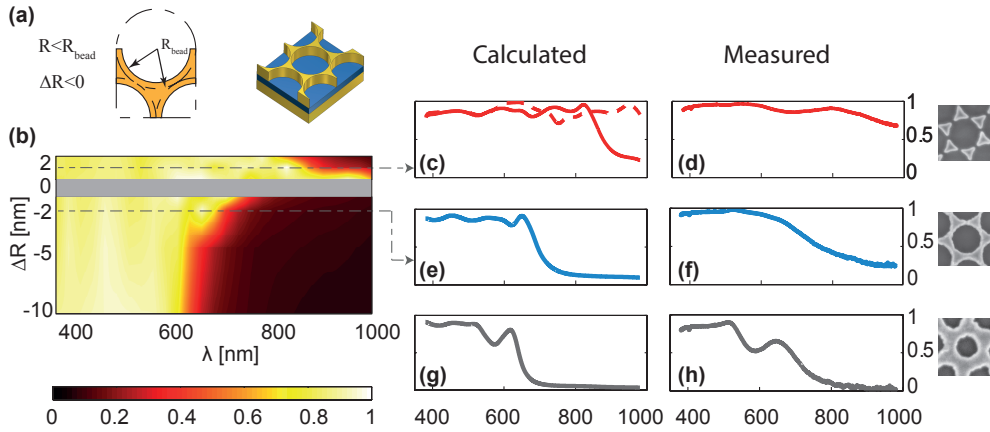


Figure 3.5: Measured and calculated absorption spectra of the absorber upon connection. (a) Schematic representation of the condition upon which connection is achieved. (b) Simulated absorption plotted as a function of wavelength λ and ΔR for negative values of ΔR . The optimal absorber case is reported for comparison. The drop in absorption bandwidth is clearly visible. (c-h) Calculated (left column) and measured (right column) absorption spectra for different values of ΔR ; from top to bottom: $\Delta R = 1$ nm (c,d), reported for comparison, -1 nm (e,f), -50 nm (g,h). The SEM pictures on the right show unit cells of the fabricated structure for each case. Scale bar is 200 nm.

3.5. Conclusions

our previous observations considered that the sudden disappearance of the triangular entities together with the suppression of the tips have a dramatic effect on the absorption spectrum (an analogous behavior will be discussed in detail in Chapter 4). Therefore we conclude that the optimal design requires disconnected triangular elements as front pattern.

In order to assess the performance of our concept in absorbing the solar spectrum, we calculate the total absorption as:

$$A_{tot} = \frac{\int_{350nm}^{1000nm} A(\lambda)I(\lambda)d\lambda}{\int_{350nm}^{1000nm} I(\lambda)d\lambda} \quad (3.1)$$

where $A(\lambda)$ and $I(\lambda)$ are the absorption of the structure and the solar irradiance for the standard AM1.5 (air mass) spectrum, respectively. In calculating the above absorption we consider the spectral range of 350 – 1000 nm, for which we performed measurements and simulations. The discarded part contains around 25% of the total solar energy. The contour plot in Figure 3.4.c shows the simulated total absorption as a function of thickness of the SiO_2 layer, h_{SiO_2} , and the size of the beads used for NSL, R_{bead} . In these simulations we used a constant value for $\Delta R/R_{bead} = 0.0133$, corresponding to $\Delta R = 2$ nm at $R_{bead} = 150$ nm), to ensure a constant angle at the tips of the triangles, 2Θ . Based on the above-mentioned studies, this assumption ensures almost the same upper cut-off wavelength of the absorption band for all the cases. The optimal geometry with $R_{bead} = 200$ nm and $h_{SiO_2} = 45$ nm leads to a total absorption of 84%. As explained before (see Figure 3.3.b), smaller values for ΔR can lead to substantially broader absorption spectrum and therefore increase the total absorption. Furthermore, Figure 3.4.c shows that the total absorption around the optimum is quite insensitive to h_{SiO_2} and R_{bead} , making the performance of such a device highly tolerant to fabrication imperfections.

3.5 Conclusions

In conclusion, exploiting a combination of different plasmonic absorption phenomena in an array of tapered triangles integrated in an MIM configuration, we introduced a novel ultra-broadband plasmonic absorber with average absorption 88% within the spectral range 380 – 980 nm. In addition, this absorber is insensitive to both light polarization and angle of incidence. While aspects of light absorption by arrays of tapered triangles have been studied before, our results contain significant novelty based on exploiting simultaneously four distinct absorption phenomena (each of different nature) two of

3. Facile Multifunctional Plasmonic Sunlight Harvesting ...

which are accessible only through the MIM configuration. Properly selecting a host of geometrical dimensions, we managed to harvest the collective benefit of these absorption events and pieced together a continuous absorption band. Our simulations show that one could go even beyond these high values, in terms of broadness and total absorption, by fine-tuning of the geometrical parameters, specifically the tip regions of the tapered triangles in the pattern. Importantly, in contrast to previous successful designs, the fabrication of our concept is based on NSL which is a low-cost and easily accessible method. [32, 34]. Although monocrystallinity is not a stringent requirement in our design, achieving large defect-free crystals with NSL remains a challenge. This bottleneck has been addressed in recent studies [42, 43] and significant improvements are foreseen. To this end, and based on the nano-scale thickness (260 nm) of our design, we envision the up-scaling of the absorber on flexible substrates even in a roll-to-roll manner. Being ultra-thin, the absorber can efficiently and rapidly elevate the temperature within a nano-scale layer, which can be exploited in various applications such as micro-fluidics [44], solar thermoelectrics [21, 45, 16], and high temperature chemical reactions [46]. In addition, efficiently absorbing the extremely broad solar light and concentrating it at the very end of the tips, renders the present concept an interesting candidate for enhancing solar-based photochemistry and improving the efficiency of solid-state devices [19, 17, 20, 18].

Chapter 4

Proximal Gap Plasmon Nanoresonators in the Limit of Vanishing Inter-Cavity Separation

Part of this chapter has been accepted for publication in *Nanoscale*

4.1 Abstract

Nanostructured metal-insulator-metal (MIM) metasurfaces supporting gap-plasmons (GPs) show great promise due to their ability to manipulate or concentrate light at the nanoscale, which is of importance to a broad palette of technologies. The interaction between individual, proximal GP nanoresonators, reaching the point of first electrical connection, can have unexpected, important consequences and remains unexplored. Here we study the optical properties of a GP-metasurface in the limit of diminishing spacing between GP nanocavities and show that it maintains its nanoresonator array character, with negligible GP interaction, even at extremely close proximity between cavities. Then, at the point where inter-cavity electrical connection is first established, the surface abruptly transforms into a patterned metal-insulator-metal waveguide. We report detailed experimental evidence and explain the underlying physics through computational modeling, based on the properties and inherent symmetries of the electromagnetic field of the investigated metasurface. The novel phenomenon explored here can have a host of potential applications in the field of active plasmonic metamaterials, plasmonic photocatalysis and ultra-sensitive sensors.

4.2 Introduction

Metasurfaces based on film-coupled nanoantennas supporting gap-plasmons have been proposed in recent years for an increasing number of applications ranging from perfect [47, 37] and broadband [48] absorbers to negative refractive index materials [49, 50], various optical components (e.g. beam splitters [51]) and ultra-sensitive biosensors [52]. Indeed, slow gap-plasmons (GPs) in truncated metal-insulator-metal (MIM) structures exhibit a desirable combination of several properties including deeply subwavelength mode volume [47, 53], direct far-field excitation with planar waves, insensitivity to excitation polarization and angle of incidence [9, 10], and ease of resonance tunability [49]. Furthermore, such metasurfaces require only a patterned front metal layer with no regular periodicity and can be easily fabricated with standard lithographic methods and even colloidal techniques [10].

The fundamental role of near-field interaction and establishment of a conductive contact between electrically isolated elementary plasmonic structures (e.g. spheres, disks) has been widely studied both experimentally and theoretically [54, 55, 56, 57, 58]. These studies showed significant spectral shifts due to near-field coupling as well as pronounced changes in the optical properties of the connected system depending on the electrical properties of the junction (both conductivity and conductance). Furthermore, a recent study on the transition from a non-concentric ring to a nano-crescent pattern, reported significant effects of charge accumulation and symmetry breaking on the corresponding optical properties [59]. Arrays of gap plasmon nanocavities consist of a continuous back metal reflector separated from a discrete front metallic layer by a thin dielectric. While the back metal layer constitutes a channel for free propagation of charges, the front discrete structures are electrically insulated and must satisfy charge neutrality. The in-plane terminations of the patterned front metal layer are responsible for the gap-plasmon mode reflection and the formation of a strongly confined standing wave in the ensuing nanocavity [9]. Establishing conductive connections between the front discrete patterns would then allow the waves to travel to neighboring nanocavities, dramatically changing the properties of the overall system, yet it remains largely unexplored.

In this chapter, we experimentally and numerically study the interaction between GP nanocavities in a two-dimensional array and demonstrate the dramatic impact of a possible realization of electrical contact between the elements of the front pattern. The choice of geometry and its fabrication facility allows us to progressively reduce the inter-cavity distance and finally establish electrical connections, which are as narrow as 15 nm in terms of the physical dimension of the contact between the nanocavities. These electrical

connections transform suddenly the array of truncated nanocavities to an infinite MIM waveguide network. We show that while the communication between the discrete cavities before contact is negligible even at very close proximity, reaching the point of electrical connection leads to strong interactions between them and consequently to an abrupt change in the absorption spectrum of the metasurface. Furthermore, we identify the origin of such a drastic shift of optical properties in the different boundary conditions the excited gap plasmons experience in the disconnected and connected states, respectively.

4.3 Methods

4.3.1 Sample Fabrication

The studied multilayer structure is composed of a silver back reflector, a SiO_2 spacer layer with thickness and a front hexagonal array of tapered gold triangles, Figure 4.2.a, which are fabricated using a combination of standard nanosphere lithography (NSL) and etching techniques [32, 33] (Figure 4.1.a).

On a clean glass slide (18×18 mm) we deposited 5 nm Ti (adhesion layer), 100 nm Ag and 7–13 nm of SiO_2 using e-beam evaporation. We then dip-coated the sample in an aqueous solution of 300 nm polystyrene beads (1% wt bead concentration, 10^{-3} M SDS surfactant) forming a monolayer (process parameters: 50% humidity, $1.1 \mu\text{m/s}$ withdrawal speed). Next, we used reactive ion etching (100 sccm Ar, 10 sccm O_2 , 50 W, 100 μbar) to reduce the size of the beads (from 35 s up to 100 s), which then act as a mask for the final gold e-beam evaporation (100 nm) (Figure 4.1.a). No adhesion layer was used in this case to avoid perturbing the system, which is very sensitive to the spacer layer thickness. Finally the beads were removed with a gentle water jet. The resulting front pattern depends on the etching time and, as illustrated in Figure 4.1.b, we can create either an array of disconnected triangles with variable size (etching time up to 68 s, Figure 4.1.b,top) or a continuous patterned metal layer (etching time longer than ≈ 100 s, Figure 4.1.b,bottom). For intermediate etching times fabrication imperfections lead to a only partially connected structure.

The periodicity of the array, $D_p = 300$ nm (Figure 4.2.a), was chosen in order to obtain the main spectral features of the structure in the visible regime. The large thickness of the two metallic layers help avoid excitation of coupled plasmon modes other than the studied gap plasmon mode.

4. Proximal Gap Plasmon Nanoresonators ...

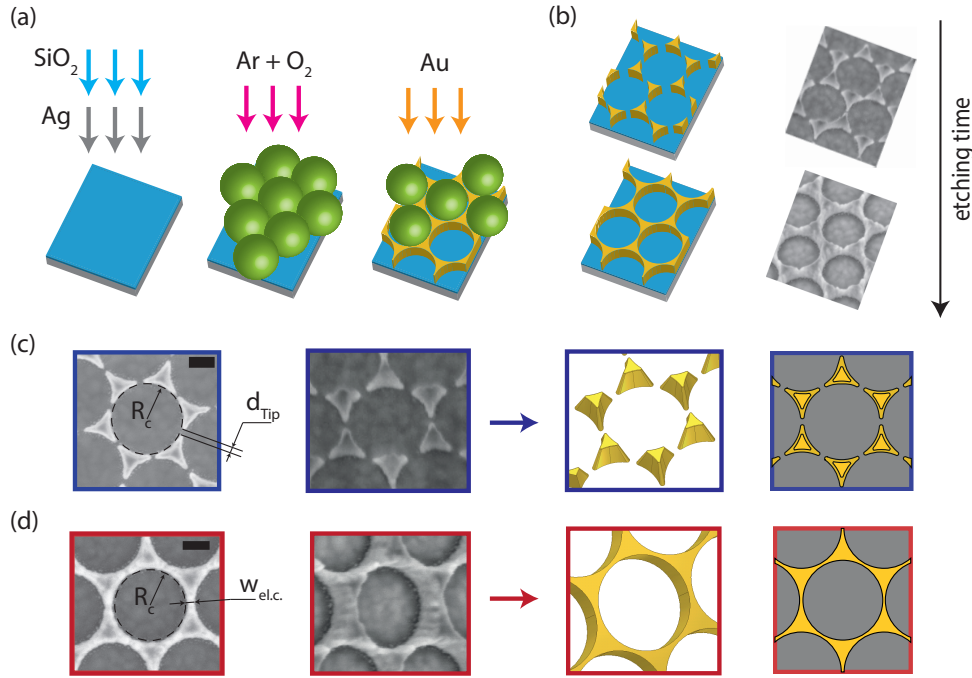


Figure 4.1: Fabrication Procedure and Definition of the Numerical Geometry (a) Steps of the multilayer structure fabrication: silver and glass deposition (left), polystyrene sphere monolayer formation and reactive ion etching (middle), gold deposition (right). (b) Effect of the etching time on the resulting structure. (c) Determination of the radius of curvature of the triangles R_c , the mean inter-tip distance d_{Tip} and the electrical connection width $w_{el.c.}$ from SEM micrographs (scalebar 100 nm). Micrographs also show that the structure has tilted side walls. (d) Same procedure for the connected front pattern (scalebar 100 nm)

4.3.2 Optical Measurements

The optical measurements were performed with the same experimental set-up and methodology described in Section 3.3.2.

4.3.3 Numerical Modeling

Geometry Definition

As illustrated in Figure 4.1.c,d we used SEM micrographs to extract approximate geometric parameters and we then defined a simplified geometry that we used to study the evolution of the optical properties between disconnected and connected nanocavities.

In the disconnected nanocavity array we estimated the mean inter-tip distance (d_{Tip}), the curvature of the triangle sides (R_c) and the width of the established electrical connection $w_{el.c.}$ (Figure 4.1.c, 4.2.a). Experimentally, the largest nanocavities we fabricated before connection (etching time of

4.3. Methods

68 s, Figure 4.1.b,top) had $2 \cdot R_c$ between 280 nm and 290 nm and mean d_{Tip} approximately between 20 nm and 25 nm. From tilted SEM images we also observed that our front structure has tapered sides and thus a smaller top than bottom surface. As will be explained later, tilted walls have to be considered and we numerically verified that the GP nanocavity behavior is negligibly influenced by the upper triangle surface. We then defined a standard front surface ($R_{c,top} = 155$ nm), which was left unchanged for all cases.

In the connected array case (Figure 4.1.d) we assumed an ideal flat bridge filling the gap between the original nanocavities. The width of the obtained electrical connection is equal to the difference between the array periodicity ($D_p = 300$ nm) and the diameter of curvature of the structure ($2 \cdot R_c$). Experimentally (etching time of 100 s, Figure 4.1.b,bottom), we obtained connection widths between 15 nm and 25 nm. We also verified numerically that the optical properties of the structure have limited sensitivity to the width of the connection in the range obtained experimentally.

For the simulations reported in Figure 4.2.c,d we then simplified the geometry fixing $2 \cdot R_c = 285$ nm and varying only the inter-tip distance from 24 nm (approximately the minimal experimental value) to touching and connection.

Array and Isolated Structure Simulations

All the simulations were performed using the COMSOL Multiphysics package (RF module), which is based on the finite element method (FEM). In all simulations we assumed planar normal illumination. The dielectric properties of the metals were taken from the literature [36, 60] while the refractive index of glass was measured with ellipsometry to be 1.45.

For the array of GP nanocavities we used symmetry boundary conditions to reduce the computational domain to one-fourth of a unit-cell. We used a port boundary condition to excite the system with normal illumination and we solved for the total fields.

For the isolated GP nanocavity we defined a large enough domain ($\approx (3 \cdot D_p) \times (3.5 \cdot D_p)$) that we then halved using the symmetry plane perpendicular to one of the triangle base heights. We used a port boundary condition to excite the system with normal illumination and we first solved for the background field (excluding the front nanostructure). In a second step we re-activated the front nanostructure and computed the scattered as well as total fields. In this second computation perfectly matched layers (PMLs) surrounded the computational domain (apart from the symmetry plane).

4.4 Results and Discussion

In order to study the gradual transition from isolated GP nanocavities to an infinite MIM waveguide, we consider a regular array of such cavities, where minute electrical connections can be achieved simultaneously over the entire array with minimal changes in the size and shape of the original nanocavities. Moreover, an ultrathin dielectric spacer is necessary in order to maximize the GP confinement effect [47, 10] and avoid mode delocalization [9] even for small nanocavity separation.

Figure 4.2.a illustrates the chosen structure which satisfies all the above-mentioned criteria (see Section 4.3.1). The inter-cavity distance d_{Tip} , can be experimentally adjusted with the etching time and, for a constant periodicity D_p , it relates directly to the cavity size. When d_{Tip} is larger than zero the nanocavities are considered to be electrically disconnected and when it is equal to zero the tips of the triangles in the top gold structure come into contact and electrical connection between the neighboring nanocavities is just established (see Section 4.3.3). In this chapter we refer to the former case as disconnected structure and to the latter case as connected structure.

The measured absorption spectra for connected and disconnected GPs excited with normal incidence are shown in Figure 4.2.b. Here, d_{Tip} is around 20–25 nm for the disconnected GPs and the established electrical connection has a width of approximately 15–20 nm (see insets). A drastic blue-shift in the absorption peak is observed: while the array of disconnected nanocavities has an absorption peak at wavelength $\lambda_1 = 890$ nm, the connected GPs spectrum shows a narrower absorption peak at $\lambda_2 = 660$ nm.

To investigate further this finding theoretically, we performed computational simulations (see Section 4.3.3). The two curves in Figure 4.2.d are the results of the simulations corresponding to the experimental cases (blue curve, $d_{Tip} = 24$ nm; red curve, $d_{Tip} = 0$ nm and 15 nm wide electrical connection) and show that the numerical model predicts the spectral position of the measured absorption peaks. Lower measured absorption peaks and their broadening as compared to simulations are attributed to inherent fabrication imperfections, such as slight non-uniformity of the structures and surface roughness.

We also simulated structures with smaller values of d_{Tip} . Figure 4.2.c shows the calculated absorption spectra for inter-cavity distances ranging from the experimental value (≈ 24 nm) until connection. For d_{Tip} values greater than zero (disconnected cavities) the low energy resonance (indicated with 1 in Figure 4.2.c) continuously red-shifts as d_{Tip} decreases. However, upon finite electrical connection ($d_{Tip} = 0$ nm, connection width 15 nm) the low energy absorption peak is suppressed and a higher energy peak emerges

4.4. Results and Discussion

(denoted by 2 in Figure 4.2.c). In the disconnected nanocavity case, a higher energy peak is denoted by 3 and will be discussed later.

Numerically, we verified (Figure 4.3) that the same abrupt transition between disconnected and connected nanocavities takes place even for extremely narrow electrical connections with width of 2 nm, which is approaching the limit of a point-like contact. Simulations of smaller widths have little physical significance due to the onset of complex non-local material responses, requiring dedicated numerical modeling [61]. The origin of the high energy absorption peak of the disconnected case, which is very pronounced in this case, will be explained later.

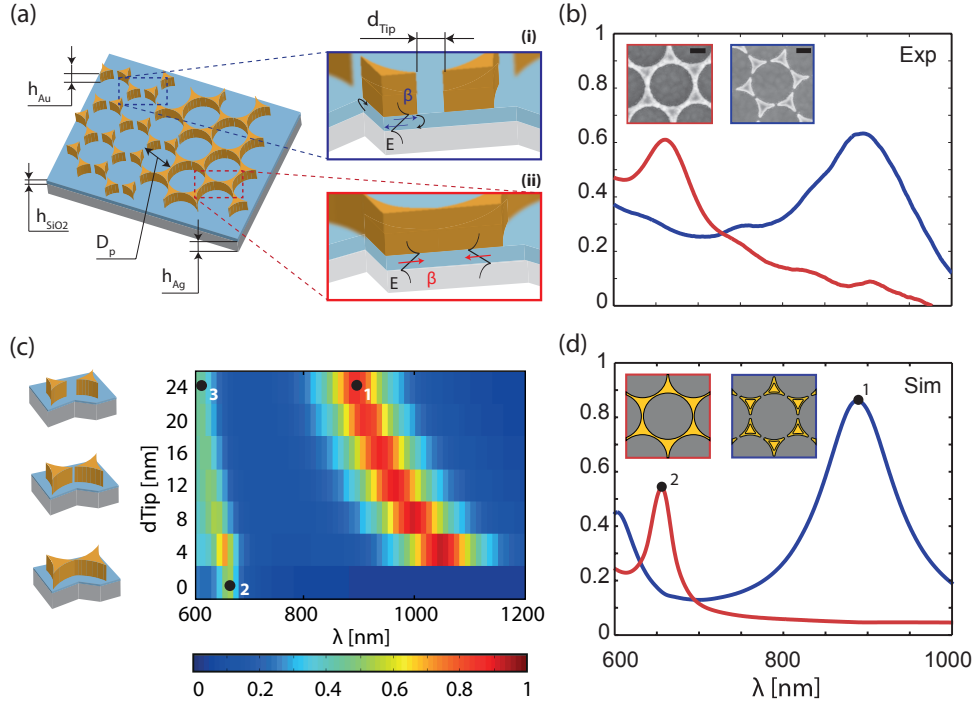


Figure 4.2: Geometric Parameters and Optical Properties of the Metasurfaces before and after Electrical Connection. (a) Geometry description. In the studied case we used $h_{SiO_2} = 13$ nm, $h_{Ag} = 100$ nm, $h_{Au} = 100$ nm and $D_p = 300$ nm. Inset (i) GP mode reflection at the nanocavity terminations in the disconnected case. Inset (ii) GP mode propagation in the connected case. (b) Experimental absorption spectra of the disconnected (blue curve, $d_{Tip} = 20 - 25$ nm) and connected (red curve, electrical connection width of 15 – 20 nm) gap plasmon nanocavities. Insets show SEM micrographs of the experimental structures (scale bars 100 nm). (c) Calculated absorption spectra of the array of gap plasmon nanocavities upon reduction of the tip-to-tip distance between the cavities (enlargement of the system). The two extremes of the graph correspond to the experimental cases, with $d_{Tip} = 24$ nm for the disconnected geometry, and 15 nm wide electric connection in the final configuration (see Figure 4.1 for details). The peaks indicated with 1 and 2 are the studied modes of the disconnected and connected cases respectively. A higher energy peak is indicated with 3 and is discussed in Supplementary Information S6. (d) Calculated absorption spectra corresponding to the experimental case in b ($d_{Tip} = 24$ nm, blue curve, and 15 nm wide electrical connection, red curve).

4. Proximal Gap Plasmon Nanoresonators ...

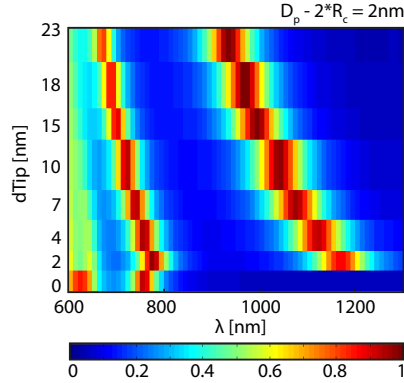


Figure 4.3: Absorption spectrum evolution from discrete to connected nanocavities with ultra-narrow, point-like connections. ($D_p - 2 \cdot R_c = 2$ nm).

Before studying the physics underlying the observed abrupt change, we investigate further the behavior of the array of electrically disconnected nanocavities. In this case, each nanocavity formed between a front triangle and the back-reflector supports a gap plasmon mode which is the result of two counter-propagating MIM waveguide modes continuously reflected at the extremities of the cavities, i.e. the tips of the triangles (Figure 4.2.a(i)). The disconnected GP modes are then determined by simultaneously satisfying the odd MIM dispersion relation, $\beta(\omega, h_{diel})$ [4] and the Fabry-Perot interferometer condition [9], $L_{cav} \cdot \beta = m\pi - \phi$ (see Figure 4.4.c), where L_{cav} is the cavity size, β is the propagation wavevector of the mode, m the mode order and ϕ the phase acquired upon reflection at the cavity terminations (Figure 4.2.a(i)).

The waveguide nature of the GP mode, represented by the first condition, makes the mode sensitive to the dielectric spacer thickness with the resonance peak red-shifting upon reduction of h_{SiO_2} (Figure 4.4.a-c)[4]. This trend allows for extreme light confinement by coupling far-field plane waves to cavities with thicknesses which are 2 – 3 orders of magnitude smaller than the light wavelength [47]. In our case we achieve a resonance wavelength to thickness ratio of 127 (Figure 4.4.a, resonance wavelength 890 nm, $h_{SiO_2} = 7$ nm).

For a given h_{SiO_2} , as d_{Tip} is reduced, the effective length of the nanocavities (L_{cav}) increases and, due to the Fabry-Perot interferometer condition, the resonance peak is red-shifted [49, 9], as observed in Figure 4.2.c. In order to quantify the effect of cavity size on the spectral position of the resonance upon variation of d_{Tip} , we perform an approximate calculation which makes direct use of the Fabry-Perot condition. From the graph in Figure 4.2.c we can extract the resonance wavelength, λ_{res} , for each value of d_{Tip} .

4.4. Results and Discussion

As explained previously, knowing the resonance wavelength and the dispersion curve (see Figure 4.4.c), we can calculate the wavevector β_{res} of the excited gap-plasmon mode, that is $\beta_{res} = \beta(h_{SiO_2} = 13\text{nm}, \lambda_{res})$. Further, we calculate an effective cavity size, L_{cav} , at resonance, by assuming perfect reflection, $\phi = 0$, a first-order mode, $m = 1$, and using the Fabry-Perot condition: $L_{cav} \cdot \beta = m\pi - \phi$, thus obtaining the relation $L_{cav} = \frac{\pi}{\beta_{res}}$. The calculated values are reported in the table 4.1.

d_{Tip}	λ_{res}	β_{res}	L_{cav}
4 nm	1040 nm	$1.976 \cdot 10^7$	159 nm
8 nm	990 nm	$2.092 \cdot 10^7$	150 nm
12 nm	960 nm	$2.168 \cdot 10^7$	145 nm
16 nm	930 nm	$2.25 \cdot 10^7$	140 nm
20 nm	900 nm	$2.339 \cdot 10^7$	134 nm
24 nm	890 nm	$2.371 \cdot 10^7$	133 nm
46 nm	800 nm	$2.716 \cdot 10^7$	116 nm

Table 4.1: Calculated values of the effective cavity size, L_{cav} , for the disconnected nanocavities with different d_{Tip} values

The results of table 4.1 are visualized in Figure 4.4.g. Indeed, we overlay on top of the magnetic field profiles at resonance (see also Figure 4.2.c) a circle whose diameter is given by $D_{eq} = L_{cav}$. We clearly see that, as the physical size of the cavity shrinks, the effective cavity size predicted by the Fabry-Perot model also shrinks. Moreover, we observe that the calculated L_{cav} almost precisely predicts the extent of the cavity mode for all the cases. In particular, the two right most field profiles ($d_{Tip} = 24$ nm and 46 nm) correspond to the resonances of the simulated spectra in Figure 4.4.e which very well agree with the experimental results reported in Figure 4.4.d. In particular, in Figure 4.4.d,e a red-shift of around 80 nm is observed both in theory and experiment as d_{Tip} varies from 46 nm to 24 nm.

In order to assess the interaction between individual GPs, we compare the simulated absorption spectrum of a single GP nanocavity including only one triangle with that of the compact hexagonal arrangement. The normalized absorption spectra of the single GP (dotted curves) are overlaid on top of the absorption spectra of the arrays (solid curves) in Figure 4.4.e. For both cases of $d_{Tip} = 24$ nm and 46 nm, the single cavities and the cavity arrays have very similar spectral position of the absorption peaks. Since this resonance peak wavelength is solely determined by the two above-mentioned criteria, MIM dispersion relation [4] and Fabry-Perot resonance condition [9], both single cavity and cavity array GPs experience the same boundary conditions at resonance. In other words, the nanocavities do not interact

4. Proximal Gap Plasmon Nanoresonators ...

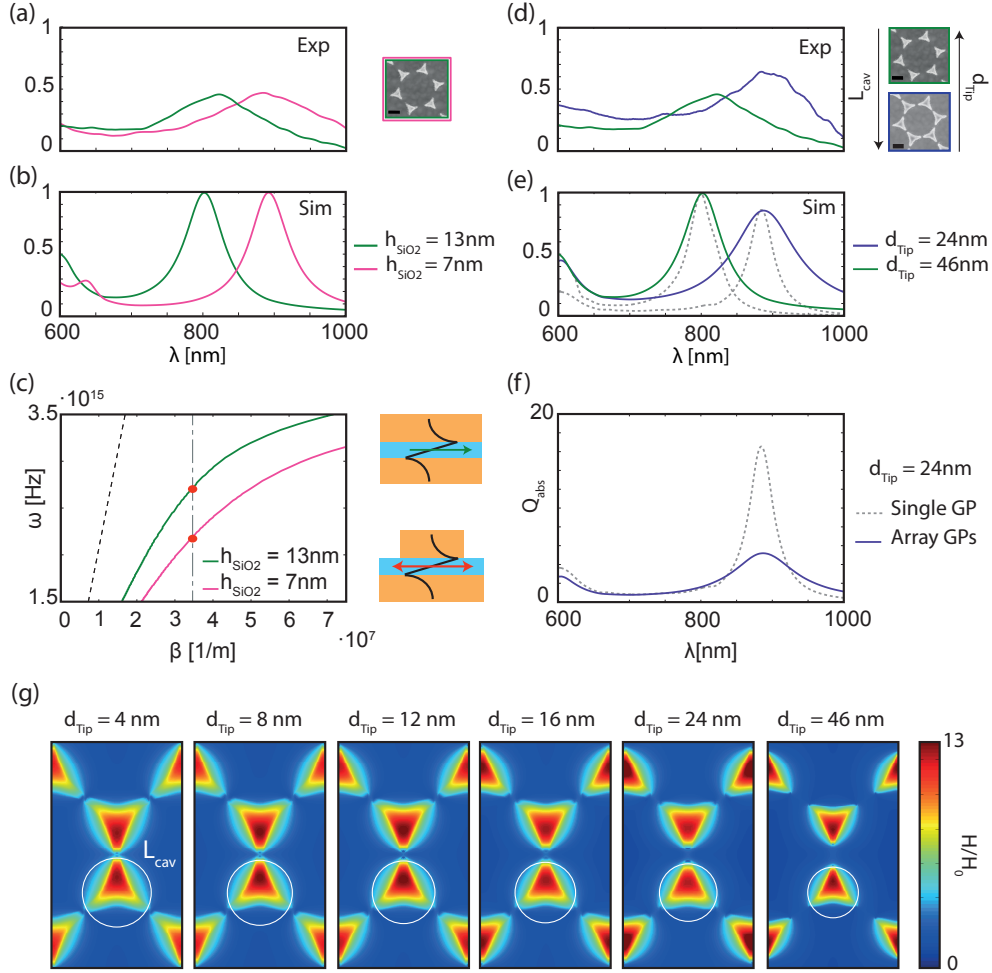


Figure 4.4: Fundamental Gap Plasmon Resonance of the Disconnected Nanocavity Array. (a) Experimental and (b) simulated absorption spectra of arrays of disconnected cavities with different dielectric spacer thicknesses (green curve $h_{SiO_2} = 13$ nm, pink curve $h_{SiO_2} = 7$ nm). (c) Calculated dispersion curves of a MIM waveguide (top schematics) for two SiO_2 thicknesses (green curve $h_{SiO_2} = 13$ nm, pink curve $h_{SiO_2} = 7$ nm). The dashed-dotted line represents a possible value of the wavevector given by the Fabry-Perot condition in a truncated MIM waveguide (bottom schematics). The red-dots indicate the frequencies which satisfy both the waveguide and Fabry-Perot conditions in the different truncated systems and therefore correspond to the resonance frequencies. (d) Experimental and (e) simulated absorption spectra of disconnected cavities with different inter-cavity distance, d_{Tip} (green curve $d_{Tip} = 46$ nm, blue curve $d_{Tip} = 24$ nm) corresponding to different cavity sizes, L_{cav} . Dashed curves represent the normalized spectrum of an isolated triangle with the same dimensions as the triangles in the array considered. Insets show SEM micrographs of the measured structures (scalebars 100 nm). (f) Absorption efficiency of the array (blue curve) with $h_{SiO_2} = 13$ nm and $d_{Tip} = 24$ nm and the corresponding single nanocavity (dashed gray curve). (g) From left to right: magnetic field profiles at resonance and circles indicating the effective cavity sizes for the structures with d_{Tip} equal to 4 nm, 8 nm, 12 nm, 16 nm, 24 nm and 46 nm and therefore, correspondingly reducing physical cavity size.

4.4. Results and Discussion

even at tip-to-tip distances as close as 24 nm. However, in the closely packed arrays, overlapping absorption cross-sections lead to absorption broadening as compared to single GP nanocavities. In Figure 4.4.f we see that in the array configuration each triangle can have a maximal absorption cross section approximately 5.2 times larger than its physical cross section and this limitation comes directly from the geometry of the array. In the isolated configuration, at resonance, the absorption cross section is instead close to 16 times larger than the physical cross section of the triangle. Indeed, the difference in absorption bandwidth is less pronounced for smaller cavities (Figure 4.4.d, green curves) than for larger nanocavities (Figure 4.4.d, blue curves) as their individual absorption cross-sections are smaller and therefore have a lower degree of overlap in the array configuration.

Negligible interaction between closely spaced GPs is in stark contrast to plasmonic systems consisting of two or several nanoparticles, which experience very large collective effects starting at distances below few tens of nm [62]. Lack of interaction between neighboring closely packed GPs makes such a system a promising candidate for integrated photonic circuits where isolation between neighboring components is highly desirable.

Given the remarkable isolation properties of disconnected ultrathin GP nanocavities, the only path leading to a substantial interaction between them is the physical connection of the front pattern (i.e. triangles). Due to the established electrical connections, GP modes will now be able to propagate into the previously discrete neighboring nanocavities (Figure 4.2.a(ii)) and the Fabry-Perot resonance criterion is no longer relevant. Upon this transformation, as shown in Figure 4.2, the optical properties of the metasurface undergo abruptly a transformative change.

To understand the origin of the sudden shift in the absorption resonance, we determined the field distributions before and after the establishment of the electrical connection. Figure 4.5.a,b show normalized magnetic field profiles in a plane perpendicular to the surface (middle panels) and at the top metal-dielectric interface (lower panels) for the resonance mode of both the disconnected, Figure 4.5.a, and the connected, Figure 4.5.b, cavities, respectively.

In the disconnected nanocavity array mode (Figure 4.5.a) the field profile is solely determined by the properties of each individual cavity. Figure 4.5.a shows the magnetic field profile for the fundamental mode of the cavity with lowest energy resonance. Indeed, in the horizontal plane (top view), the magnetic field exhibits a single peak spreading across the nanocavity with a minimum in between the cavities [47, 37]. For each entity, the observed magnetic field profile represents the standing wave pattern resulting from the constructive interference of the counter-propagating GP modes excited

4. Proximal Gap Plasmon Nanoresonators ...

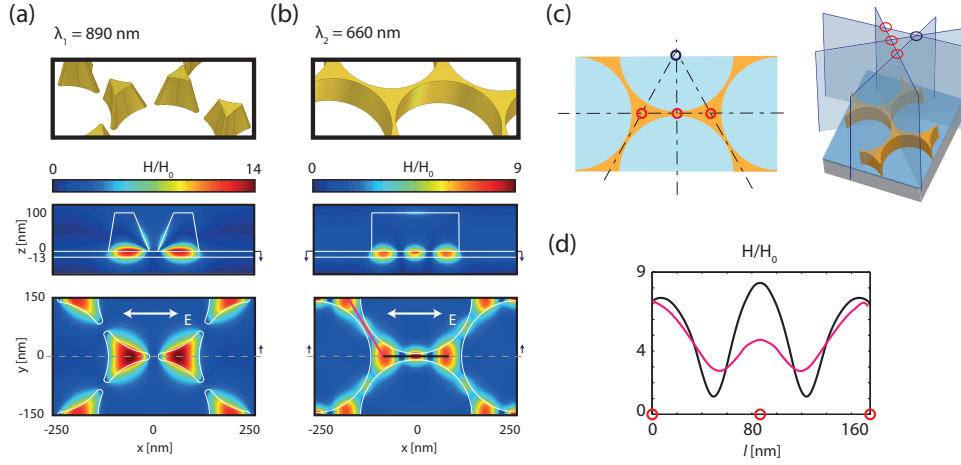


Figure 4.5: Magnetic Field Profiles and Symmetries. (a) and (b) Schematics (upper panels) and normalized magnetic field profiles (middle and lower panels) of the gap plasmon resonances for (a) the disconnected nanocavity array and (b) the connected nanocavity array. The side views (middle panels) are taken on the planes indicated by the dashed lines in the top views (lower panels). The top views are calculated at the upper metal-dielectric interface, as shown by the arrow in the side views. (c) Planes of symmetry for the MIM two-dimensional network (right) and top view of the same schematics (left). The red and blue circles highlight the intersections of the planes of symmetry. The red circles, located along the metal waveguide, identify the positions where symmetry constraints impose a magnetic field peak. The blue circle does not belong to the metal waveguide and is thus irrelevant for the waveguide GP mode. (d) Normalized magnetic field profiles along the two branches of the MIM waveguide in the connected case. The black and pink profiles correspond to the field profiles along the black and pink lines indicated in (b), lower panel, respectively. The red circles indicate the positions of the field extrema and correspond to the red circles in Fig.(c), left.

at the cavity terminations (Fabry-Perot condition) [10]. The field profile of the array of nanocavities, as expected, has a remarkable similarity with that of the isolated nanocavity (see Figure 4.5.a, lower panel and Figure 4.6) At the same time, the waveguide nature of this mode leads to a remarkable vertical confinement (side view) and insensitivity to the excitation conditions [10].

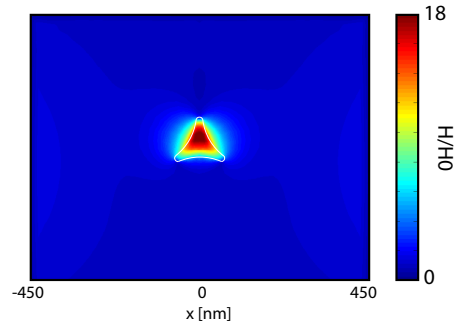


Figure 4.6: Magnetic Field profile of the isolated nanocavity. Normalized magnetic field profile at resonance (≈ 890 nm) for the isolated nanocavity with $h_{SiO_2} = 13$ nm and $d_{TiP} = 24$ nm calculated at the upper metal-dielectric interface

4.4. Results and Discussion

The effect of electrical connections between neighboring nanocavities is apparent in the drastic change of the field profile of the resonance mode (Figure 4.5.b). In fact, the new mode is characterized by an increased horizontal confinement as compared to the disconnected cavity array and additional antinodes are present at the established connection positions (top view). In the following we prove that the field profile shown in Figure 4.5.b represents the fundamental mode of the system with connected cavities.

In the one-dimensional approximation used to describe GP nanocavities, at resonance, the excitation of MIM waveguide modes and their constructive interference constrains the mode to exhibit an odd number of antinodes in the magnetic field profile within the nanocavity [10]. This constraint always leads to an antinode (local maximum with zero derivative) of the magnetic field profile at the symmetry line of the structure. Similarly, in the two-dimensional waveguide network investigated here, as a result of excitation of MIM waveguide modes, the magnetic field profile exhibits a local extremum (zero derivative) at each symmetry plane, in the direction perpendicular to that plane. Therefore, at the points where two anti-parallel symmetry planes intersect, local antinodes (local maxima with zero derivative in two anti-parallel directions) appear (Figure 4.5.c). Four planes of symmetry of the infinite MIM waveguide network under consideration are shown in Figure 4.5.c (right) together with their intersection positions (red and blue circles). The lowest energy resonance mode of the connected structure should then exhibit magnetic field peaks at the locations indicated with red circles and any higher order mode would have a larger number of antinodes. The blue point lies outside the MIM waveguide and therefore, does not experience a field antinode. The pink and black curves in Figure 4.5.d show the magnetic field profiles along the lines indicated in Figure 4.5.b. The red circles correspond to the points where the symmetry planes intersect (also shown in Figure 4.5.c). As seen in this plot, the field profile of the connected structure possesses magnetic antinodes only at the intersection points (Figure 4.5.b). This mode indeed represents the fundamental mode of the structure. One should notice that, although the structure is excited with a pure x-polarized wave, the field profile is determined almost solely by the symmetries of the structure, i.e. it exhibits a magnetic field peak at all junctions and is symmetric not only with respect to the $x = 0$ plane but also, for all practical purposes, upon ± 60 deg rotations (Figure 4.5.b,c). Asymmetries in the field profile, i.e. unequal strength of the antinodes and slight misplacement of the magnetic field peak positions, are a result of the light polarization. We can now attribute the increased horizontal confinement of the mode of the connected nanostructure, as compared to the disconnected nanocavity array, to the emergence of the new antinodes which appear beneath all the

4. Proximal Gap Plasmon Nanoresonators ...

connection points. Indeed, the presence of the additional antinodes leads to shrinkage of each magnetic field antinode extension. This is equivalent to having nanocavities with shorter effective lengths, L_{cav} , as compared to the fundamental mode of the disconnected nanocavity array. According to Fabry-Perot resonance condition, $L_{cav} \cdot \beta = m\pi - \phi$, a decrease in L_{cav} leads to a larger in-plane resonance wavevector, β . Considering the odd MIM dispersion relation of the structure, this increase in β corresponds to a decrease in resonance wavelength (also the discussion regarding table 4.1 and Figure 4.4.g), which explains the abrupt blue-shift of the absorption peak upon connection (Figure 4.2.c). Finally, these considerations are valid for the infinite array condition. In Appendix A we briefly studied the case of connected GP nanocavities with finite number of elements.

In the light of the just discussed aspects, we can now look at the field profiles of the peak indicated with 3 in Figure 4.2.c which was not observed in experiments. Figure 4.7.b presents the normalized magnetic field profiles of this mode.

From the side view (Figure 4.7.b) we notice that the magnetic field is concentrated both in the dielectric spacer and the gap in between the front structures. Similarly, the top view (Figure 4.7.b, bottom) shows that the magnetic field is non-zero between the two tips, in contrast with the standard GP mode profiles (e.g. Figure 4.5.a, lower panel). Overall, we notice a similarity with the channel plasmon polaritons (CPP) supported in grooves with tilted walls [63]. After coupling at the metallic top, such a mode propagates in the negative z-direction along the vertical walls of the front structure creating a magnetic field node between the cavity ends. Moreover, close to the dielectric layer, the CPP mode couples to the GP mode, which then propagates in the gap creating weak magnetic field peaks in the dielectric spacer. This mode has thus a hybrid GP-CPP nature and originates from the side coupling between the structures of the front metallic pattern. This high energy mode is not observed in our experiments due to the non-smooth side walls of our metallic triangles, which do not allow the propagation of the CPP.

If the walls of the structure are considered to be perfectly straight (perpendicular to the substrate), then the absorption spectrum of the system is modified (Figure 4.7.a, green curve). In fact, a very strong absorption peak appears in the visible range, while the fundamental GP mode is dampened and red-shifted. Figure 4.7.c shows the field profiles for the peak indicated with λ_S . We observe that this mode is a pure CPP mode with strong magnetic field confinement along the vertical edges and in between, which also couples very weakly to the GP. Looking at the experimental results (Figure 4.2.b) and at the SEM micrographs (Figure 4.1.b,c) we clearly see that this

4.4. Results and Discussion

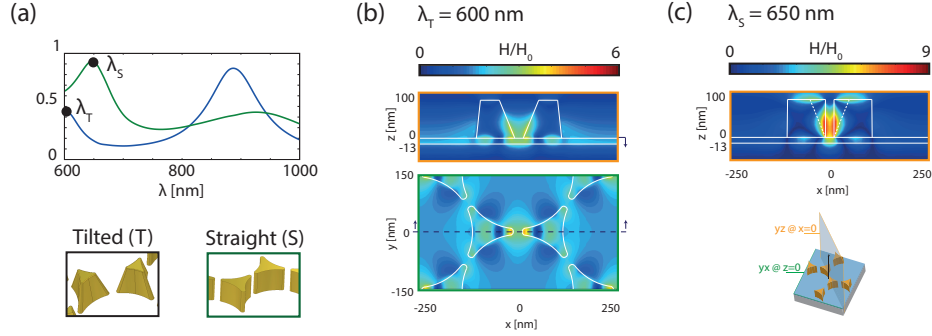


Figure 4.7: Characteristics of the High Energy Mode (3). (a) Absorption spectrum of the realistic geometric with tilted walls (blue curve) and of the idealized geometry with straight vertical sides (green curve). (b) Magnetic field profile in the yz and yx planes at the resonance peak λ_T for the considered realistic geometry. (c) Magnetic field profiles in the yz plane at the resonance peak λ_S of the idealized geometry.

result is not physical and only disturbs the studied phenomenon, which is the evolution of GP nanocavities into a continuous network of MIM waveguides. Numerically we also verified that when the front structure is thin, the coupling to the CPP mode is weak and only pure GP modes become visible in the absorption spectrum [47, 49]. Therefore, the experimental results are better represented by the structure with tilted walls, which have in fact been used throughout this study.

We thus showed that this mode is of substantially different nature than the GP and waveguide modes. Upon connection, due to the disappearance of the vertical channel, this mode becomes completely suppressed. Overall, we conclude that the transition from the disconnected to the connected structure indeed happens abruptly, as the apparent *smooth* transition in reality involves resonances with completely different origins.

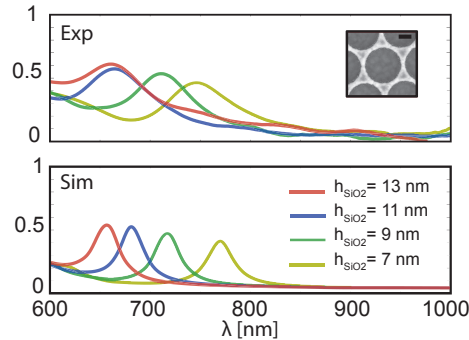


Figure 4.8: Effect of Dielectric Spacer Thickness. Experimental (top) and simulated (bottom) absorption spectra of connected structure arrays with different dielectric spacer thicknesses.

Finally, the preserved waveguide nature of the mode of the connected structure still allows for easy tunability of the resonance position through the dielectric spacer thickness. Figure 4.8 shows the experimental and simulated absorption spectra for different spacer thicknesses, $h_{SiO_2} = 7 - 9 - 11 - 13$ nm. Similarly to Figure 4.4.a,b, the observed red-shift as h_{SiO_2} decreases is a result of a shift in the associated MIM dispersion curve (Figure 4.4.c) [4].

4.5 Conclusions

In summary, we studied, theoretically and experimentally, the interaction between discrete GP nanocavities in an array, near and immediately after the limit at which their top metallic patterns connect. Electrically isolated top patterns result in negligible interaction between GP nanocavities even at distances of approximately 20 nm. However, as soon as the electrical connections are formed, the array transforms abruptly to a continuous network of MIM waveguides, accompanied by the sudden suppression of the original GP absorption resonance and the emergence of a largely blue-shifted new resonance. Furthermore, we showed that the physics responsible for this abrupt change can be explained by the inherent change of the boundary conditions of the system upon connection. In fact the Fabry-Perot interferometer condition, which defines the mode properties in the disconnected nanocavity array, is suddenly replaced by symmetry constraints.

Even though both metasurfaces allow extreme light confinement due to the excitation of GP waveguide modes in the ultrathin spacer [47], both identified regimes have exceptional individual properties, which can be beneficial to different kinds of applications. The negligible interaction between closely-packed nanocavities suggests using such configurations for integrated photonic circuits, where high integration with minimal cross-talk between components is required [64]. On the other hand, resonance tunability, light confinement capabilities and the existence of two electrically continuous electrodes make the demonstrated MIM waveguide network a very attractive candidate for applications such as plasmonic active materials [65, 66] and photocatalysis [17]. Finally, the drastic shift of optical properties of the structure upon contact could be itself employed in the functionality of highly sensitive sensors.

Chapter 5

Three-dimensional Confinement of Light in Deeply Subwavelength Gap-plasmon Nanocavities

5.1 Abstract

Combining extreme coupling in ultrathin metal-insulator-metal (MIM) structures with the light concentration capabilities of a planar tapered strip, we propose an array of graded planar gap plasmon (GP) nanocavities to efficiently confine light at deeply subwavelength dimensions. A semi-analytical one-dimensional model allows us to understand the underlying physics and approximately predict the behavior of the structure. Three dimensional simulations are then used to precisely calculate the optical behaviors of the structure. We show that laterally thinning the graded structure substantially increases the effective refractive index of the excited mode. This leads to a simultaneous bi-dimensional shrinkage of the mode. Moreover, we show how the superposition of symmetry constraints on such a graded waveguide leads to the formation of a deeply sub-wavelength nanocavity where light is effectively confined. Mode shrinkages greater than 20 times as compared to conventional gap plasmons are achieved within volumes as small as 6000 nm^3 . Being composed of a holey gold layer and a continuous silver film separated by an ultrathin glass spacer, our design could find interesting applications in the area of active metamaterials or plasmonic photocatalysis where both electrical access and light concentration are stringent requirements.

5.2 Introduction

Plasmonic structures have become essential in bridging the gap between the micro-scale of visible-IR light waves and the nanoscale of electronic devices or quantum emitters [67]. Accordingly, an increasing number of designs have been proposed to confine, guide, manipulate and focus light at the nanoscale, relying both on localized [68] and propagating surface plasmons [69].

Coupled metallic surfaces have been shown to be more effective than single metal-dielectric interfaces in achieving subwavelength light confinement [4]. In particular, metal-insulator-metal structures (MIM) support an asymmetric (odd) surface plasmon polaritons (SPP) which does not exhibit any cut off thickness. This mode is mainly confined in the dielectric gap (thus called gap plasmon, GP) and is thus well suited for confining light in a desired non-metallic material (e.g. photo-catalyst or active material). Given the direct proportionality between the GP mode group velocity and the gap thickness [4], most designs have employed MIM waveguides with tapered dielectrics to successfully slow down and nano-focus the light [70], [6], [8], [71]. However, realizing tapered three dimensional structures requires cumbersome fabrication procedures [8]. For applications requiring extreme light confinement [47] GP nanocavities can be used. Indeed, film-coupled nanoantennas form truncated MIM waveguides supporting GP modes [10]. These GPs are continuously reflected at the terminations of the nanoresonator forming a standing wave pattern inside each MIM nanocavity. Contrary to waveguides, such finite systems can directly couple the incoming radiation to the deeply subwavelength dielectric gap [47] and can be fabricated also with simple colloidal techniques [10]. However, the coupling efficiency drops for very small antennas.

In this chapter we first show how a planar, tapered GP waveguide can be used to achieve full three dimensional light focusing. Successively, we demonstrate a symmetric and periodic planar design where this concept is used to create deeply subwavelength nanocavities where light can be confined with better coupling efficiency than in the case of film-coupled nanoantennas. Indeed, using three dimensional simulations and a semi-analytical one-dimensional model we show that, while propagating along the waveguide, the excited GP mode is focused due to a significant increase in the nanocavity effective refractive index with shrinking width. Thus, the studied structure simultaneously exploits the extreme coupling properties of gap-plasmons in ultrathin systems and the nanofocusing capabilities of laterally tapered strips to achieve deeply subwavelength light confinement. Being based on a metal hole array coupled to a continuous back reflector through an ultrathin dielectric spacer, our design could find potential applications in the emerging

fields of active metamaterials[65] and plasmonic photocatalysis where both electric access and fast heat removal would be advantageous [72], [17]. More broadly, our approach could be used to design and easily fabricate planar elements for light guiding and focusing at the nanoscale.

5.3 Methods

5.3.1 Numerical Modeling

All the simulations were performed using the COMSOL Multiphysics package (RF module), which is based on the finite element method (FEM). In all simulations we assumed planar normal illumination. The dielectric properties of the metals were taken from the literature [36, 60] while the refractive index of glass was set equal to 1.5.

Array Simulations

For the array of GP nanocavities we used symmetry boundary conditions to reduce the computational domain to one-fourth of a unit-cell. We used a port boundary condition to excite the system with normal illumination and we solved for the total fields.

N_{eff} Calculation

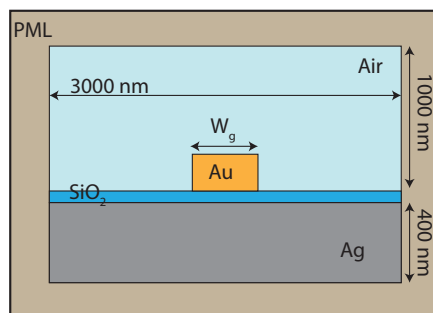


Figure 5.1: N_{eff} Calculation Bi-dimensional computational domain defined for the calculation of N_{eff} .

To compute the propagating GP modes of waveguides with finite width, we set-up a bidimensional model in COMSOL, which is represented in Figure 5.1. The dimensions of the overall cell were chosen large enough to avoid the calculation of spurious eigenmode of the entire space. As we were interested

5. Three-dimensional Confinement of Light ...

only in the modes of the gap, the silver layer was assumed infinite while all of the other dimension concerning the waveguide were equal to the case under study ($h_{SiO_2} = 13$ nm, $h_{Au} = 100$ nm).

The Mode analysis node was used to solve for the structure eigenmodes. Among all the computed modes, we manually selected the odd GP mode by looking at the field profiles (as shown in Figure 5.2). The obtained values are complex numbers, the real part representing the propagation wavevector and the imaginary part accounting for the losses. For most of the computed values, losses were less than 7%, rising above 10% for very narrow waveguides and short wavelengths.

5.4 Results and Discussion

Even though most MIM GP-based designs rely on the extremely large mode wave-vectors obtained for very thin dielectric spacers [4], [6], [47], it is known that lateral confinement can be also responsible for an increased mode effective index [6], [73] and eventually, in the limit of very narrow waveguides, the mode has a localized surface plasmon character [51]. Nevertheless, only few works [8], [74] in the literature have exploited this alternative nanofocusing effect. We used the Mode Analysis solver in COMSOL to compute the modes of a MIM system consisting of an infinitely thick silver (Ag) continuous metallic layer, an ultrathin ($h_{SiO_2} = 13$ nm) glass (SiO_2) layer and a 100 nm thick gold (Au) stripe of width W_g (Figure 5.2.a). From the magnetic and

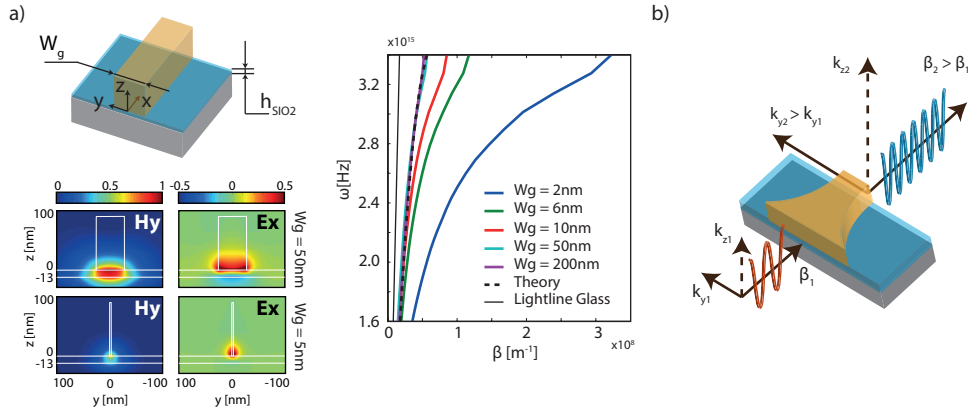


Figure 5.2: Effect of Width (W_g) in a GP-based Waveguide. a) left - Schematic of the simulated MIM waveguide and coordinate system; odd GP mode in-plane (y - z) magnetic field profiles (left column) and out of plane electric field profiles (right column) calculated for a MIM waveguide with finite width W_g using the Mode Analysis solver in COMSOL; right - dispersion curves for MIM waveguides with different finite widths W_g . b) Schematic representation of the three-dimensional concentration effect caused by lateral confinement of the GP mode in a tapered planar waveguide.

5.4. Results and Discussion

electric field profiles (Figure 5.2.a) we identified the asymmetric GP mode and recorded the calculated out-of-plane mode wave-vector $\beta(\lambda, W_g)$ thus obtaining the dispersion curves reported in Figure 5.2.a. We observe that a reduction of W_g modifies the dispersion curve of the described waveguide in a manner similar to a reduction of the dielectric spacer thickness [65]. Indeed, at a given frequency, the narrower the waveguide the larger the propagation wavevector β (change of the dispersion curve). We also notice that, for a fixed frequency, the slope of the dispersion curve, $\partial\omega/\partial\beta$, representing the group velocity, decreases for decreasing waveguide width. For W_g values comparable or smaller than h_{SiO_2} , this effect becomes dramatic. On the other hand, we see that for W_g larger than 50 nm, the lateral confinement plays a negligible role, confirming the validity of the infinite strip approximation for the majority of the works available in the literature where the used dimensions and wavelengths are in the region of insensitivity to lateral confinement [47],[10].

Figure 5.2.b shows the schematics of a bi-dimensional, tapered ultra-thin MIM waveguide capable of three dimensional light focusing. As demonstrated, the lateral tapering is responsible for the increase of the propagation wavevector, β , and the reduction of the mode group velocity. Concurrently, the transversal wavevector, k_y , which is real in the dielectric due to the absence of interfaces, can be assumed to be inversely proportional to W_g and will therefore increase along the tapered waveguide. This effect is clearly visible in Figure 5.2.a where the extension of the field profiles along y decreases with W_g . Due to momentum conservation:

$$k_0\epsilon = 2\pi/\lambda = \sqrt{\beta^2 + k_y^2 + (ik_z)^2} = \sqrt{\beta^2 + k_y^2 - k_z^2} \quad (5.1)$$

the purely imaginary wavevector in z-direction, k_z , is thus forced to grow in magnitude, leading to a stronger localization of the mode in the vertical direction and a three dimensional focusing of the mode.

From the dispersion curves we can determine the mode effective refractive index as:

$$N_{eff}(\lambda, W_g) = \beta(\lambda, W_g)/k_0 \quad (5.2)$$

where $k_0 = 2\pi/\lambda$ is the illuminating light wavenumber (Figure 5.3.a). As anticipated in Figure 5.2.a, for W_g smaller than 10 nm and for wavelengths shorter than 800 nm $N_{eff}(\lambda, W_g)$ increases significantly. Knowing the waveguide profile, $W(x)$, as well as $N_{eff}(\lambda, W_g)$, it is then possible to calculate the effective refractive index profile of an arbitrary waveguide at any given wavelength, $N_{eff}(\lambda, x)$.

5. Three-dimensional Confinement of Light ...

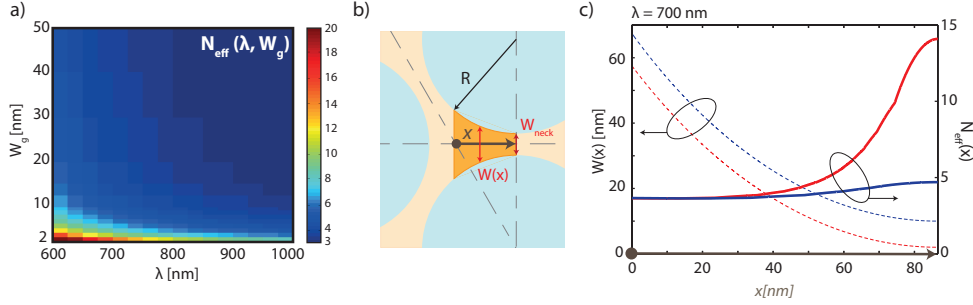


Figure 5.3: Effective Refractive Index Calculation a) GP mode effective refractive index (real part) as a function of W_g and λ ; b) Au front strip profile corresponding to an hexagonal arrangement of holes with center-to-center distance equal to 300 nm and radius of curvature R . The bright orange part identifies the considered waveguide section. The used coordinate system (x) is defined together with the minimum width point, W_{neck} ; c) waveguide width profile $W(x)$ (dashed lines) for W_{neck} equal to 10 nm (blue curve) and 2 nm (red curve) and corresponding N_{eff} profiles (continuous lines) calculated combining $W(x)$ with the information of part a).

We considered a tapered waveguide section whose front Au strip has the profile shown in Figure 5.3.b (bright orange area). Indeed, the complete periodic structure (pale orange area) was shown to exhibit interesting absorption and confinement properties 4. According to expectations, when the minimum waveguide width is of the order of 10 nm, the refractive index profile is nearly constant (Figure 5.3.c, blue curves). Instead, when the waveguide width drops below 10 nm, $N_{eff}(x)$ increases dramatically (Figure 5.3.c, red curves) corresponding to a significant focusing of the mode along the direction of propagation, x (see also Figure 5.2.a).

Contrary to a waveguide which presents a continuum of allowed modes, a symmetric and periodic pattern is characterized by resonance mode(s) because of the additional constraints imposed by symmetry and periodicity. More specifically, the allowed GP modes are characterized by a phase accu-

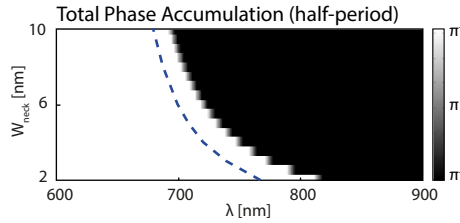


Figure 5.4: Total Phase Accumulation (half-period) of the GP mode for a Periodic and Symmetric GP Metasurface Calculation of the total phase accumulation along half-period of the structure shown in Figure 5.3.b and Figure 5.5.a for different width profiles and different wavelengths. For each waveguide there is only one wavelength which leads to a total phase accumulation equal to π , which is then the fundamental mode resonance frequency. The dotted line report the resonance wavelength as calculated with 3D simulations (see Figure 5.5.a).

5.4. Results and Discussion

mulation of 2π over a complete period of the structure and of π over half a period because of symmetry:

$$\int_0^{L/2} \beta(x) dx = m\pi \quad (5.3)$$

where L correspond to the spatial length of a period. The knowledge of $N_{eff}(\lambda, x)$ (Figure 5.3) thus allows us to predict the resonance wavelength for a periodic and symmetric MIM structure by calculating:

$$\int_0^{L/2} \beta(x) dx = \frac{2\pi}{\lambda^*} \int_0^{L/2} N_{eff}(\lambda^*, x) dx \quad (5.4)$$

Figure 5.4 shows such integration performed for the considered periodic and symmetric structure (Figure 5.3.b and Figure 5.5.a) as a function of wavelength and W_{neck} . The expected resonance wavelength is then given by:

$$\frac{2\pi}{\lambda_{res}} \int_0^{X_{neck}} N_{eff}(\lambda_{res}, x) dx = m\pi \quad (5.5)$$

and the extreme color-scale evidences the curve corresponding to $\lambda_{res}(W_{neck})$. We observe that W_{neck} has a considerable influence on the optical properties of the metasurface, the excited GP mode (λ_{res}) substantially red-shifting as W_{neck} decreases below 10 nm. Indeed, as the minimum width of the waveguide is decreased $N_{eff}(x)$ presents a steeper gradient (Figure 5.3.b) and the overall optical size of the considered structure increases. This result is in good agreement with the absorption resonance position obtained from 3D simulations (Figure 5.4 dashed line and Figure 5.5.a). The nearly constant offset could be attributed to polarization effects or to reflections of the excited mode along the structure which are not considered in the approximated calculations. Nevertheless, the similarity of the observed trends confirms the validity of the tapered waveguide approach to describe the behavior of the periodic GP metasurface.

In a periodic, tapered structure, the significant increase in $\beta(x)$ and decrease in group velocity upon reduction of $W(x)$ are also beneficial for the absorption process as they reduce the possibility of out-coupling of the GP mode due to time-reversal effects. In fact, after in-coupling the GP mode propagates along the waveguide eventually reaching the corresponding point in the next unit cell of the array where, due to reciprocity, it can be efficiently out-coupled. However, slower GP waves and larger optical distances reduce the chances of propagating along a full period of the array. Indeed, from Figure 5.5.a we observe that, the smaller W_{neck} , the stronger the absorption peak.

5. Three-dimensional Confinement of Light ...

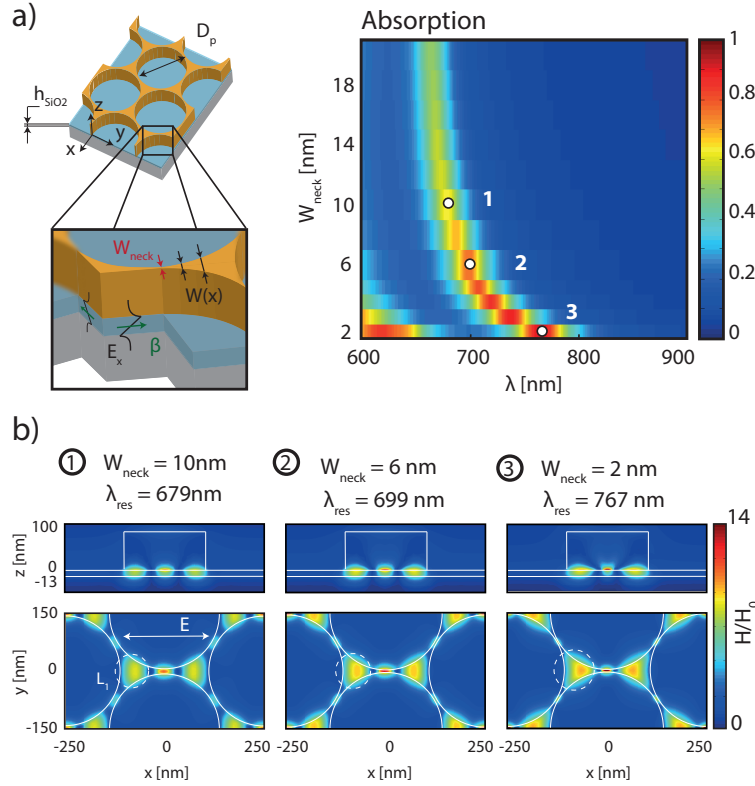


Figure 5.5: Periodic and Symmetry GP Metasurface with Tapered Geometry. a) left - sketch of the overall geometry and definition of the geometrical parameters of the tapered structure, D_p , $W(x)$ and W_{neck} . Right - evolution of the absorption spectrum of the considered structure upon reduction of W_{neck} ; c) From top to bottom: normalized magnetic field profiles for the resonance modes indicated with 1,2,3 in part a) (side views correspond to the xz plane for $y = 0$, top views correspond to the xy plane for $z = 0$); the dotted circles identify the single-node cavity effective size, L_1 , as defined in the text.

Given the marked magnetic character of GP resonances, magnetic field profiles can reveal important details of the excited modes. Figure 5.5.b shows these profiles for the resonances indicated with 1,2 and 3 in Figure 5.5.a, corresponding to W_{neck} equal to 10 nm, 6 nm and 2 nm respectively. Both the side views (upper panels) and the front views (lower panels) display a high degree of confinement of the GP mode: vertically the field is trapped in the dielectric spacer and horizontally it is tightly bounded beneath the holey metal pattern. In all the considered cases the field exhibits a standing wave pattern (see Chapter 4) which creates several optical nanocavities (field antinodes) with non-homogeneous spatial distribution. From the front views we observe that a broad field antinode is present below the large section of the waveguide while a tighter antinode is present under the neck, its extension in x - and y -directions decreasing upon reduction of W_{neck} . From the side views we also notice that, the decrease of the in-plane (x - y) extension of this antin-

5.4. Results and Discussion

ode is accompanied by a higher degree of localization of the magnetic field close to the upper dielectric-metal interface. Indeed, this trend is consistent with the approach described in Figure 5.2.b.

In a GP nanocavity with uniform cross section and effective refractive index, the resonance condition can be obtained from the Fabry-Perot condition [9]:

$$L_{cav} \cdot \beta = m\pi - \phi \quad (5.6)$$

Assuming $\phi = 0$ and $m = 1$, it is possible to identify an elemental field antinode whose effective optical size, L_1 , is equal to:

$$L_1 = L_{cav}(m = 1) = \pi\beta \quad (5.7)$$

where β is the GP wavevector calculated from the gap-plasmon dispersion curve knowing the vacuum resonance wavelength $\lambda_{res}(\beta_{MIM}(h_{SiO_2}, \lambda_{res}))$. The overall optical size of the cavity is then equal to $m \cdot L_1$.

Similarly to the case of film-coupled nanoantennas, the observed mode of our periodic metasurface (Figure 5.5.b) can be assumed to originate from the constructive interference of two counter-propagating GP waves. Using the result of Figure 5.2.a, $\beta_{MIM}(13nm, \lambda(W_{neck}))$, and Figure 5.5.a, λ_{res} , we

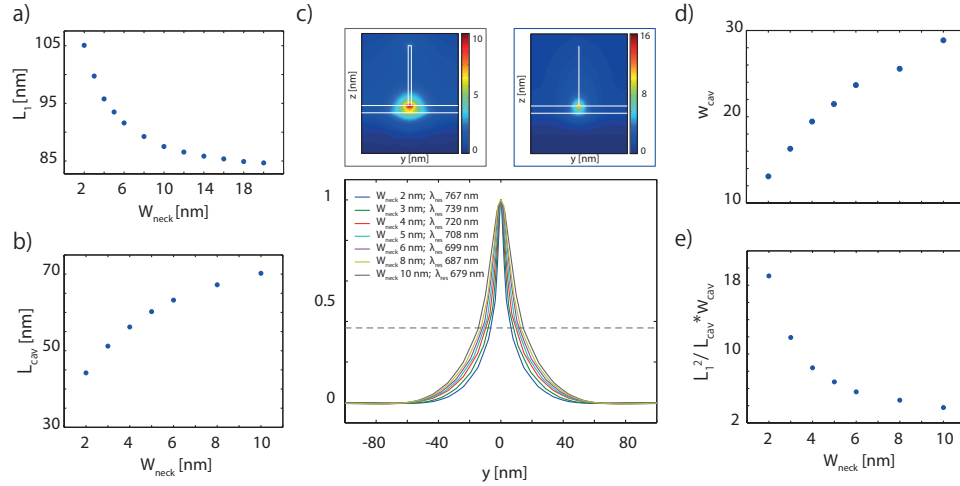


Figure 5.6: Results of Nano-confinement. a) Calculation of L_1 at the resonance wavelength (see Figure 5.5.a) for structures with different W_{neck} values; b) Physical extension of the nanocavity underneath the neck as a function of W_{neck} ; c) Magnitude of magnetic field at resonance at the neck position in a plane perpendicular to the mode propagation direction (z - y plane) for W_{neck} equal to 10 nm (upper left panel) and 2 nm (upper right panel). Comparison of the mode extension in the y - z plane and at $z = 0$ for different waveguides at resonance. Due to the physical lateral confinement the mode is focused also in the y direction. The dashed line indicates the $1/e$ point that we use to quantify the mode extension. d) Quantification of the mode extension in the y direction. w_{cav} is computed from part c). e) For the nanocavity at the neck we compare its optical area, proportional to L_1^2 , to the physical extension, proportional to $L_{cav} \cdot w_{cav}$. The confinement in the lateral direction boosts this ratio to nearly 20 times.

5. Three-dimensional Confinement of Light ...

thus computed L_1 as a function of W_{neck} (Figure 5.6.a). In Figure 5.5.b we indicate with a dashed circle an equivalent circular cavity, $D_{cav} = L_1$ centered at one of the intersections of the axis of symmetry of the structure (see Chapter 4) and observe that the calculated L_1 correctly predicts the extension of the broad nanocavities, whose effective refractive index is nearly constant. Instead, the nanocavity below the neck has a much smaller in-plane (x-y) extension as a consequence of its large effective refractive index.

We quantified the achieved planar confinement by comparing the optical and physical size of this nanocavity. We define the cavity dimension along x (L_{cav}) measuring the distance between the zeros of the magnetic field (Figure 5.6.b). The cavity dimension along y (w_{cav}) is instead obtained by extracting the magnetic field profile along y at the upper metal-dielectric interface and by measuring the distance between the positions at which the field intensity drops below $1/e \cdot H_{peak} \approx 0.368H_{peak}$ (Figure 5.6.c). As W_{neck} decreases, both L_{cav} and w_{cav} reduce non-linearly (Figure 5.6.b,d) and, approximating the cavity physical area with an ellipse, the area ratio:

$$\frac{A_1}{A_{cav}} = \frac{L_1^2}{L_{cav} \cdot w_{cav}} \quad (5.8)$$

increases in a hyperbolic manner for $W_{neck} \rightarrow 0$ (Figure 5.6.e). For $W_{neck} = 2$ nm the cavity has a physical extension which is nearly 20 times smaller than its optical area. Therefore, by employing a periodic and symmetric MIM structure with tapered geometry it was possible to confine light in a deeply subwavelength nanocavity. Such degree of confinement is relative to a dielectric spacer of 13 nm and better results could be obtained further reducing this dimension to few nanometers [47].

Even though the proposed metasurface could be fabricated with simpler techniques than previously described 3D structures [8], it remains considerably more complex than the colloidal approach used for film-coupled nanoantennas [10]. However, it presents significant advantages in the case of visible-light concentration in deeply subwavelength nanocavities. We define the average energy density, E_{ave} , by dividing the total energy stored in the nanocavity (in the dielectric) by the nanocavity volume and, as shown in Figure 5.7.a, we compare E_{ave} in the nanocavity under the neck with E_{ave} in a nanocavity with the same physical dimensions and shape but formed by a film-coupled nanoantenna. We observe (Figure 5.7.b) that, while the latter system presents an optimal cavity size ($6 \text{ nm} \leq W_{neck} \leq 15 \text{ nm}$, blue circles), the proposed approach is characterized by a monotonic increase of E_{ave} upon reduction of the nanocavity dimension (green squares) and for W_{neck} smaller than 4 nm it is more effective than the equivalent film-coupled nanoantenna system in concentrating the energy in the dielectric.

5.5. Conclusions

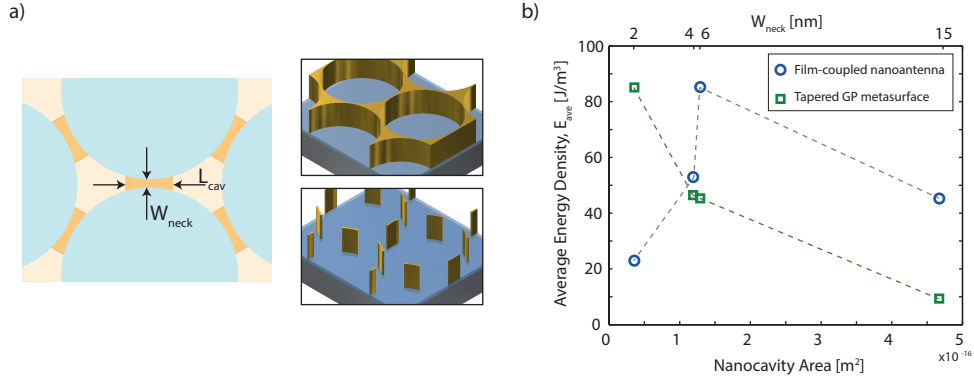


Figure 5.7: Energy Confinement. a) Definition of the nanocavity volume as $V_{cav} = \text{bright} - \text{orange} - \text{area} \cdot h_{SiO_2}$. The right insets show one of the proposed GP metasurfaces (top) and its equivalent film-coupled nanoantenna array (bottom). Indeed, as shown in the left schematics, the latter has the same nanoantenna dimensions of the nanocavity formed under the neck; b) Average energy density E_{ave} stored in the nanocavity under the neck (green squares) and in the equivalent nanocavity under the film-coupled nanoantenna (blue circles) at resonance as a function of the nanocavity area (bright orange area in part a)). The dashed lines have only eye-guiding purpose.

5.5 Conclusions

In conclusion, combining the extreme coupling in ultrathin MIM structures [47] with the concentration effect of laterally tapered strips (both along the direction of propagation and perpendicular to it) and including the symmetry constraints, we achieved deeply subwavelength, three dimensional light nano-confinement in a planar geometry. Due to the GP nature of the excited modes, the incoming light can be directly coupled into the ultrathin dielectric spacer and we showed that the coupling frequency strongly depends on the width profile of the structure. We also demonstrated that the proposed approach is more advantageous as the required confinement dimensions decrease. In addition, the proposed structure is capable of nano-confining light in a very small volume in the dielectric spacer between two continuous metal layers. Therefore substituting the used glass layer with a gain material or a catalyst would provide an interesting, electrically accessible system where incoming radiation is strongly concentrated in the active material [65], [17]. At the same time, the high thermal conductivity of the metals and the low thermal capacity of the entire structure provide interesting thermal characteristics for thermally demanding applications (e.g. steady state lasers [65]). More generally, planar tapered ultrathin waveguides can represent a useful paradigm to design and easily fabricate planar highly integrated optical components for light guiding and focusing at the nanoscale, avoiding the often cumbersome fabrication procedures required to achieve more commonly proposed three dimensional designs [8], [71].

Chapter 6

Macro-Scale Thermal Response of a Broadband Plasmonic Absorber

Part of this Chapter has been submitted for publication.

6.1 Abstract

Plasmonic nanostructures can significantly advance broadband visible-light absorption, with absorber thicknesses in the sub-wavelength regime, much thinner than conventional broadband coatings. Such absorbers have inherently very small heat capacity, hence a very rapid response time, and high light power-to-temperature sensitivity. Additionally, their surface emissivity can be spectrally tuned to suppress infrared thermal radiation, yielding efficient selective coating performance. These capabilities make plasmonic absorbers promising candidates for fast, high-temperature light-to-heat applications, such as radiation sensors or thermal-photovoltaics. Here we investigate the light-to-heat conversion properties of a metal-insulator-metal broadband plasmonic absorber, fabricated as a free-standing membrane. Using a fast IR camera, we show that, due to its sub-wavelength thickness, the transient response of the absorber has a characteristic time below 13 ms, nearly one order of magnitude lower than a similar membrane coated with a commercial black spray. Concurrently, despite the small thickness, due to the large absorption capability, the achieved absorbed light power-to-temperature sensitivity is maintained at the level of a standard black spray. Finally, we show that while black spray has emissivity similar to a black body, the plasmonic absorber features a very low infra-red emissivity of almost 0.16, demonstrating

its capability as selective coating for high temperature applications.

6.2 Introduction

Initially considered an undesired effect limiting the design of plasmonic based circuits, absorption in plasmonic structures has gained more attention in recent years due to the emergence of new areas of application. On the one hand, those requiring engineering of nanoscale heat sources such as cancer targeting or optofluidics [75], [44]. On the other hand, macro scale applications requiring broadband efficient absorbers such as sunlight vapor generators [76], [77], solar thermoelectric [21], [16], thermal photovoltaic [15] as well as radiation sensors [78].

Absorption is intrinsically related to plasmons excitation. Nevertheless, the design of efficient narrowband as well as broadband absorbers requires carefully dimensioned multilayer systems. For example, the exploitation of strong magnetic resonances in film-coupled plasmonic nanoantennas [37], [10] leads to enhanced absorption properties compared to the original nanoantennas system. However, theoretical and experimental studies on the light-to-heat conversion capabilities of plasmonic systems have focused so far on the individual and collective response of separated plasmonic nanoantennas supported by (when not embedded in [79], [80]) a bulk dielectric material [81], [82]. Though improving the fundamental understanding of plasmonic heating processes at the nanoscale, only few studies [75], [80] considered the thermal behavior of large scale plasmonic systems which are instead necessary for many applications. Moreover, to the best of our knowledge, no work investigated the thermal response of an optimally designed plasmonic absorber.

In this chapter, we study the macroscopic thermal response of the broadband, large scale, multilayer plasmonic absorber presented in Chapter 3 which we were able to fabricate as a free-standing ultrathin membrane with a diameter of 10 mm. After characterizing its optical absorption properties, we performed IR measurements to determine its temperature rising capabilities in terms of peak temperature and characteristic rising time. Thanks to the subwavelength thickness and the negligible thermal capacity such broadband plasmonic absorber has a time constant of less than 13 ms and a sensitivity above $2.4 \cdot 10^3$ K/W. Comparing these results with a commercial blackening spray, we show that our plasmonic design has one order of magnitude faster thermal response while exhibiting comparable peak temperatures. To conclude, we present preliminary results of the implementation of the proposed absorber on a real thermoelectric sensor.

6.3 Methods

6.3.1 Sample Fabrication

The schematic representation of the studied broadband plasmonic absorber membrane is given in Figure 6.1.a. It consists of a metal-insulator metal (MIM) multilayer structure presenting a continuous gold back reflector ($h_{AuBR} = 100$ nm), a continuous SiO_2 dielectric layer ($h_{SiO_2} = 60$ nm) and a patterned gold front layer ($h_{AuFP} = 100$ nm).

As rigid supports for the absorber fabrication procedure we used 18x18

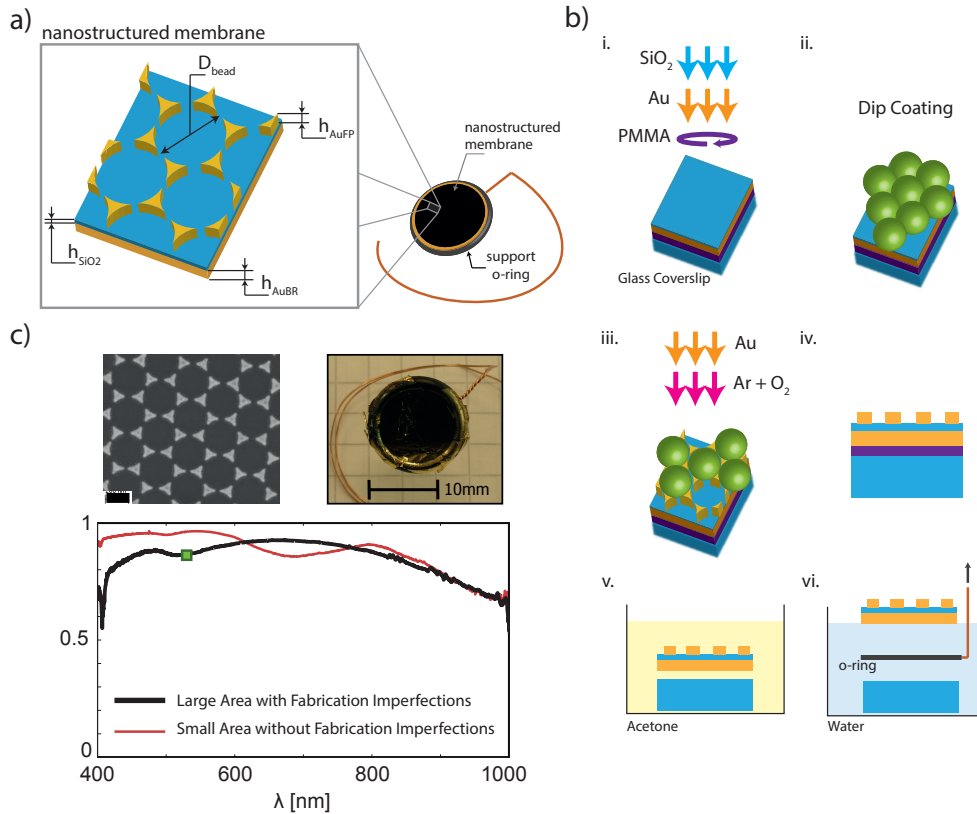


Figure 6.1: Broadband Plasmonic Absorber Design and Fabrication. a) Schematic representation of the broadband plasmonic absorber. The absorber consists of a nanostructured membrane suspended onto a thermally isolating o-ring (right). The geometrical details of the multilayer plasmonic absorber membrane are shown on the left; b) Schematic representation of the fabrication process for a large-scale, suspended, ultra-thin nanostructured membrane; c) upper panel: scanning electron micrograph from the top surface of a fabricated absorber (left, scale-bar 200 nm) and an image from an absorbing membrane suspended on an o-ring (right). Lower panel: absorption spectrum of the broadband plasmonic absorber. Red curve: absorption spectrum measured from a micrometer-scale area free of fabrication imperfections; black curve: absorption spectrum measured from a large, nanostructured area which includes standard fabrication imperfections; the green square represents the absorption at the used excitation laser wavelength.

mm glass coverslips. On the glass chip we first of all spin coated a thin layer of PMMA (240 μl of 9%wt PMMA in toluene spin coated for 30 s at 650 rpm) that we later used as sacrificial layer. We then proceeded with the standard absorber fabrication procedure which consists of the e-beam evaporation of a 100 nm gold layer and a 60 nm SiO₂ layer, the formation of a self-assembled polystyrene beads (300 nm in diameter) monolayer with dip coating, an etching step to adjust the size of the beads mask and the final e-beam evaporation of the 100 nm thick front gold pattern (Figure 6.1.b.i-iii).

After removal of the beads with a gentle water jet, we placed the sample in pure acetone for at least 24 h to allow for the complete dissolution of the thin, uncured PMMA layer. For the final lift off of the plasmonic membrane we firstly removed the acetone and then gently added water in the same beaker. The freed plasmonic absorber membrane can then be lifted and obtained floating at the water surface. Finally, we used a rubber o-ring (12 mm inner diameter, 2 mm rubber diameter) to suspend the membrane for further handling. As our experimental set-up is mostly made of metallic components, the rubber o-ring later ensures the thermal isolation of our sample from the environment. Upon removal from the water surface, surface tension helps in straightening the absorber membrane (Figure 6.1.b.iv-vi).

6.3.2 Infrared Thermography Measurements

Figure 6.2 shows the experimental set-up. The sample is mounted on a flat support with the absorber side facing downwards and the back gold layer facing upwards. Illumination comes from below and hits the absorber side while the IR camera (FLIR, SC7650) is placed vertically above the sample looking at the gold back layer. Even though IR measurements are difficult to perform on low emissivity materials such as metals, being non-contact they were the only choice for the characterization of the thermal response of our ultrathin absorber. In fact, any contact probe (e.g. thermocouples or RTDs micro-fabricated on the same membrane) would have significantly affected the system (see Figure 6.9). For the same reason, we could not apply any blackening material at the back of the absorber to improve the accuracy of the measurements (see Figure 6.8).

In order to compensate for the very low signal from the sample (very low emissivity) we needed a high power light source and we opted for a continuous wave green (532 nm) laser. Using a series of neutral density filters we could change the power incident on the sample, P_{in} , from 4.8 mW to 60.3 mW. The laser was continuously running and we controlled the sample irradiation via an in-house made shutter consisting of a metallic disk with a 45° opening. During the irradiation time the beam was located at the center of the 45°

6.3. Methods

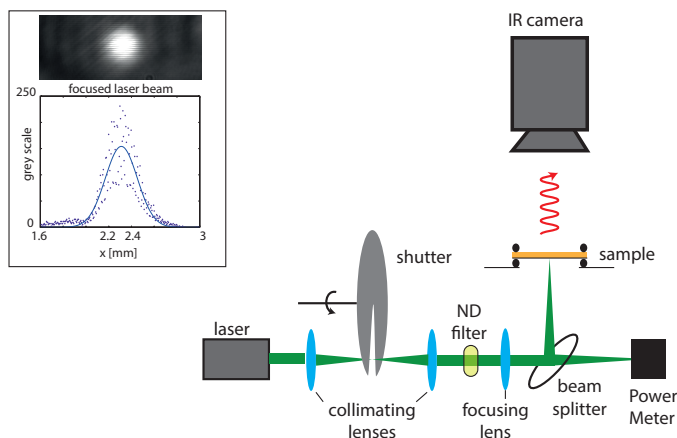


Figure 6.2: Schematics of the measurement set-up. The upper left inset shows the focused laser beam at the sample position.

open sector of the shutter. Approximately every 3 s the shutter was then rotated by 180° deg, alternatively blocking or enabling illumination of the sample.

We placed the shutter at the focal position of the first collimating lens in order to minimize the beam opening and closing times. The laser beam has a nominal diameter of 1.2 mm which we focus with a 5 cm lens to a theoretical spot diameter of approximately 50 μm ($d_{focus} = 2f\lambda/D_{beam}$). Considering a very safe size of the focal spot of 500 μm (which accounts for the small beam divergence and eventual shutter misalignment with the respect to the beam waist) and knowing the shutter radius (4 cm) and its rotation speed (approx 160 rpm, full speed, motor mechanical time constant ≈ 5 ms) we obtain a beam opening time of the order of 1 ms. We periodically excited the samples with pulses of light with long enough width to ensure reaching the steady state.

All the measured sequences were recorded with an acquisition frequency of 500 Hz. Higher frequencies were achievable with the IR camera but loss of data happened during transfer to the computer hard disk (Ethernet cable). The exposure time was chosen equal to 410 μs , which gives a calibrated measurable black-body temperature range of 21°C - 92°C. As we will see in the following, for the highest powers we had to extrapolate the manufacturer calibration curve up to 83% (calculated single pixel peak temperatures of 168°C). Nevertheless, as stated by the manufacturer [83], extrapolation is allowed as the used calibration curve is based on radiation physics and is a theoretical procedure only limited by electronic related constraints [83]. The good agreement of the results with the data within the calibration range (approximately $P_{in} < 40$ mW, $P_{abs} < 35$ mW) supports the validity of our

6. Macro-Scale Thermal Response ...

extrapolation.

Let's now come to the temperature values calculation starting from the sequences acquired with the IR camera. The IR camera collects thermally radiated energy in a defined wavelength range which consists of three contributions: the emission from the object of interest, the reflected emission from ambient sources and the atmosphere emission. Mathematically we write:

$$W_{tot}(x, y, t) = \epsilon\tau_{air}W_{obj}(x, y, t) + (1-\epsilon)\tau_{air}W_{amb}(x, y, t) + (1-\tau_{air})W_{atm} \quad (6.1)$$

where ϵ is the studied object emissivity and τ_{air} is the transmittance of the atmosphere. Given the close distance between the IR camera and our sample we can assume $\tau_{air} = 1$ and neglect the last term. Nevertheless, in order to convert the measured signal $W_{tot}(x, y, t)$ to the desired temperature value $T_{obj}(x, y, t)$ we then need to know the object emissivity ϵ , the local ambient reflection $(1 - \epsilon)W_{amb}$ and the camera calibration curve which is given by the manufacturer

$$f_{cal} : W[DL] = f_{cal}(T[K]) \quad (6.2)$$

where DL are the camera units (digital level).



Figure 6.3: Emissivity calculation. Left) Picture of the used metallic cylinder with a deep hole which acts as a black body cavity and the surface coated with gold to obtain similar emission properties to our sample. right) Emissivity map calculated with the camera software.

We estimated the sample emissivity ϵ using a black body cavity (hole with diameter-to-depth ratio higher than 10 [84]) in a metallic cylinder whose front surface has similar radiative characteristics to our absorber. The cylinder was electrically heated to 40°C and then 60°C. As the cavity has unit emissivity and the cylinder has uniform temperature (Biot number smaller than 0.1), we can derive the emissivity of the surface of interests (Figure 6.3) which is $\epsilon = 0.1 \pm 0.01$.

From equation 6.1 we see that, when ϵ is low (like in our case), the reflection term $(1 - \epsilon)W_{amb}$ can become dominant. We will now show how the reflection contribution can be removed during the data-processing but in order to obtain consistent result it is very important to shield the set-up during the measurement in order to avoid temporal fluctuations of this term.

6.3. Methods

We begin with the removal of the spatially varying but timely constant contribution of the reflections from the environment $(1 - \epsilon)W_{amb}(x, y)$ by subtraction of the first frame from the entire acquired sequence. The frames at time zero (first frame) and t are:

$$\begin{aligned} W_{tot}(x, y, 0) &= \epsilon W_{obj}(x, y, 0) + (1 - \epsilon)W_{amb}(x, y, 0) \\ W_{tot}(x, y, t) &= \epsilon W_{obj}(x, y, t) + (1 - \epsilon)W_{amb}(x, y, 0) \end{aligned} \quad (6.3)$$

and their subtraction gives:

$$W_{tot}(x, y, t) - W_{tot}(x, y, 0) = \epsilon(W_{obj}(x, y, t) - W_{obj}(x, y, 0)) \quad (6.4)$$

where $W_{tot}(x, y, t)$ is the frame acquired at time t while $W_{tot}(x, y, 0)$ is the first frame of the sequence with values in digital counts. We are now capable of deriving the following expression for the emitted power of the object at time t in digital counts:

$$W_{obj}(x, y, t) = \frac{W_{tot}(x, y, t) - W_{tot}(x, y, 0)}{\epsilon} + W_{obj}(x, y, 0) \quad (6.5)$$

The missing information is now the $W_{obj}(x, y, 0)$, the power emitted by the object at the beginning of the measurement. We always started our measurements with the sample in full thermal equilibrium with the environment (uniform temperature equal to the ambient temperature). Thus, knowing the ambient temperature and the camera calibration curve we are able to compute:

$$W_{obj}(x, y, 0) = W(T_{amb}) = f_{cal}(T_{amb}) \quad (6.6)$$

where T_{amb} was determined using both a position with black body emission in the first frame and a thermometer close to the set-up. For all the measurements we had $T_{amb} = 23^\circ\text{C} = 296.15\text{ K}$. Finally we calculate:

$$\begin{aligned} T_{obj}(x, y, t) &= f_{cal}^{-1}(W_{obj}(x, y, t)) \\ &= f_{cal}^{-1}\left(\frac{W_{tot}(x, y, t) - W_{tot}(x, y, 0)}{\epsilon} + f_{cal}(T_{amb})\right) \end{aligned} \quad (6.7)$$

From the point of view of the error calculation we see that the uncertainty on the sample emissivity is responsible of a large uncertainty in the final calculated temperature [85]. Nevertheless, all of the measured samples present equal emissivity properties. Therefore, the systematic error introduced in this calculation does not affect the comparison of the results among different samples. Also, the error in temperature estimation does not affect the calculation of the transient time.

6. Macro-Scale Thermal Response ...

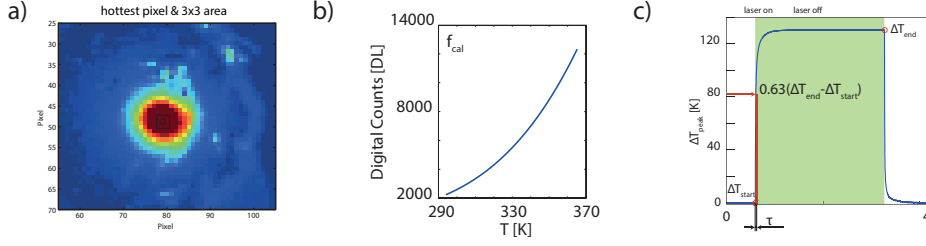


Figure 6.4: Temperature calculation. a) Digital count raw image. The small square indicates the identified hottest pixel and the larger square indicates the 3×3 pixels upon which we average the temperature. b) IR camera calibration curve at $410 \mu s$ integration time. d) Calculation of the characteristic rising time from the $T(t)$ curve.

After subtraction of the initial frame from the sequence, we determine the (x, y) position of the hottest pixel, which represent the position of the laser beam. We then consider the 3×3 pixels centered onto it (Figure 6.4.a) and calculate the mean temperature in that area. Subtracting the known ambient temperature we obtain the parameter $\Delta T_{peak}(t)$.

The calculation of the rising characteristic time requires a further processing of the sequence. We calculate the derivative of $\Delta T_{peak}(t)$ and identify the rising and decaying points as those with the highest derivative. The sign of the derivative identifies the rising from the decaying edges. The steady state temperature rise can be obtained subtracting the temperature value at the beginning of a rising edges from the T value at the beginning of the following decaying edge (Figure 6.4.c,d). Subsequently we calculate $T(\tau) = 0.63 \cdot \Delta T$. Finally, starting from the rising time position we follow the temperature curve until getting to $T(\tau)$ (eventually using a linear interpolation to compute the exact value). In this way, we obtain the characteristic temperature rising time.

From equation 6.7 we observe that, after subtraction of the initial frame, both signal and noise are divided by ϵ and thus get greatly enhanced. The steady state value of ΔT_{peak} could be extracted from every recorded sequence, eventually employing a moderate filtering for the noisiest cases. However, only high power measurements, which exhibit a large signal-to-noise ratio, were used to calculate the characteristic rising time τ , due to the difficulty in identifying the correct rising points among the noise.

Having performed each measurement with multiple rising and decaying edges, we can calculate the standard deviation on both ΔT_{peak} and τ and use this as the error. For ΔT_{peak} the obtained standard deviation was always below 1 K and thus we didn't report it in the plots. On the other hand, τ has significant standard deviations, which is what we reported as error-bars in the graphs.

6.3.3 Area Coverage Calculation

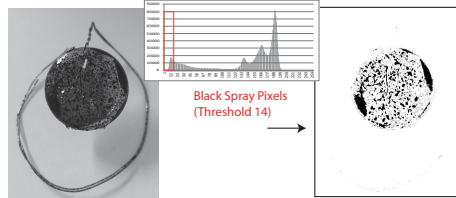


Figure 6.5: Calculation of the area coverage. Application of a threshold to the image (14) and calculation of the area coverage

To compare the absorption characteristic time with the commercial black spray we had to post-process the acquires pictures of the sample. We first convert the color image into a 16 bit one, then we set 14 as the color threshold. The generated image contains only the pixels with color below the chosen threshold. With *ImageJ* we can integrate all the obtained areas. The application of this procedure to the image of the sample before any spraying gives us the offset area value due to the black areas of the o-ring. We also calculate the total sample area and finally we can then compute the area coverage, AC , as:

$$AC = \frac{A_{threshold} - A_{threshold,0}}{A_{sample}} \quad (6.8)$$

For the studied cases we obtain area fractions of 17.7%, 34.1% and 82.7%.

6.3.4 Numerical Simulations

We performed finite element simulations (COMSOL) to investigate the power to temperature relation for a 2D (radial symmetry) model of our membrane.

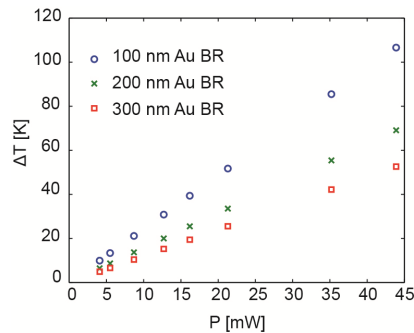


Figure 6.6: Simulated power to temperature curve for the three membranes with increasing beck reflector thickness.

We imposed a boundary heat source to represent the Gaussian laser intensity profile and solved for the temperature profile at different incident powers. From Figure 6.6 we see that there is a linear relationship between these two quantities. We adjusted the convection coefficient to match the 100 nm-Au-BR experimental curve and verified that the numerical results corresponded to the experimental ones also for the other two geometries considered (Figure 6.6 and Figure 6.9).

6.4 Results and Discussion

The described fabrication technique allows studying the light-to-heat conversion properties of an ultrathin plasmonic absorber on a cm^2 -scale and without the influence of a bulky supporting substrate. Indeed, the continuous gold back-reflector and SiO_2 layers provide enough mechanical stability to suspend the subwavelength thin membrane.

The right inset of Figure 6.1.c shows a picture of a free standing membrane of plasmonic absorber with diameter of 12 mm. Previously, we reported large broadband absorption of a similarly structured plasmonic absorber (Figure 6.1.c, red curve) measured from a μm^2 area with defect-less front pattern, as shown in the reported scanning electron micrograph (left inset of Figure 6.1.c). Such a broad absorption spectrum was obtained exploiting simultaneously four different plasmonic resonances originating both from the front pattern geometry and its coupling to the back reflector (see Chapter 3). Our large-scale (mm^2 -scale) absorption spectrum measurements (Figure 6.1.c, black curve) verify that, although the absorption is reduced by a few percent in the range of 400 – 600 nm, similar exceptional optical properties are well preserved on a larger scale, despite the unavoidable realistic fabrication imperfections in the front array such as grain boundaries, point defects, inhomogeneities etc.

Following absorption, plasmons quickly undergo non-radiative decay and the energy of the photons is converted into heat. The induced change in temperature could be exploited in a number of applications such as thermoelectric radiation sensors and thermal photovoltaics. We thus performed a series of transient thermal measurements to determine the magnitude (peak temperature, T_{peak}) and the speed (characteristic time, τ) of such temperature variations.

The steady-state value of ΔT_{peak} (when the laser is on in Figure 6.7.b) increases linearly with increasing irradiation power (Figure 6.7.a), as confirmed also by numerical simulations, carried out by using COMSOL Multiphysics software (see Section 6.3.4). With a laser power of approximately 60 mW we

6.4. Results and Discussion

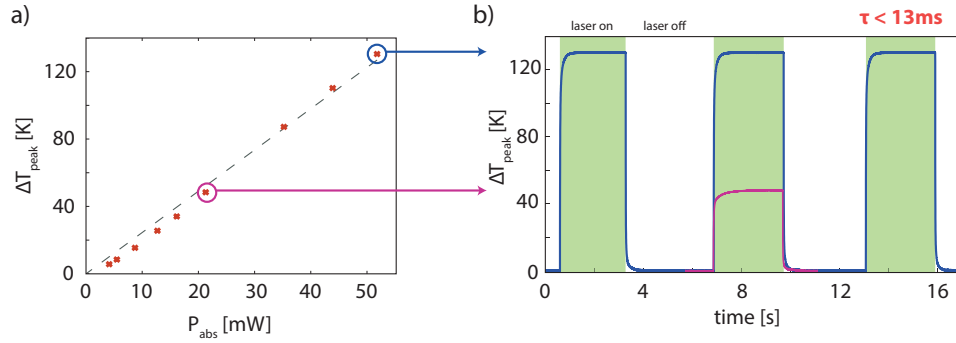


Figure 6.7: Absorption Properties, Experimental Set-up and Characteristic Thermal Response of the Broadband Plasmonic Absorber. a) Peak temperature increase as a function of the absorbed power. The dashed line represents a linear fit with zero intercept $\Delta T_{peak} = 2.45 \cdot P_{abs}$. b) Time evolution of temperature increase at maximum incident power (= 60.3 mW, absorbed power = 51.8 mW). The reached peak temperature determines the steady-state value of ΔT_{peak} , which is shown in (c). The purple curve shows the time evolution of temperature increase obtained for a lower incident power (= 24.8 mW, absorbed power = 21.3 mW).

were able to obtain steady-state values of ΔT_{peak} higher than 120 K. Moreover, the high signal-to-noise ratio of the measured curve for the highest incident power (Figure 6.7.b) allows the calculation of the system characteristic response time, defined here as the time during which ΔT_{peak} reaches from 0 to $(1 - 1/e)$ times of its maximum. For the case reported in Figure 6.7, the measured value is as small as $\tau = 12.6 \pm 1.3$ ms. This short response time is attributed to the small volume of our ultra-thin system and therefore, its practically negligible heat capacity ($C_{AuBR} + C_{SiO2} \approx 4.3 \cdot 10^{-5}$ J/K).

In order to assess the thermal performance of our absorber as coating, we compare it to a typical commercial broadband black spray coating. To ensure

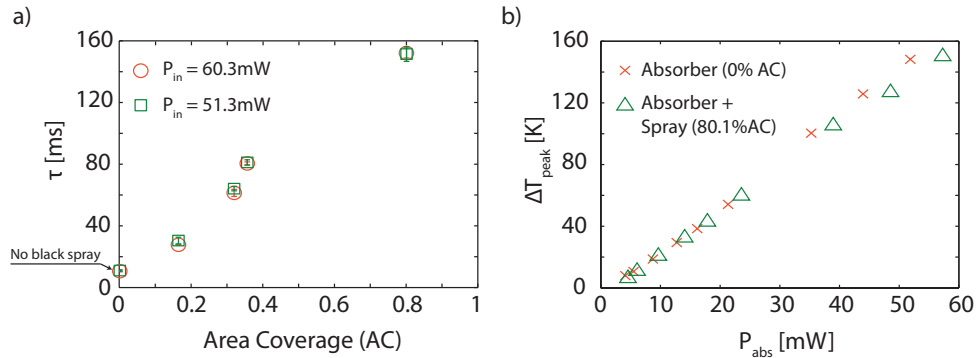


Figure 6.8: Comparison of the plasmonic absorber with a commercial absorbing coating (black spray). a) Change in characteristic time with increasing area coverage (AC) of the black spray; b) Peak steady state temperature versus absorbed power curve for the plasmonic absorber alone and the plasmonic absorber coated with black spray with area coverage of 80.1%.

6. Macro-Scale Thermal Response ...

a fair comparison of the two absorbing systems, we progressively coated one of our ultrathin absorbing membranes (Figure 6.8.a) with a commercial black spray (Krylon, ultra-flat black spray). After each spraying step, we measured the characteristic temperature rise time and the steady-state ΔT_{peak} value of the membrane. By doing so, we can attribute any variation in the thermal response of the membrane solely to the effect of the black spray. For each spraying step we also estimated the area covered by the black coating. For that, we took an image of the coated sample after each spraying step and processed it with an image analysis software (ImageJ, see section 6.3.3). In Figure 6.8.a we started from the as-fabricated absorber (black spray area coverage equal to zero) which has a characteristic time $\tau = 10.3 \pm 0.5$ ms and increased the black spray area coverage (AC) to 16.4%, 31.9%, 35.6% and finally 80.1%. We observe that even a very discontinuous black spray coating layer with only 16.4% AC increased the response time to $\tau = 27.4 \pm 0.1$ ms. The response time increases further for higher ACs and, for the case that the surface of the sample is almost completely covered (AC = 80.1%), it reaches the value $\tau = 152 \pm 3.2$ ms, which is more than one order of magnitude larger than the response time of the bare plasmonic absorber (Figure 6.8.a). On the other hand, the ΔT_{peak} vs. P_{abs} curves are similar for both cases of the bare and the spray coated plasmonic absorber (Figure 6.8.b). This similarity can be understood by considering the interplay which exists between thickness and thermal diffusivity of the layered structure. Indeed, upon increase of the sample thickness due to the black spray coating we would expect a reduction in peak temperature. However, the added spray layer has a very low thermal diffusivity ($\alpha_{spray} \approx 10^{-7}/10^{-8}$ m²/s [86], as compared to $\alpha_{gold} \approx 10^{-5}$ m²/s, $\alpha_{glass} \approx 10^{-6}$ m²/s) which improves temperature localization. At the same time, the increase in thickness and reduction in thermal diffusivity both have a detrimental effect on the transient response time, as seen in Figure 6.8.a.

To study in a systematic manner the role of the absorber thickness on the response time and peak temperature, while excluding other physical properties such as different thermal conductivities, we varied the thicknesses of the membrane by varying the thickness of the gold back-reflector from $h_{AuBR} = 100$ nm to $h_{AuBR} = 300$ nm. Changing this dimension does not influence the optical absorption properties of the layer (see Chapter 3). Figure 6.9.a,b show that the thinnest structure outperforms the other two for both considered criteria, rise time and thermal sensitivity. To this end, the thin plasmonic absorber has the highest light-to-heat conversion efficiency with absorbed power-to-temperature sensitivity of $2.45 \cdot 10^3$ K/W while the cases with 200 nm and 300 nm thick back reflectors have sensitivities of $1.5 \cdot 10^3$ K/W and $1.19 \cdot 10^3$ K/W, respectively. The thinnest absorber has also the fastest response of all, $\tau = 12.6 \pm 1.3$ ms, while the rise time increases to

6.4. Results and Discussion

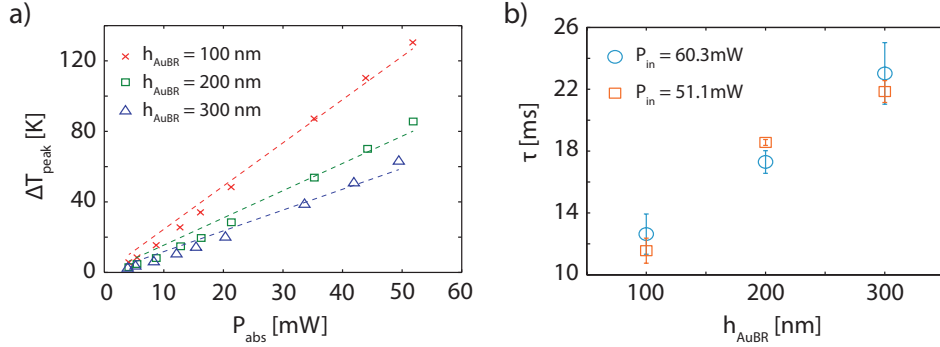


Figure 6.9: Effect of Absorber Thickness. a) Peak temperature as a function of absorbed power for samples with different thicknesses of the back reflector; b) Characteristic time as a function of the back reflector thickness for two different incident powers.

17.3 ± 0.7 ms and 23 ± 2 ms for the samples with 200 nm and 300 nm thick back reflectors, respectively (here, $P_{\text{in}} = 60.3$ mW). These results are also consistent with numerical simulations (see section 6.3.4). Therefore, reducing the absorber thickness concurrently improves sensitivity and characteristic temperature rise time of the structure.

For applications where working temperatures are as high as hundreds of degrees, such as thermal-photovoltaics, losses through re-emission of thermal radiation are significant and selective coatings with negligible emission in IR are highly desirable. We calculated the absorption coefficient of the proposed broadband plasmonic absorber across the visible and IR spectrum up to wavelength $12 \mu\text{m}$, which corresponds to the peak emission wavelength of

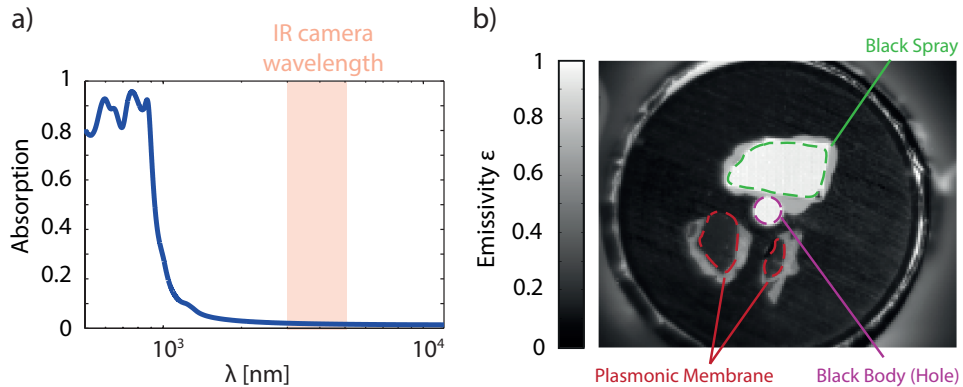


Figure 6.10: Absorption and Emissivity in IR range. a) Simulated absorption spectrum (equivalently emissivity spectrum) of the broadband plasmonic absorber. The shaded area represents the wavelength window used by the IR camera. b) Emissivity map measured with the IR camera in the range 3–5 μm for a membrane coated with the plasmonic absorber (dashed-red lines) and for a membrane coated with the black spray (dashed green line).

6. Macro-Scale Thermal Response ...

a black-body at 240 K (Figure 6.10.a). The dielectric data for gold and glass were taken from literature [87], [88]. Since emissivity is equal to optical absorption, Figure 6.10.a equivalently represents the emissivity spectrum of the absorber. As shown in this figure, absorption, and therefore, thermal emissivity, drops to very small values (below 10%) for wavelengths longer than 1000 nm.

Using the IR camera we were able to determine the emissivity of the plasmonic absorber in the spectral range 3 – 5 μm . We cut small pieces of plasmonic absorber membrane and a membrane coated with black spray and pasted them to the top facet of a metallic cylinder by a thermally conductive silver paste (Figure 6.10.b). This guarantees that the membrane pieces and the cylinder stay at the same temperature. The cylinder has a deep hole which emits like a black-body [84] and can be used as a reference for measuring the absolute temperature and calibrating camera measurements (see section 6.3.2). We heated up the cylinder to 41.6°C and then to 52.6°C and, by subtracting the two IR images we acquired an emissivity map of the system, which is shown in Figure 6.10.b. We observe that while the black-spray coated membrane has an emissivity close to unity, similar to the hole (black-body), the plasmonic absorber membrane has a much smaller emissivity $\epsilon = 0.16 \pm 0.1$. This confirms the spectral selectivity of the plasmonic absorber.

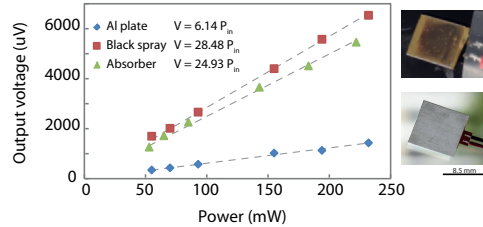


Figure 6.11: Sensitivity Measurements on a Real Thermoelectric Sensor. The graph shows the sensitivity curves measured for the same sensor without coating (blue diamonds), with the absorber (green triangles) and with a standard blackening spray (red squares). The two inset on the right show the bare sensor (lower inset) and the sensor coated with the absorber (upper inset).

In collaboration with GreenTEG, we tested our absorber on a real thermoelectric sensor. As shown in Figure 6.11, the sensitivity obtained with our absorber (green triangles) was similar to the use of a blackening spray (red squares) and much higher compared to the case of no absorbing material (blue diamonds). Even though we performed some preliminary transient measurements, the characteristic time of the system is always dominated by the sensor bulk response, due to its large thickness ($\approx 400 \mu\text{m}$). Neverthe-

less, experiments on thinner sensors are currently being performed and we are confident they will show significant advantages of the absorber compared to the blackening spray.

6.5 Conclusions

In conclusion, we fabricated a large-scale, free-standing MIM-plasmonic light absorber with subwavelength thickness and studied its light-to-heat conversion capabilities. We showed that, compared to a commercial thin-film black coating, a plasmonic absorber exhibits more than one order of magnitude faster transient response with comparable absorbed light power-to-temperature sensitivity. In particular, we studied the effect of increasing the absorber thickness and demonstrated that its ultrathin feature plays a fundamental role in determining the characteristic time response and thermal sensitivity. Furthermore, we demonstrated the spectral selectivity of our plasmonic coating and showed that it exhibits high absorption across the entire visible range but low emissivity in the IR range. Therefore, such plasmonic absorbers are excellent candidates to achieve fast and effective broadband light-to-heat conversion in a host of applications. Their exceptional optical absorption and thermal properties could be especially exploited to increasing the speed of visible-light thermal sensors, as well as to improve the efficiency of solar thermoelectric devices by suppressing undesired radiation losses.

Chapter 7

Direct Observation of Charge Separation on Au Localized Surface Plasmon

Part of this chapter has been published in *Energy and Environmental Science*, 2013, 6(12), pp.3584 – 3588

7.1 Abstract

Plasmonic nano-structures of d^{10} metals are suggested to be the future of photo-voltaics and photo-catalysis under solar irradiation thanks to their large light absorption cross-section, versatility, and stability. We investigated the impact of continuous plasmon excitation at 532 nm on the density of states of gold nanoparticles, and found an increase of the unoccupied density of d states of gold nanoparticles at the Fermi level, consistent with the formation of electron-hole pairs. Some of those electrons have sufficient energy to overcome the Schottky barrier, and be injected into TiO_2 conduction band. The results confirm that d^{10} metals plasmonic structures can act as light sensitizers and photo-catalysts.

7.2 Introduction

In the early seventies Honda and Fujishima [89] used TiO_2 to photo-assist the electrochemical splitting of water. Shortly after, Inoue et al. [90] demonstrated that CO_2 too could be photo-reduced to a plethora of hydrocarbons, using powder semiconductors, including TiO_2 . These ground-breaking discoveries were hampered by the semiconductors large band gap (> 3 eV).

7. Direct Observation of Charge Separation ...

Indeed, in order to induce charge separation UV-A (300 – 400 nm) irradiation is required, which represents only a small fraction of the solar spectrum. Nevertheless, TiO_2 remains indisputably the best performing photo-catalyst to date [91]. Several efforts have been made to improve visible light absorption by direct manipulation of the TiO_2 band gap generally by doping with elements, such as N , C and S [92]. However, this might become counterproductive because by narrowing the band gap one decreases the breath of reactions that can be photo-catalysed. As a reminder, a photo-catalytic reaction can take place when its redox reaction potential follows within the semiconductor band gap. Conceptually, the use of sensitizers circumvents the visible light absorption deficiency of TiO_2 because they are capable of harvesting solar light, and injecting hot electrons into the TiO_2 conduction band (CB). This is the principle of dye-sensitized solar cell (DSSCs)[93, 94]. Their success is based on fast electron injection (< 1 ps), and slow back electron transfer. However, they can have low photo-stability, discrete absorption levels (narrow-band), and small optical cross-sections. This means they require high dye coverage, which diminishes the space available for photo-catalytic reactions. Metallic nanoparticles (NPs) are interesting sensitizer candidates because of their localized surface plasmons (LSP), which have large optical cross-sections. Gold group metals exhibit plasmonic resonances, which can be tuned by changing their shape, size and/or composition, enabling a good match with the solar spectrum [95]. Furthermore, due to their d^{10} configuration they are chemically stable. Recently, the excitation of Au and Ag LSP nanostructures was shown to improve solar cell charge transfer from sensitizer to semiconductor [96, 97, 98, 99], increase the photocurrents under solar irradiation [100, 20, 101, 102], and improve photo-initiated catalytic oxidations [103, 104, 105, 17, 106, 107, 108, 109, 18, 110, 111]. The physical principles that governed plasmons were comprehensively described elsewhere [112, 113, 114, 12, 13, 115]. However, there are several open questions related to the plasmon excitation and electron injection into the semiconductor CB. Furube et al. [116] suggested that the excited plasmon band overlaps with an interband transition in gold, leading to the excitation of electrons in the filled d-band to electronic states above the Fermi level. The collective electron excitation provides enough energy to some of the electrons so that they can overcome the $Au - TiO_2$ Schottky barrier [117], which is of about ≈ 1.0 eV [118, 119, 120]. The aim of this chapter is to first demonstrate that LSP excitation indeed does change the gold d-band occupancy and second, that some of the generated hot electrons possess enough energy to overcome the Schottky barrier and be injected into the TiO_2 CB, which would validate the suggested mechanism. In a recent perspective, Aruda et al. [121] highlighted that changes in the metallic structure itself under plasmonic excitation de-

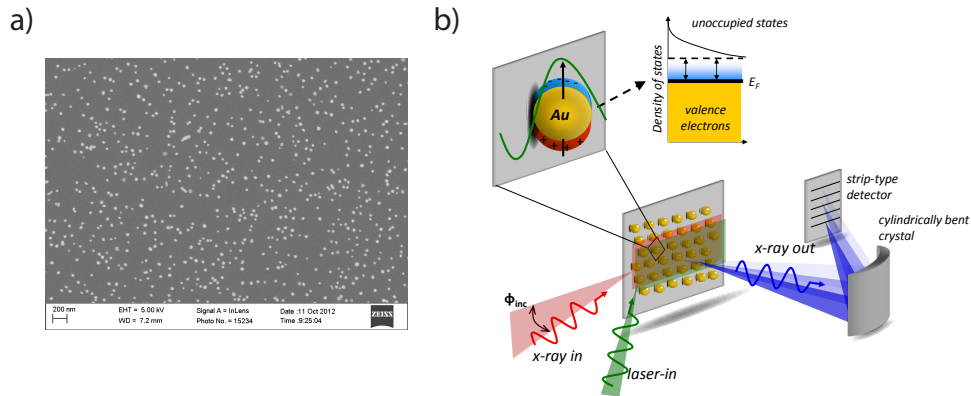


Figure 7.1: HR-XAS experimental procedure a) Description of the experimental procedure used to determine the changes in Au L_{III} -edge induced by continuous wave laser excitation of LSP at 532nm, with 100 mW power. b) SEM micrograph of the one of the measured samples showing the 40nm Au NPs supported on passivated Si.

picting charge separation and formation of hot electrons was not reported so far.

7.3 Methods

7.3.1 HR-XAS Measurements

We used high-resolution X-ray absorption spectroscopy (HR-XAS) at the Au L_{III} -edge to probe the creation of hot electrons (electron-hole pairs) due to LSP excitation. HR-XAS is sensitive to the unoccupied density-of-states in the metal.

Sample Preparation

An array of Au NPs with a diameter of ca. 40nm (largely spaced, > 100 nm, Figure 7.1.a) was fabricated by block-copolymer lithography [122, 123, 124] on 1 cm² Si chip.

First we prepared a solution of toluene (5 ml) and the block-copolymer Polystyrene - 2Polyvinylpyridine (PS-b-2PVP) which we stirred at a moderate speed for more than 24 h to ensure the complete dissolution of the block copolymer. Then we added 14.5 mg of $HAuCl_4 \cdot 3H_2O$ salt to the initial solution and continued stirring for more 24 h until the uptake of the gold salt into the block-copolymer micelles was complete and the solution presented a bright yellow color.

7. Direct Observation of Charge Separation ...

On each Si chip we spin coated approximately $10\mu\text{l}$ of the final block-copolymer solution at 1000 rpm and for 30 s. Then the sample was exposed to a short oxygen treatment (20 s, 100 W, 0.2 mbar) to favor the formation of the initial gold cluster within each micelle. In order to enlarge these initial gold clusters, we dipped the samples for approximately 60 s in a 0.1 % $\text{HAuCl}_4 \cdot 3\text{H}_2\text{O}$ - 0.2 mM NH_3OHCl water solution. After drying with a gently nitrogen flow, the samples were exposed to a second, longer plasma treatment (30 min, 150 W, 0.4 mbar) which completely removed the polymer micelle leaving only the gold nanoparticles onto the Si substrate, as shown in Figure 7.1.a.

HR-XAS Set-up

The schematics of the HR-XAS set-up is shown in Figure 7.1.b. The Au NPs array was irradiated with incoming x-rays at a grazing incident angle ca. 1.5° . The x-rays photons were overlapped with continuous-wave (CW) laser (532 nm, 150 mW power) photons, also at a grazing incident angle ca. 2° . The measurements were performed at the SuperXAS beamline of the Swiss Light Source (SLS) at the Paul Scherrer Institute, Switzerland. The X-ray beam delivered by the 2.9 Tesla super-cooled bending magnet was collimated by a spherically bent Rh mirror. The collimated X-rays were monochromatized by means of a double Si (111) crystal monochromator and focused by a toroidally bent Rh mirror. On the sample the photon flux was $7 - 8 \cdot 10^{11}$ photons/sec with an energy resolution of $\Delta E/E \approx 1.4 \cdot 10^{-4}$ and a spot size of $100 \times 100 \mu\text{m}^2$. For calibration a 4 μm thick Au foil was used. The emitted x-rays were collected with a dispersive von Hamos-type spectrometer [125, 126], which avoids component scanning during the acquisition. The grazing incidence experimental geometry provides a line-like probe with a large number of irradiated particles thus enhancing the x-ray detection efficiency. Because the employed von Hamos geometry accepts a line-like source the grazing incident scheme does not affect the experimental resolution. To our knowledge, the application of grazing incidence with the von Hamos geometry is demonstrated here for the first time. Briefly, the x-rays emitted from the sample were diffracted by a Ge (660) crystal bent cylindrically to a radius of curvature of 25 cm. The crystal size was 10 cm and 5 cm in the focusing and dispersive axes, respectively. For the detection of the diffracted photons, a 1D-array, single photon counting, Mythen II was used. The spectrometer was operated in the vertical scattering geometry. Spectra were acquired around the Au L_{III} -edge located at 11919 eV.

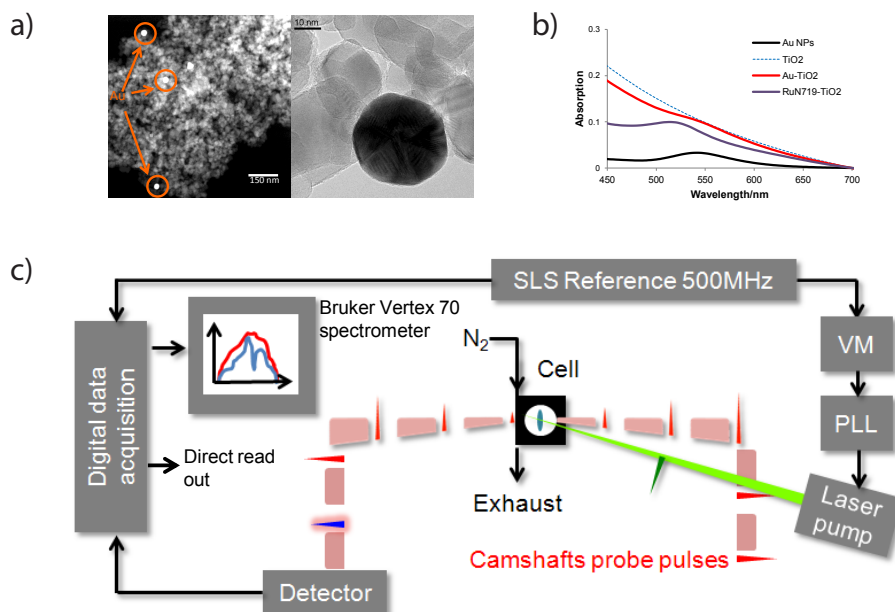


Figure 7.2: Transient mid-IR measurements a) TEM images of Au-TiO₂. Left, overview image depicting low-loading Au nanoparticle density; right, image of a representative Au nanoparticle with roughly 30 – 40 nm diameter. b) UV-vis spectra of the mid-IR samples. c) Schematic representation of the SLS IR pump-probe setup. Both the pulsed laser at 532nm and the digital data acquisition were synchronized to the SLS reference frequency of 500MHz.

FDMNES Calculations

To support our HR-XAS experimental results, we performed FDMNES [127] calculations revealing the absorption cross sections of photons around the ionization edge. FDMNES is a commonly used code to simulate X-ray absorption spectroscopy (XANES, XMCD) or resonant scattering (RXD) spectra collected at synchrotrons [127]. Its ab initio approach reduces all the methodological parameters. FDMNES uses time dependent density functional theory (TD-DFT) for better description of excited states linked to the photon-matter interaction [128]. The only change in the input parameter file performed was the electronic configuration of Au.

7.3.2 IR Measurements

To confirm that the photo-generated hot electrons have sufficient energy to overcome the Schottky barrier and be injected into the TiO_2 CB, we performed transient broadband mid-IR (infrared) spectroscopy [129, 130] on systems comprised of TiO_2 anatase powder coated with a sensitizer.

Sample Preparation

TiO_2 NPs were prepared via the sol-gel method [131]. The synthesis was carried out in a glove box under argon atmosphere. Titanium isopropoxide was dispersed in 10 mL 2-propanol. The resultant mixture was added drop wise under vigorous stirring to cold acidic water (2°, 250 mL H_2O , 18 M mixed with 80 mL glacial acetic acid, final pH 2). The sample was left under vigorous stirring in an ice bath for 12h. After which the sample was peptized at 80°C for 2h until the liquid turns into a transparent gel. The gel was autoclaved at 230°C for 12 h. During this process the amorphous sample undergoes a phase transition leading to the formation of anatase NPs 20 nm (125000 TiO_2 units) in size. We used two types of sensitizers, namely:

- 30–40 nm Au NPs (Biocell) sparsely distributed and a loading 0.5 wt.% Au. A solution containing the NPs was added to a suspension of TiO_2 at room temperature. The sample was kept under vigorous stirring for 2h. The sample was dried overnight at 100°C. The sample was used as prepared. Figure 7.2.a shows transmission electron microscopy (TEM) pictures of the sample. A suspension of $Au - TiO_2$ in ethanol was used to prepare TEM specimen.
- $RuN719$ dye was used as reference sensitizer. To achieve monolayer coverage of TiO_2 NPs nanoparticles at a concentration of 5 g/L we dissolve 170 mg of $RuN71$ in di-methyl formamide (DMF) [132]. The anatase nanoparticles were mixed with the dye solution for half a day. To ensure that all dye is bonded to TiO_2 , the suspension was left for several days in order to settle and then washed several times with DMF until the resultant DMF from the washing was clear. In order to avoid mid-IR signal saturation the sample was diluted tenfold with pure TiO_2 . Representative UV-Vis spectra of the samples are depicted in Figure 7.2.b. The samples were measured using a Perkin-Elmer Lambda 2000 spectrometer. The samples were measured as acidic water suspension concentration 0.5 mg/mL (sample/acid water), except the $RuN719 - TiO_2$, which was measured with a dilution of 0.05mg/mL.

The UV-Vis spectrum of Au NPs reveal a peak centered at 544 nm ascribed to plasmonic resonance of gold (Figure 7.2.b). The peak decreases in intensity when the NPs are loaded onto TiO_2 , which is associated with the dilution factor. The $RuN719 - TiO_2$ reveals a characteristic absorption centered at around 525 nm. TiO_2 shows no absorption band in the region between 400 – 800 nm. The rising background measured for all samples containing TiO_2 are related to light scattering due to the milky nature of the solution, especially for the more concentrated samples (TiO_2 and $Au - TiO_2$).

IR Set-up

We performed transient mid-IR absorption technique using the recently developed synchrotron based pump-probe setup with 100 ps time resolution, as given by the synchrotron radiation bunch length, installed at the Infrared beamline of the SLS [129, 130], Figure 7.2.c. Advantages of synchrotron-based experiments include large dynamic range and the sensitivity of the system combined with the large spectral bandwidth, which covers the entire mid-IR range (approx. 625 to 10000 cm^{-1}). The multi-wavelength laser light system uses near-IR laser pulses generated by a Nd:YAG system and parametric down and up-conversion. A Phase-Lock Loop (PLL) control system locks the laser system to the SLS reference frequency of 500 MHz. The delay between the 80 ps pump pulse from the laser system and the relevant synchrotron radiation pulse, the so-called camshaft (4 times the charge of a standard bunch), is electronically tuned by a vector modulator (VM). This allows adding an arbitrary phase delay, and hence a time delay of up to 1 ms. The transmission of the camshaft pulses was measured with a fast Peltier-cooled mercury cadmium telluride (MCT) detector featuring a bandwidth of 800 MHz. The peak amplitude is digitized with a 14-bit resolution fast-sampling card, which records both pumped and unpumped transmission (arriving 1 s in advance) instantaneously. Hence, this detection scheme is not susceptible to instabilities of the synchrotron source (manifested at the 1 to 3 kHz range) and slow drift phenomena, and it allows increasing the signal-to-noise ratio (S/N) of step-scan experiments significantly (typically by a factor of 100) on a time scale relevant to our experiments. The samples were excited with 33 mW of Nd:YAG pulsed monochromatic green (532nm) light. We used a resolution of 32 cm^{-1} to avoid contributions from *RuN719* molecular vibrations. To ensure good S/N, the presented spectra correspond to the average of data collected over a period of 24 h (2 – 3h per average spectrum). The changes obtained from the interferogram were found to be the same as the ones detected by integration of the signal difference directly from the digital data acquisition. Since direct read out decreases significantly the acquisition time, we used it to measure the signal difference at longer delay times (2 – 80 ns). However it must be emphasized that this approach can only be used if one is evaluating a single event, which is the case.

7.4 Results and Discussion

The results of the high-resolution X-ray absorption spectroscopy (HR-XAS) at the Au L_{III} -edge are shown in Figure 7.3. The unexcited Au L_{III} -edge

7. Direct Observation of Charge Separation ...

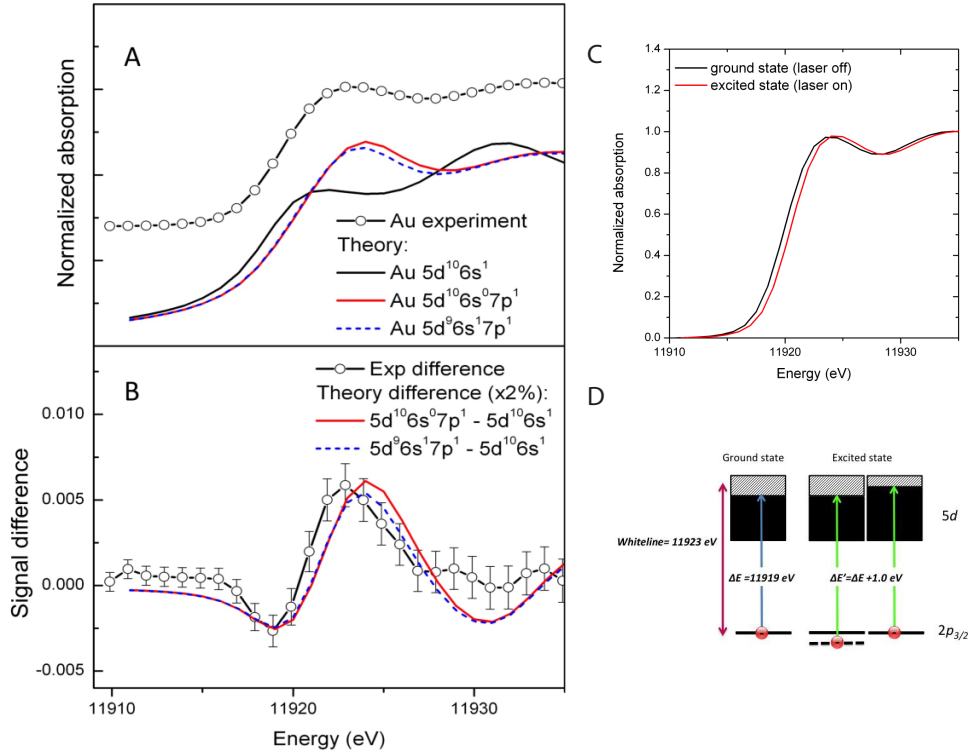


Figure 7.3: HR HR-XAS experiments depicting changes in Au L_{III} -edge induced by continuous wave laser excitation of LSP at 532 nm, with 100 mW power A) HR-XAS ground state spectrum of Au NPs (open circles black trace), FDMNES calculated spectrum of ground state (black trace Au $5d^{10}6s^1$) and excited states (red trace $5d^{10}6s^07p^1$) and (blue trace $5d^96s^17p^1$); B) Difference spectra between excited and ground state: experimental (open circles black trace), and calculated assuming 2% excitation Au $5d^{10}6s^17p^0 \rightarrow Au5d^{10}6s^07p^1$ (red trace); $Au5d^{10}6s^17p^0 \rightarrow Au5d^96s^07p^1$ (dashed blue trace); C) Excited and ground state spectra; D) Motifs responsible for the ionization threshold energy blue shift.

spectrum (open circles black trace) and the spectral difference resulting from laser excitation (Laser ON - Laser OFF (open circles black trace)) are shown in Figure 7.3.a,b respectively. The HR-XAS spectra of excited and ground state Au NPs are depicted in Figure 7.3.c. Au NPs spectrum is characterized by the resonance threshold at 11923 eV (whiteline) associated with a $2p_{3/2} \rightarrow 5d$ dipole transition, reflecting the unoccupied d density of states above the Fermi level. The unoccupied states above the Fermi level in Au ($5d^{10}6s^1$) arise from s-d hybridization [133, 134, 135, 136]. The difference spectrum reveals a derivative-like profile, whose negative part is assigned to an upward shift of the ionization threshold energy ($\Delta E = 11919$ eV) by ca. 1.2 to 1.0 eV, assuming 1 – 3% excitation yield, respectively.

To support our assignment, we performed FDMNES [127] calculations revealing the absorption cross sections of photons around the ionization edge. The excited spectrum due to the excitation from ground state Au $5d^{10}6s^1$

7.4. Results and Discussion

(black trace) electron to unoccupied $7p$ orbital when we excited the $6s^1$ ([Au $5d^{10}6s^07p^1$] red trace) or $5d^{10}$ ([Au $5d^96s^17p^1$] dashed blue trace) electrons are depicted in Figure 7.3.a. The calculated spectral differences between excited and ground state assuming 2% excitation are depicted in Figure 7.3.b (red trace [Au $5d^{10}6s^17p^0$] \rightarrow [Au $5d^{10}6s^07p^1$]; dashed blue trace [Au $5d^{10}6s^17p^0$] \rightarrow [Au $5d^96s^07p^1$]). The similarity between excitation of a $6s^1$ and $5d^{10}$ electrons is expected due to the $6s$ - $5d$ hybridization. The excited spectrum shows a shift in the ionization threshold, and an increase in the whiteness intensity, as detected experimentally. Figure 7.3.d depicts a schematic representation of potential causes for the ionization threshold energy shift. In the present case, the ionization threshold energy is the energy difference between the $2p_{3/2}$ and the unoccupied $5d$ states, i.e., the energy necessary to excite the electron from $2p_{3/2}$ to unoccupied $5d$ states. LSP excitation induces a blue shift of the ionization threshold energy of about 1.0 eV ($\Delta E' = \Delta E + 1.0$ eV). The result can be rationalized in two ways, either a change in the $2p_{3/2}$ states due to electron screening or shift in the highest occupied band, which cannot be differentiated with HR-XAS.

The increase in whiteness intensity (11923 eV) is synonymous of an increase of holes in Au d-band. Plasmon excitation is a collective phenomenon, in which the excess energy is distributed among many atoms when viewed over an extended period of time, however at a given instant the energy is likely to be carried out by a single electron [137]. Therefore it is plausible that this electron has sufficient energy to be excited to a higher level (hot electron formation) and create a hole in the valence states (d-band) [138], as suggested by the HR-XAS measurements. The final energy of the created hot electrons is not the same [116] making it difficult to determine their final states since HR-XAS detects hole density, not electrons. Since the main decay channel of the excited state is electron thermalization [139], spectral changes due to thermal contributions are anticipated. We estimated the thermal contribution to the spectrum by expanding the Au lattice parameters [140, 141, 142]. Au NPs surface excited at 532 nm can experience temperatures in excess of 500°C for submicrosecond times [46]. Therefore we calculated the spectra difference for 2% lattice expansion, which equates to approximately 600°C according to Christensen et al. [141]. The outcome of the calculation is depicted in Figure 7.4. The thermal contribution decreases all the spectral features, in particular the unoccupied density of states, contrary to what we measured. Thus the detected signal contains the fingerprint for hot electron (electron-hole pair) formation with little contribution from lattice expansion.

Free and trapped electrons in a semiconductor CB lead to the appearance of a distinct broad mid-IR absorption band [143, 144, 145, 146]. Figure 7.5.a

7. Direct Observation of Charge Separation ...

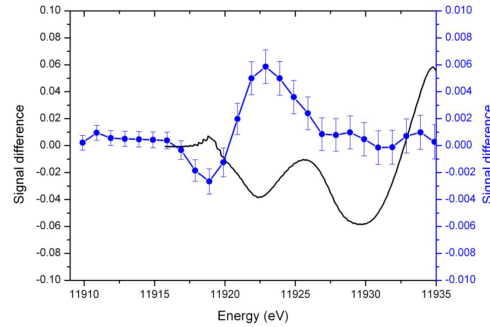


Figure 7.4: Theoretical estimation of XAS spectral change due to thermal expansion. Blue measured signal and black the estimated signal changed due to 2% of Au lattice expansion, which equates to about 600°C , according to Christensen [141].

shows the integrated mid-IR transient signal of $\text{Au} - \text{TiO}_2$. Figure 7.5.b depicts the mid-IR transient spectra for two delay times. For comparison purposes we plotted the signal for the system consisting of the ruthenium *N719* dye adsorbed on TiO_2 , measured with the same experimental parameters.

Upon excitation, the sample transmittance strongly decreases due to the appearance of broad mid-IR band associated with the presence of electrons in the TiO_2 CB, Figure 7.5.a. The minimum in transmittance was observed at $t = 0$ ps for both systems. This is the time assigned to the best possible overlap between pump and probe pulses, confirming fast injection, which we cannot resolve due to our time resolution (100 ps). Furube et al. [116] suggested that electron injection from gold to TiO_2 occurs in less than 240 fs. Recent reports suggest electron injection from the *N719*-dye system occurs in < 10 fs [147], and from graphene quantum dots in < 15 fs [148]. The

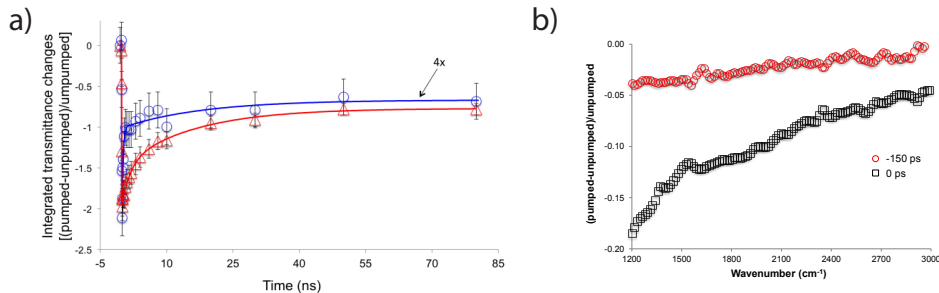


Figure 7.5: Transient mid-IR measurements a) Transient mid-IR measurements of TiO_2 coated with a light absorber irradiated at 532 nm with 100 ps pump pulses and 33 mW energy. The spectral changes were probed with 100 ps broad mid-IR pulses at a spectral resolution of 32 cm^{-1} . Time dependence of the integrated mid-IR signal of $\text{Au} - \text{TiO}_2$ (O) and $\text{N719} - \text{TiO}_2$ (Δ) b) Time dependence of the mid-IR of TiO_2 coated with *Ru - N719* dye irradiated at 532 nm with 100 ps pump pulses with energy of 33 J. Experimental resolution 32 cm^{-1} .

7.4. Results and Discussion

detection of electrons in the TiO_2 CB confirms that some of the generated hot electrons have sufficient energy to overcome the Schottky barrier and be injected into the TiO_2 CB [149]. It should be mentioned that the signal is not associated to the direct excitation of TiO_2 band gap because the excitation energy is not enough to overcome the band gap and multi-photon absorption does not occur, nor is it due to Au NPs because their typical IR absorption is not in the mid-IR range [116]. After injection, only 20% of Au NPs and 50% of *N719* signal recovered within the measurement time (80 ns). A bi-exponential behavior with $\tau_1 = 1.9 \pm 0.42$ ns and $\tau_2 = 16.0 \pm 3.1$ ns for *N719-TiO2* and $\tau_1 = 0.21 \pm 0.03$ ns and $\tau_2 = 18.1 \pm 10.3$ ns for *Au-TiO2*, were fitted. The charge decays are associated to the recombination of injected electrons with holes in the Au NPs or photo-oxidized dye. The different recombination times are due to distinct times that the electrons take to reach the surface and react with the holes of the sensitizer, which depends on electron dynamic free path and their energy. Since the IR signal does not recover completely during the measurement time (80 ns) at least a third component must be involved, which is most likely to be related to electron-hole recombination of electrons that hopped between TiO_2 particles [150, 151]. Charge hopping transport between TiO_2 particles is a resistive phenomenon, which in practical terms slows the recombination process. It should be emphasized that both samples contained pristine TiO_2 particles. Full relaxation occurs in the millisecond and beyond time scales [152]. The observed differences for the faster time decay are significant and hints to a different decay mechanism. However, our experimental time resolution (100 ps) is not sufficient to clarify this aspect. It should be emphasized, that transient IR measurements were performed with the single purpose of confirming that some electrons have indeed enough energy to be injected into TiO_2 , upon electron-hole pair formation. The relative electron injection yield revealed that Au NPs injected roughly 20 – 25% of the electrons into TiO_2 comparatively to *N719*. Relative injection yield is the ratio between Au NPs and *N719* integrated transient infrared signal normalized according to sample optical density at a specific delay time. Efficiencies of about 11.1% have been reported for *N719* dye-system [153, 154]. The Au NPs injection yield is very encouraging because it can be improved by increasing metal loading, optimizing sensitizer-semiconductor contact points [155], to name only a few. The low Au loading was selected to prevent inter-particle communication [156, 157, 158].

7.5 Conclusions

In conclusion, we detected the formation of electron-hole pairs (hot electrons) and demonstrated that some of those electrons possess enough energy to be injected into TiO_2 . The presented results validate retroactively the rationalization of their catalytic and photo-voltaic enhancements on the basis of the electronic mechanism [96, 97, 98, 99, 100, 20, 101, 102, 103, 104, 105, 17, 106, 107, 108, 109, 18, 110, 111, 112, 113, 114, 12, 13, 115, 116, 117]. The inherent properties of gold group plasmonic nanostructures with respect to chemical stability, high optical cross-section and tunable optical properties, make them very promising for harvesting of visible light. Their properties can be further exploited by combining them with photo-catalysts, such as TiO_2 to drive photo-catalytic processes under solar irradiation. Furthermore the materials can be used as composite materials [159, 160], e.g. with the LSP NPs at the core and TiO_2 at the surface, for a plethora of sunlight driven photo-reactions from fuel to bulk and fine chemical production. This strategy enables the photochemical reaction on pristine and/or metal-doped TiO_2 under visible irradiation without compromising the surface area availability, which is a major issue with the dye-systems.

Chapter 8

Conclusions and Outlook

Concluding, in this thesis we have addressed the problem of efficient harvesting, confinement and conversion of the energy of light using facile plasmonic nanostructures.

Concerning the light-harvesting process, we have shown the design and experimental realization of a novel broadband, ultra-thin plasmonic absorber which could be employed for efficient sunlight absorption. The proposed structure is capable of harvesting more than 88 % of the Sun energy in the spectral range 380 – 980 nm, thanks to the simultaneous exploitation of four different plasmonic phenomena which we combine to obtain a continuous absorption band. Moreover, in accordance with sunlight characteristics, our design is polarization insensitive and preserves its performance for incidence angles up to 48 deg. Furthermore, the fabrication process is compatible with large-scale production procedures and the multilayer structure is advantageous for the integration in real devices.

We then demonstrated a facile geometry which allows for extreme light confinement and could be thus used in combination with different active materials, e.g. lasers, photocatalytic reactors. For this purpose we considered a metal-insulator-metal structure with ultra-thin dielectric spacer 7 – 13 nm. The front pattern consisted of a hexagonal array of tapered triangles which eventually connected forming a continuous, holey metallic layer. We showed that, in the disconnected configuration, the nanocavities were completely isolated from each other, even for small physical separation. Therefore, such design would be advantageous for highly integrated optical components. Moreover, we demonstrated that in the connected configuration, exploiting the non-uniform width of the structure and its symmetries, it is possible to locally achieve mode confinement in a nanocavity whose physical size is almost 20 times smaller than its optical size. At the same time, the presence of two continuous metal electrodes could be advantageous for those

8. Conclusions and Outlook

applications, like the one mentioned above, which require electrical control or electrical access.

Finally, we considered two possible light conversion processes, namely light-to-heat and light-to-hot electrons conversion. On the one hand, we used infrared thermography to investigate the thermal response of a broadband plasmonic absorber, and showed that, thanks to the reduced thickness and high absorption, its characteristic time is almost two orders of magnitude smaller than commercial systems of equivalent size. At the same time, it exhibits a comparable temperature rising capability. Also, we presented preliminary results demonstrating the successful large-scale implementation of such absorber in a fast thermoelectric radiation sensor. At last, using x-ray spectroscopy, we measured, for the first time, the change in the density of states of gold plasmonic nanoparticles during plasmonic excitation. We proved that a significant shift in the Fermi level occurs (1 eV shift), confirming the capability of plasmonic nanostructures to act as sensitizers, eventually improving the performance of a catalyst.

In perspective, further steps towards the application of these structures in real devices should be taken. Concerning the light-to-heat conversion processes, a series of fundamental studies on the thermal behavior of multilayer, efficient absorbers is still missing, all significant studies being so far focused on elemental arrangements of simple plasmonic nanoparticles. At the same time, moving towards real applications, a thin and fast thermoelectric system should be found in order to exploit the full potential of the designed ultra-thin plasmonic absorber. On the other hand, for photocatalytic or photovoltaic applications, the inert dielectric layer used so far should be replaced by the actual active material (e.g. TiO_2 , Si) and the complex interplay between different processes and materials, e.g. charge transfer and recombination processes, formation of interfacial energy barriers etc., should be investigated.

Appendices

Appendix A

Evolution of Plasmonic Crystal Modes from Plasmonic Atomic Modes

A.1 Abstract

We briefly investigate the applicability of solid state concepts like plasmonic atoms, molecules and crystals to proximal gap plasmon nanocavities. We compare the spectrum of finite groups of interacting proximal gap plasmon nanocavities to that of the single isolated nanocavity (plasmonic atom) and the infinite array (plasmonic crystal). We observe that plasmonic molecules spectra present interesting features which are analogous to surface and bulk states in real crystal. The surface state mode strength progressively reduces eventually disappearing for the infinite array while the resonance peak resembling the infinite crystal resonance mode becomes dominant.

A.2 Introduction

In the previous chapters we have largely investigated the optical characteristics of infinite, defect-less, arrays of proximal gap plasmons (GP) nanocavities both in the electrically disconnected and connected configurations. In particular, we highlighted the role of symmetry and boundary conditions on the abrupt change in optical properties between these two states of the system. Furthermore, we showed how, in the disconnected configuration, the array is nothing but a collection of individual, isolated gap-plasmon nanocavities which only interact upon achievement of physical contact. Naming every single plasmonic gap plasmon nanocavity a *plasmonic atom*, we could state

A. Evolution of Plasmonic Crystal Modes from Plasmonic Atomic Modes

that in the disconnected array case these atoms are not interacting and therefore there is no overlap between their orbitals. Similarly we could say that the establishment of physical contact is the equivalent of the creation of a *chemical bond* between neighboring plasmonic atoms. Therefore, the simultaneous establishment of electrical connections between all neighboring atoms together with the uniform spatial arrangement suddenly turns the considered structure into a plasmonic crystal. It is therefore not surprising to observe considerably different plasmonic modes in the two systems.

Given the so-far good analogy between gap-plasmon based systems and solid state systems, in this chapter we numerically investigate the broader applicability of these concepts by taking into considerations intermediate states between the already studied cases of the *plasmonic atom* and the *plasmonic crystal*. Therefore, we study finite groups of interacting (i.e. connected) plasmonic atoms of increasing number, equivalent to *plasmonic molecules*, following the evolution of their plasmonic resonances.

A.3 Methods

A.3.1 Numerical Modeling

Similarly to the case of atoms forming molecules and crystals, in the addition process we respected the spatial arrangement rules dictated by the final crystalline configuration. Moreover, we always simulated structures with a symmetry plane parallel to the illumination polarization so that the computational domain could be halved along such plane.

For simulating finite GP nanocavities we thus defined a large enough computational domain that we halved along the above-mentioned plane. We used a port boundary condition to excite the system with normal illumination and we first solved for the background field (excluding the front nanostructure). In a second step we re-activated the front nanostructure and computed the scattered as well as total fields. In this second computation perfectly matched layers (PMLs) surrounded the computational domain (apart from the symmetry plane).

A.3.2 Absorption Cross Section Computation

For each simulated structure we calculated the integral of the total dissipation term both in the finite structure and the continuous back reflector, P_{abs} . Knowing the incident power (imposed at the port boundary condition) as well as the total computational cell area we could compute the irradiation

intensity in each case ($I = P_{in}/A_{cell}$). Then, knowing the geometrical area of the plasmonic molecule, we could compute the power directly impinging on it as $P_{in} = I \cdot A_{molecule}$ and finally come to the absorption cross section calculation from $C_{abs} = P_{abs}/P_{in}$.

A.4 Results and Discussion

We simulated three different finite groups of connected gap plasmon nanocavities. The smallest one is the equivalent of an hexane molecule and consists of a loop of six connected nanocavities. Then we considered 4 loops, arranged according to the final array symmetry (hexagonal arrangement) and, finally, we considered 9 loops. In the graph in Figure A.1 we can compare the absorption spectra of these three systems with those of an isolated GP nanocavity and an infinity array of connected GP nanocavities.

We already saw in the previous chapters, that the isolated GP nanocavity is characterized by a dominant absorption peak around 870 nm which we indicated with 1 in the graph. While such peak is completely absent in the infinite array, we observe that the finite structures all present a defined absorption peak in the same wavelength range (peaks indicated with 1b-d). From the analysis of the normalized magnetic field amplitude (right column) we immediately notice a similarity between the nature of these modes. In particular, the field profile is dominated by a strong antinode beneath one of the peripheral nanocavities of the structure. Additional, weaker antinodes are visible along the *surface* of the considered structure. Moreover, upon increasing the structure size, the strength of this mode decreases, eventually vanishing. We can therefore consider this resonance mode like a plasmonic surface mode, which becomes weaker as the surface to volume ratio of the structure decreases and completely disappears for an infinite array.

At the other end of the spectrum, we find the absorption peak of the infinite array (indicated with 2). In the three GP nanocavities groups spectra we identify the corresponding peaks (2b-d). We observe that, as the structure complexity increases, this mode blue-shifts and strengthen compared to the surface mode peak. Once more, the magnetic field profiles (left column) clearly show the similar nature of these resonance peaks. In particular we can notice that the GP nanocavities located in the bulk of the structure present the characteristic three-node magnetic field profile. Therefore, as the structure grows the number of bulk element increases and the field assumes the characteristics of the infinite array.

A.5 Conclusions

To conclude, we have briefly shown that, finite groups of connected GP nanocavities present an intermediate behavior between the single, isolated nanocavity and the infinite array of nanocavities. In the studied intermediate states, we could identify a resonance with affinities to the isolated GP nanocavity which behaves as a surface mode, propagating along the peripheral elements of the structure. At the same time, as the number of elements increases, more contribution from the bulk, array-like mode causes the emergence of a peak which strengthen while blue-shifting. In the limit of the infinite array, no surface modes are possible and all the elements present the characteristic three-node structures. Consequently, the absorption spectrum presents only one mode.

A.5. Conclusions

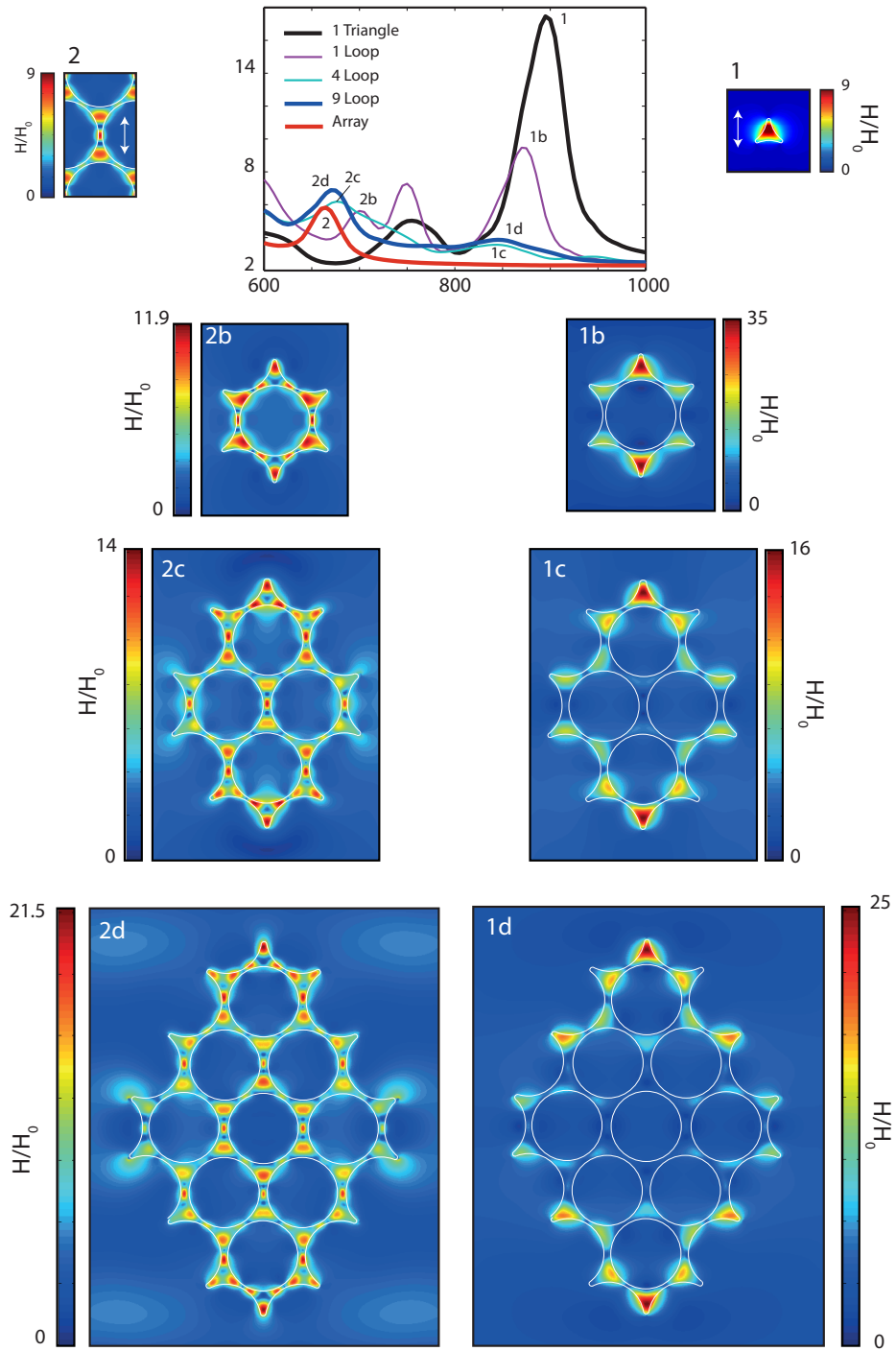


Figure A.1: Absorption Spectra of Different Plasmonic Molecules The graph shows the absorption spectra of the single GP atom (black curve), the GP crystal (red curve) and those of three GP molecules consisting of 1 loop of 6 atoms (purple curve), 4 loops (cyan curve) and 9 loops (blue curve). The two interesting resonance modes at long and short wavelengths are indicated with 1 and 2 respectively plus a letter to identify the structure for which it is considered. The color plots show the normalized magnitude of the magnetic field for the indicated resonances.

Bibliography

- [1] R. v. G. Albert Van Helden, Sven Dupr, *The Origin of the Telescope*. Royal Nethederlands Academy of Arts and Sciences, 2010.
- [2] C. K. Rosenthal, “Milestone 1 - the beginning,” *Nature Cell Biol.*, vol. 11, p. S6, 2009.
- [3] Various, “Nature milestone - light microscopy,” *Nature Cell Biol.*, vol. 11, pp. S1 – S22, 2009.
- [4] S. A. Maier, *Plasmonics Fundamentals and Applications*. Springer, 2007.
- [5] M. N. D. Ashcroft Neil W., *Solid State Physics*. Cengage Learning Emea, 2000.
- [6] S. I. Bozhevolnyi, *Plasmonic Nanoguides and Circuits*. Pan Stanford, 2009.
- [7] B. Prade, J. Y. Vinet, and A. Mysyrowicz, “Guided optical waves in planar heterostructures with negative dielectric constant,” *Phys. Rev. B*, vol. 44, pp. 13 556–13 572, Dec 1991. [Online]. Available: <http://link.aps.org/doi/10.1103/PhysRevB.44.13556>
- [8] H. Choo, M. K. Kim, M. Staffaroni, T. J. Seok, J. Bokor, S. Cabrini, P. J. Schuck, M. C. Wu, and E. Yablonovitch, “Nanofocusing in a metal-insulator-metal gap plasmon waveguide with a three-dimensional linear taper,” *Nature Photonics*, vol. 6, no. 12, pp. 837–843, Dec 2012, 048EC Times Cited:19 Cited References Count:41. [Online]. Available: [Go to ISI://WOS:000311892000013](#)
- [9] M. G. Nielsen, D. K. Gramotnev, A. Pors, O. Albrektsen, and S. I. Bozhevolnyi, “Continuous layer gap plasmon resonators,” *Optics Express*, vol. 19, no. 20, pp. 19 310–19 322, Sep 26 2011, 826SC Times Cited:8 Cited References Count:37. [Online]. Available: [Go to ISI://WOS:000295373800055](#)

Bibliography

- [10] A. Moreau, C. Ciraci, J. J. Mock, R. T. Hill, Q. Wang, B. J. Wiley, A. Chilkoti, and D. R. Smith, "Controlled-reflectance surfaces with film-coupled colloidal nanoantennas," *Nature*, vol. 492, no. 7427, pp. 86–+, Dec 6 2012, 048EQ Times Cited:29 Cited References Count:30. [Online]. Available: [iGo to ISI://WOS:000311893400050](#)
- [11] D. R. H. Craig F. Bohren, *Absorption and Scattering of Light by Small Particles*. Wiley, 1983.
- [12] N. J. Halas, S. Lal, W. S. Chang, S. Link, and P. Nordlander, "Plasmons in strongly coupled metallic nanostructures," *Chemical Reviews*, vol. 111, no. 6, pp. 3913–3961, Jun 2011, sp. Iss. SI 779CW Times Cited:459 Cited References Count:513. [Online]. Available: [iGo to ISI://WOS:000291756700008](#)
- [13] H. A. Atwater and A. Polman, "Plasmonics for improved photovoltaic devices," *Nature Materials*, vol. 9, no. 3, pp. 205–213, Mar 2010, 557WN Times Cited:1044 Cited References Count:92. [Online]. Available: [iGo to ISI://WOS:000274700900014](#)
- [14] J. V. van de Groep, P. Spinelli, and A. Polman, "Transparent conducting silver nanowire networks," *Nano Letters*, vol. 12, no. 6, pp. 3138–3144, Jun 2012, 956RI Times Cited:10 Cited References Count:38. [Online]. Available: [iGo to ISI://WOS:000305106400081](#)
- [15] C. H. Wu, B. Neuner, J. John, A. Milder, B. Zollars, S. Savoy, and G. Shvets, "Metamaterial-based integrated plasmonic absorber/emitter for solar thermo-photovoltaic systems," *Journal of Optics*, vol. 14, no. 2, Feb 2012, sp. Iss. SI 892RN Times Cited:17 Cited References Count:26. [Online]. Available: [iGo to ISI://WOS:000300303400006](#)
- [16] Y. J. Xiong, R. Long, D. Liu, X. L. Zhong, C. M. Wang, Z. Y. Li, and Y. Xie, "Solar energy conversion with tunable plasmonic nanostructures for thermoelectric devices," *Nanoscale*, vol. 4, no. 15, pp. 4416–4420, 2012, 973AS Times Cited:5 Cited References Count:18. [Online]. Available: [iGo to ISI://WOS:000306324000008](#)
- [17] S. Linic, P. Christopher, and D. B. Ingram, "Plasmonic-metal nanostructures for efficient conversion of solar to chemical energy," *Nature Materials*, vol. 10, no. 12, pp. 911–921, Dec 2011, 857CS Times Cited:263 Cited References Count:91. [Online]. Available: [iGo to ISI://WOS:000297692900014](#)

- [18] S. C. Warren and E. Thimsen, “Plasmonic solar water splitting,” *Energy & Environmental Science*, vol. 5, no. 1, pp. 5133–5146, Jan 2012, 875PX Times Cited:38 Cited References Count:74. [Online]. Available: [iGo to ISI://WOS:000299046100003](#)
- [19] M. W. Knight, H. Sobhani, P. Nordlander, and N. J. Halas, “Photodetection with active optical antennas,” *Science*, vol. 332, no. 6030, pp. 702–704, May 6 2011, 759RK Times Cited:115 Cited References Count:30. [Online]. Available: [iGo to ISI://WOS:000290265800038](#)
- [20] F. M. Wang and N. A. Melosh, “Plasmonic energy collection through hot carrier extraction,” *Nano Letters*, vol. 11, no. 12, pp. 5426–5430, Dec 2011, 860LQ Times Cited:12 Cited References Count:26. [Online]. Available: [iGo to ISI://WOS:000297950200056](#)
- [21] D. Kraemer, B. Poudel, H. P. Feng, J. C. Caylor, B. Yu, X. Yan, Y. Ma, X. W. Wang, D. Z. Wang, A. Muto, K. McEnaney, M. Chiesa, Z. F. Ren, and G. Chen, “High-performance flat-panel solar thermoelectric generators with high thermal concentration,” *Nature Materials*, vol. 10, no. 7, pp. 532–538, Jul 2011, 781WV Times Cited:101 Cited References Count:41. [Online]. Available: [iGo to ISI://WOS:000291969500019](#)
- [22] M. K. Hedayati, M. Javaherirahim, B. Mozooni, R. Abdelaziz, A. Tavassolizadeh, V. S. K. Chakravadhanula, V. Zaporozhchenko, T. Strunkus, F. Faupel, and M. Elbahri, “Design of a perfect black absorber at visible frequencies using plasmonic metamaterials,” *Advanced Materials*, vol. 23, no. 45, pp. 5410–+, Dec 1 2011, 853WZ Times Cited:21 Cited References Count:26. [Online]. Available: [iGo to ISI://WOS:000297457700013](#)
- [23] M. Elbahri, S. Homaeigohar, R. Abdelaziz, T. Dai, R. Khalil, and A. U. Zillohu, “Smart metal-polymer bionanocomposites as omnidirectional plasmonic black absorber formed by nanofluid filtration,” *Advanced Functional Materials*, vol. 22, no. 22, pp. 4771–4777, Nov 21 2012, 035RU Times Cited:1 Cited References Count:57. [Online]. Available: [iGo to ISI://WOS:000310966500014](#)
- [24] A. De Luca, N. Depalo, E. Fanizza, M. Striccoli, M. L. Curri, M. Infusino, A. R. Rashed, M. La Deda, and G. Strangi, “Plasmon mediated super-absorber flexible nanocomposites for metamaterials,” *Nanoscale*, vol. 5, no. 13, pp. 6097–105, Jul 7 2013, de Luca, Antonio Depalo, Nicoletta Fanizza, Elisabetta Striccoli, Marinella

Bibliography

- Curri, M Lucia Infusino, Melissa Rashed, Alireza R La Deda, Massimo Strangi, Giuseppe eng England 2013/06/01 06:00 Nanoscale. 2013 Jul 7;5(13):6097-105. doi: 10.1039/c3nr00988b. Epub 2013 May 30. [Online]. Available: <http://www.ncbi.nlm.nih.gov/pubmed/23722253>
- [25] K. Aydin, V. E. Ferry, R. M. Briggs, and H. A. Atwater, “Broadband polarization-independent resonant light absorption using ultrathin plasmonic super absorbers,” *Nature Communications*, vol. 2, Nov 2011, 857AQ Times Cited:58 Cited References Count:28. [Online]. Available: [iGo to ISI://WOS:000297686500004](#)
- [26] M. G. Nielsen, A. Pors, O. Albrektsen, and S. I. Bozhevolnyi, “Efficient absorption of visible radiation by gap plasmon resonators,” *Optics Express*, vol. 20, no. 12, pp. 13 311–13 319, Jun 4 2012, 961KP Times Cited:7 Cited References Count:28. [Online]. Available: [iGo to ISI://WOS:000305463600068](#)
- [27] E. E. Narimanov and A. V. Kildishev, “Optical black hole: Broadband omnidirectional light absorber,” *Applied Physics Letters*, vol. 95, no. 4, Jul 27 2009, 478TT Times Cited:107 Cited References Count:13. [Online]. Available: [iGo to ISI://WOS:000268611900006](#)
- [28] A. Aubry, D. Y. Lei, A. I. Fernandez-Dominguez, Y. Sonnefraud, S. A. Maier, and J. B. Pendry, “Plasmonic light-harvesting devices over the whole visible spectrum,” *Nano Letters*, vol. 10, no. 7, pp. 2574–2579, Jul 2010, 632IP Times Cited:89 Cited References Count:34. [Online]. Available: [iGo to ISI://WOS:000280416200047](#)
- [29] J. B. Pendry, A. Aubry, D. R. Smith, and S. A. Maier, “Transformation optics and subwavelength control of light,” *Science*, vol. 337, no. 6094, pp. 549–552, Aug 3 2012, 982PU Times Cited:9 Cited References Count:38. [Online]. Available: [iGo to ISI://WOS:000307058700035](#)
- [30] T. Sondergaard, S. M. Novikov, T. Holmgaard, R. L. Eriksen, J. Beermann, Z. H. Han, K. Pedersen, and S. I. Bozhevolnyi, “Plasmonic black gold by adiabatic nanofocusing and absorption of light in ultra-sharp convex grooves,” *Nature Communications*, vol. 3, Jul 2012, 981UA Times Cited:6 Cited References Count:34. [Online]. Available: [iGo to ISI://WOS:000306995000041](#)
- [31] T. Sondergaard and S. I. Bozhevolnyi, “Theoretical analysis of plasmonic black gold: periodic arrays of ultra-sharp grooves,” *New Journal of Physics*, vol. 15, Jan 17 2013, 071TJ Times

- Cited:0 Cited References Count:34. [Online]. Available: [Go to ISI://WOS:000313617000001](#)
- [32] J. C. Hulteen and R. P. Van Duyne, “Nanosphere lithography - a materials general fabrication process for periodic particle array surfaces,” *Journal of Vacuum Science & Technology a-Vacuum Surfaces and Films*, vol. 13, no. 3, pp. 1553–1558, May-Jun 1995, 2 Rd767 Times Cited:775 Cited References Count:32. [Online]. Available: [Go to ISI://WOS:A1995RD76700063](#)
- [33] B. J. Y. Tan, C. H. Sow, T. S. Koh, K. C. Chin, A. T. S. Wee, and C. K. Ong, “Fabrication of size-tunable gold nanoparticles array with nanosphere lithography, reactive ion etching, and thermal annealing,” *Journal of Physical Chemistry B*, vol. 109, no. 22, pp. 11 100–11 109, Jun 9 2005, 932YC Times Cited:65 Cited References Count:38. [Online]. Available: [Go to ISI://WOS:000229589700005](#)
- [34] X. Y. Zhang, A. V. Whitney, J. Zhao, E. M. Hicks, and R. P. Van Duyne, “Advances in contemporary nanosphere lithographic techniques,” *Journal of Nanoscience and Nanotechnology*, vol. 6, no. 7, pp. 1920–1934, Jul 2006, 070SA Times Cited:50 Cited References Count:114. [Online]. Available: [Go to ISI://WOS:000239542900004](#)
- [35] S. R. Ye, A. L. Routzahn, and R. L. Carroll, “Fabrication of 3d metal dot arrays by geometrically structured dynamic shadowing lithography,” *Langmuir*, vol. 27, no. 22, pp. 13 806–13 812, Nov 15 2011, 842KM Times Cited:4 Cited References Count:83. [Online]. Available: [Go to ISI://WOS:000296598300050](#)
- [36] E. D. Palik, “Handbook of optical-constants,” *Journal of the Optical Society of America a-Optics Image Science and Vision*, vol. 1, no. 12, pp. 1297–1297, 1984, tx574 Times Cited:23 Cited References Count:0. [Online]. Available: [Go to ISI://WOS:A1984TX57400387](#)
- [37] N. Liu, M. Mesch, T. Weiss, M. Hentschel, and H. Giessen, “Infrared perfect absorber and its application as plasmonic sensor,” *Nano Letters*, vol. 10, no. 7, pp. 2342–2348, Jul 2010, 632IP Times Cited:196 Cited References Count:43. [Online]. Available: [Go to ISI://WOS:000280416200009](#)
- [38] Y. Z. Chu and K. B. Crozier, “Experimental study of the interaction between localized and propagating surface plasmons,” *Optics Letters*, vol. 34, no. 3, pp. 244–246, Feb 1 2009, 412WV

Bibliography

- Times Cited:48 Cited References Count:11. [Online]. Available: [Go to ISI://WOS:000263755800007](#)
- [39] W. Rechberger, A. Hohenau, A. Leitner, J. R. Krenn, B. Lamprecht, and F. R. Aussenegg, "Optical properties of two interacting gold nanoparticles," *Optics Communications*, vol. 220, no. 1-3, pp. 137–141, May 1 2003, 676LJ Times Cited:644 Cited References Count:14. [Online]. Available: [Go to ISI://WOS:000182753300017](#)
- [40] K. L. Kelly, E. Coronado, L. L. Zhao, and G. C. Schatz, "The optical properties of metal nanoparticles: The influence of size, shape, and dielectric environment," *Journal of Physical Chemistry B*, vol. 107, no. 3, pp. 668–677, Jan 23 2003, 638AE Times Cited:2826 Cited References Count:64. [Online]. Available: [Go to ISI://WOS:000180545300005](#)
- [41] Y. Luo, J. B. Pendry, and A. Aubry, "Surface plasmons and singularities," *Nano Letters*, vol. 10, no. 10, pp. 4186–4191, Oct 2010, 661KQ Times Cited:31 Cited References Count:26. [Online]. Available: [Go to ISI://WOS:000282727600065](#)
- [42] C. C. Ho, P. Y. Chen, K. H. Lin, W. T. Juan, and W. L. Lee, "Fabrication of monolayer of polymer/nanospheres hybrid at a water-air interface," *Acs Applied Materials & Interfaces*, vol. 3, no. 2, pp. 204–208, Feb 2011, 725IW Times Cited:8 Cited References Count:28. [Online]. Available: [Go to ISI://WOS:000287639400017](#)
- [43] G. D. Moon, T. I. Lee, B. Kim, G. Chae, J. Kim, S. Kim, J. M. Myoung, and U. Jeong, "Assembled monolayers of hydrophilic particles on water surfaces," *Acs Nano*, vol. 5, no. 11, pp. 8600–8612, Nov 2011, 849RR Times Cited:8 Cited References Count:53. [Online]. Available: [Go to ISI://WOS:000297143300017](#)
- [44] J. S. Donner, G. Baffou, D. McCloskey, and R. Quidant, "Plasmon-assisted optofluidics," *Acs Nano*, vol. 5, no. 7, pp. 5457–5462, Jul 2011, 796ES Times Cited:33 Cited References Count:18. [Online]. Available: [Go to ISI://WOS:000293035200021](#)
- [45] K. Moth-Poulsen, D. Coso, K. Borjesson, N. Vinokurov, S. K. Meier, A. Majumdar, K. P. C. Vollhardt, and R. A. Segalman, "Molecular solar thermal (most) energy storage and release system," *Energy & Environmental Science*, vol. 5, no. 9, pp. 8534–8537, Sep 2012, 989XQ

- Times Cited:2 Cited References Count:28. [Online]. Available: [iGo to ISI://WOS:000307595000010](#)
- [46] C. Fasciani, C. J. B. Alejo, M. Grenier, J. C. Netto-Ferreira, and J. C. Scaiano, “High-temperature organic reactions at room temperature using plasmon excitation: Decomposition of dicumyl peroxide,” *Organic Letters*, vol. 13, no. 2, pp. 204–207, Jan 21 2011, 705LN Times Cited:15 Cited References Count:19. [Online]. Available: [iGo to ISI://WOS:000286130000009](#)
- [47] R. Alaei, C. Menzel, U. Huebner, E. Pshenay-Severin, S. Bin Hasan, T. Pertsch, C. Rockstuhl, and F. Lederer, “Deep-subwavelength plasmonic nanoresonators exploiting extreme coupling,” *Nano Letters*, vol. 13, no. 8, pp. 3482–3486, Aug 2013, 202SX Times Cited:1 Cited References Count:39. [Online]. Available: [iGo to ISI://WOS:000323241000006](#)
- [48] G. Tagliabue, H. Eghlidi, and D. Poulidakos, “Facile multifunctional plasmonic sunlight harvesting with tapered triangle nanopatterning of thin films,” *Nanoscale*, vol. 5, no. 20, pp. 9957–9962, 2013, 226AC Times Cited:0 Cited References Count:35. [Online]. Available: [iGo to ISI://WOS:000325005500069](#)
- [49] J. M. Hao, L. Zhou, and M. Qiu, “Nearly total absorption of light and heat generation by plasmonic metamaterials,” *Physical Review B*, vol. 83, no. 16, Apr 13 2011, 749ST Times Cited:62 Cited References Count:59. [Online]. Available: [iGo to ISI://WOS:000289490500004](#)
- [50] B. Kante, Y. S. Park, K. O’Brien, D. Shuldman, N. D. Lanzillotti-Kimura, Z. J. Wong, X. B. Yin, and X. Zhang, “Symmetry breaking and optical negative index of closed nanorings,” *Nature Communications*, vol. 3, 2012, 104KP Times Cited:4 Cited References Count:37. [Online]. Available: [iGo to ISI://WOS:000315992100017](#)
- [51] A. Pors, O. Albrechtsen, I. P. Radko, and S. I. Bozhevolnyi, “Gap plasmon-based metasurfaces for total control of reflected light,” *Scientific Reports*, vol. 3, Jul 8 2013, 178EA Times Cited:2 Cited References Count:28. [Online]. Available: [iGo to ISI://WOS:000321425700003](#)
- [52] A. Cattoni, P. Ghenuche, A. M. Haghiri-Gosnet, D. Decanini, J. Chen, J. L. Pelouard, and S. Collin, “ $\lambda(3)/1000$ plasmonic nanocavities for biosensing fabricated by soft uv nanoimprint lithography,” *Nano*

Bibliography

- Letters*, vol. 11, no. 9, pp. 3557–3563, Sep 2011, 818XO Times Cited:28 Cited References Count:43. [Online]. Available: [iGo to ISI://WOS:000294790200008](#)
- [53] M. Kuttge, F. J. G. de Abajo, and A. Polman, “Ultrasmall mode volume plasmonic nanodisk resonators,” *Nano Letters*, vol. 10, no. 5, pp. 1537–1541, May 2010, 593HX Times Cited:43 Cited References Count:24. [Online]. Available: [iGo to ISI://WOS:000277444900002](#)
- [54] O. Perez-Gonzalez, N. Zabala, A. G. Borisov, N. J. Halas, P. Nordlander, and J. Aizpurua, “Optical spectroscopy of conductive junctions in plasmonic cavities,” *Nano Letters*, vol. 10, no. 8, pp. 3090–3095, Aug 2010, 636JO Times Cited:51 Cited References Count:32. [Online]. Available: [iGo to ISI://WOS:000280728900060](#)
- [55] I. Romero, J. Aizpurua, G. W. Bryant, and F. J. G. de Abajo, “Plasmons in nearly touching metallic nanoparticles: singular response in the limit of touching dimers,” *Optics Express*, vol. 14, no. 21, pp. 9988–9999, Oct 16 2006, 098JS Times Cited:305 Cited References Count:44. [Online]. Available: [iGo to ISI://WOS:000241517400051](#)
- [56] Y. M. Wang, Z. W. Li, K. Zhao, A. Sobhani, X. Zhu, Z. Y. Fang, and N. J. Halas, “Substrate-mediated charge transfer plasmons in simple and complex nanoparticle clusters,” *Nanoscale*, vol. 5, no. 20, pp. 9897–9901, 2013, 226AC Times Cited:1 Cited References Count:37. [Online]. Available: [iGo to ISI://WOS:000325005500061](#)
- [57] W. A. Murray, S. Astilean, and W. L. Barnes, “Transition from localized surface plasmon resonance to extended surface plasmon-polariton as metallic nanoparticles merge to form a periodic hole array,” *Physical Review B*, vol. 69, no. 16, Apr 2004, 820YW Times Cited:71 Cited References Count:26. [Online]. Available: [iGo to ISI://WOS:000221427100084](#)
- [58] S. Palomba, S. Zhang, Y. Park, G. Bartal, X. B. Yin, and X. Zhang, “Optical negative refraction by four-wave mixing in thin metallic nanostructures,” *Nature Materials*, vol. 11, no. 1, pp. 34–38, 2012, 866TK Times Cited:17 Cited References Count:25. [Online]. Available: [iGo to ISI://WOS:000298406500017](#)
- [59] V. E. Bochenkov and D. S. Sutherland, “From rings to crescents: A novel fabrication technique uncovers the transition details,” *Nano Letters*, vol. 13, no. 3, pp. 1216–1220, Mar 2013, 107TN Times

- Cited:3 Cited References Count:30. [Online]. Available: [Go to ISI://WOS:000316243800055](#)
- [60] P. B. Johnson and R. W. Christy, “Optical constants of noble metals,” *Physical Review B*, vol. 6, no. 12, pp. 4370–4379, 1972, o3462 Times Cited:6396 Cited References Count:42. [Online]. Available: [Go to ISI://WOS:A1972O346200002](#)
- [61] A. Wiener, H. G. Duan, M. Bosman, A. P. Horsfield, J. B. Pendry, J. K. W. Yang, S. A. Maier, and A. I. Fernandez-Dominguez, “Electron-energy loss study of nonlocal effects in connected plasmonic nanoprisms,” *Acs Nano*, vol. 7, no. 7, pp. 6287–6296, Jul 2013, 191MO Times Cited:4 Cited References Count:59. [Online]. Available: [Go to ISI://WOS:000322417400075](#)
- [62] T. Atay, J. H. Song, and A. V. Nurmikko, “Strongly interacting plasmon nanoparticle pairs: From dipole-dipole interaction to conductively coupled regime,” *Nano Letters*, vol. 4, no. 9, pp. 1627–1631, Sep 2004, 853OP Times Cited:322 Cited References Count:14. [Online]. Available: [Go to ISI://WOS:000223837200011](#)
- [63] E. Moreno, F. J. Garcia-Vidal, S. G. Rodrigo, L. Martin-Moreno, and S. I. Bozhevolnyi, “Channel plasmon-polaritons: modal shape, dispersion, and losses,” *Optics Letters*, vol. 31, no. 23, pp. 3447–3449, Dec 1 2006, 106LR Times Cited:104 Cited References Count:14. [Online]. Available: [Go to ISI://WOS:000242102500015](#)
- [64] S. W. Qu and Z. P. Nie, “Plasmonic nanopatch array for optical integrated circuit applications,” *Scientific Reports*, vol. 3, 2013, 248GF Times Cited:0 Cited References Count:40. [Online]. Available: [Go to ISI://WOS:000326683700002](#)
- [65] O. Hess, J. B. Pendry, S. A. Maier, R. F. Oulton, J. M. Hamm, and K. L. Tsakmakidis, “Active nanoplasmonic metamaterials,” *Nature Materials*, vol. 11, no. 7, pp. 573–584, Jul 2012, 963QR Times Cited:51 Cited References Count:103. [Online]. Available: [Go to ISI://WOS:000305638600008](#)
- [66] J. Yang, C. Sauvan, H. T. Liu, and P. Lalanne, “Theory of fishnet negative-index optical metamaterials,” *Physical Review Letters*, vol. 107, no. 4, Jul 19 2011, 794CI Times Cited:25 Cited References Count:24. [Online]. Available: [Go to ISI://WOS:000292872600002](#)

Bibliography

- [67] Y. C. Jun, R. D. Kekatpure, J. S. White, and M. L. Brongersma, “Nonresonant enhancement of spontaneous emission in metal-dielectric-metal plasmon waveguide structures,” *Physical Review B*, vol. 78, no. 15, Oct 2008, 367TB Times Cited:70 Cited References Count:22. [Online]. Available: [Go to ISI://WOS:000260574400012](#)
- [68] S. A. Maier, P. G. Kik, H. A. Atwater, S. Meltzer, E. Harel, B. E. Koel, and A. A. G. Requicha, “Local detection of electromagnetic energy transport below the diffraction limit in metal nanoparticle plasmon waveguides,” *Nature Materials*, vol. 2, no. 4, pp. 229–232, Apr 2003, 664GE Times Cited:1241 Cited References Count:17. [Online]. Available: [Go to ISI://WOS:000182052700018](#)
- [69] M. I. Stockman, “Nanofocusing of optical energy in tapered plasmonic waveguides,” *Physical Review Letters*, vol. 93, no. 13, Sep 24 2004, 857PS Times Cited:513 Cited References Count:26. [Online]. Available: [Go to ISI://WOS:000224131400076](#)
- [70] D. K. Gramotnev and S. I. Bozhevolnyi, “Nanofocusing of electromagnetic radiation,” *Nature Photonics*, vol. 8, no. 1, pp. 14–23, Jan 2014, 280JL Times Cited:0 Cited References Count:91. [Online]. Available: [Go to ISI://WOS:000329025000008](#)
- [71] V. S. Volkov, S. I. Bozhevolnyi, S. G. Rodrigo, L. Martin-Moreno, F. J. Garcia-Vidal, E. Devaux, and T. W. Ebbesen, “Nanofocusing with channel plasmon polaritons,” *Nano Letters*, vol. 9, no. 3, pp. 1278–1282, Mar 2009, 418IO Times Cited:68 Cited References Count:26. [Online]. Available: [Go to ISI://WOS:000264142100062](#)
- [72] F. van Beijnum, P. J. van Veldhoven, E. J. Geluk, M. J. A. de Dood, G. W. 't Hooft, and M. P. van Exter, “Surface plasmon lasing observed in metal hole arrays,” *Physical Review Letters*, vol. 110, no. 20, May 13 2013, 146AX Times Cited:3 Cited References Count:34. [Online]. Available: [Go to ISI://WOS:000319062300020](#)
- [73] D. F. P. Pile, T. Ogawa, D. K. Gramotnev, Y. Matsuzaki, K. C. Vernon, K. Yamaguchi, T. Okamoto, M. Haraguchi, and M. Fukui, “Two-dimensionally localized modes of a nanoscale gap plasmon waveguide,” *Applied Physics Letters*, vol. 87, no. 26, Dec 26 2005, 998SD Times Cited:137 Cited References Count:19. [Online]. Available: [Go to ISI://WOS:000234338700014](#)

- [74] R. F. Oulton, V. J. Sorger, D. A. Genov, D. F. P. Pile, and X. Zhang, “A hybrid plasmonic waveguide for subwavelength confinement and long-range propagation,” *Nature Photonics*, vol. 2, no. 8, pp. 496–500, Aug 2008, 337CS Times Cited:474 Cited References Count:30. [Online]. Available: [Go to ISI://WOS:000258413700015](#)
- [75] G. Baffou and R. Quidant, “Thermo-plasmonics: using metallic nanostructures as nano-sources of heat,” *Laser & Photonics Reviews*, vol. 7, no. 2, pp. 171–187, Mar 2013, 238HD Times Cited:22 Cited References Count:139. [Online]. Available: [Go to ISI://WOS:000325934300004](#)
- [76] Z. Y. Fang, Y. R. Zhen, O. Neumann, A. Polman, F. J. G. de Abajo, P. Nordlander, and N. J. Halas, “Evolution of light-induced vapor generation at a liquid-immersed metallic nanoparticle,” *Nano Letters*, vol. 13, no. 4, pp. 1736–1742, Apr 2013, 125OO Times Cited:8 Cited References Count:32. [Online]. Available: [Go to ISI://WOS:000317549300060](#)
- [77] O. Neumann, A. S. Urban, J. Day, S. Lal, P. Nordlander, and N. J. Halas, “Solar vapor generation enabled by nanoparticles,” *Acs Nano*, vol. 7, no. 1, pp. 42–49, Jan 2013, 078FB Times Cited:23 Cited References Count:33. [Online]. Available: [Go to ISI://WOS:000314082800008](#)
- [78] F. Yi, H. Zhu, J. C. Reed, and E. Cubukcu, “Plasmonically enhanced thermomechanical detection of infrared radiation,” *Nano Letters*, vol. 13, no. 4, pp. 1638–1643, 2013. [Online]. Available: <http://pubs.acs.org/doi/abs/10.1021/nl400087b>
- [79] A. O. Govorov, W. Zhang, T. Skeini, H. Richardson, J. Lee, and N. A. Kotov, “Gold nanoparticle ensembles as heaters and actuators: melting and collective plasmon resonances,” *Nanoscale Research Letters*, vol. 1, no. 1, pp. 84–90, Jun 2006, v44ao Times Cited:125 Cited References Count:17. [Online]. Available: [Go to ISI://WOS:000202975800011](#)
- [80] H. H. Richardson, M. T. Carlson, P. J. Tandler, P. Hernandez, and A. O. Govorov, “Experimental and theoretical studies of light-to-heat conversion and collective heating effects in metal nanoparticle solutions,” *Nano Letters*, vol. 9, no. 3, pp. 1139–1146, Mar 2009, 418IO Times Cited:110 Cited References Count:56. [Online]. Available: [Go to ISI://WOS:000264142100039](#)

Bibliography

- [81] G. Baffou, P. Berto, E. B. Urena, R. Quidant, S. Monneret, J. Polleux, and H. Rigneault, “Photoinduced heating of nanoparticle arrays,” *Acs Nano*, vol. 7, no. 8, pp. 6478–6488, Aug 2013, 210DX Times Cited:0 Cited References Count:38. [Online]. Available: [iGo to ISI://WOS:000323810600006](#)
- [82] K. Setoura, Y. Okada, D. Werner, and S. Hashimoto, “Observation of nanoscale cooling effects by substrates and the surrounding media for single gold nanoparticles under cw-laser illumination,” *Acs Nano*, vol. 7, no. 9, pp. 7874–7885, Sep 2013, 294BH Times Cited:0 Cited References Count:37. [Online]. Available: [iGo to ISI://WOS:000330016900047](#)
- [83] FLIR, “Photometry form.”
- [84] Campanar.P and T. Ricolfi, “New determination of total normal emissivity of cylindrical and conical cavities,” *Journal of the Optical Society of America*, vol. 57, no. 1, pp. 48–&, 1967, 89456 Times Cited:13 Cited References Count:12. [Online]. Available: [iGo to ISI://WOS:A19678945600009](#)
- [85] D. S. Minkina W., *Infrared Thermography: Error and Uncertainties*. Wiley, 2009.
- [86] D. Legaie, H. Pron, C. Bissieux, and V. Blain, “Thermographic application of black coatings on metals,” 2008.
- [87] A. D. Rakic, A. B. Djurisic, J. M. Elazar, and M. L. Majewski, “Optical properties of metallic films for vertical-cavity optoelectronic devices,” *Applied Optics*, vol. 37, no. 22, pp. 5271–5283, 1998, 106AJ Times Cited:673 Cited References Count:77. [Online]. Available: [iGo to ISI://WOS:000075107300033](#)
- [88] M. Rubin, “Optical-properties of soda lime silica glasses,” *Solar Energy Materials*, vol. 12, no. 4, pp. 275–288, 1985, ara34 Times Cited:114 Cited References Count:23. [Online]. Available: [iGo to ISI://WOS:A1985ARA3400003](#)
- [89] A. Fujishima and K. Honda, “Electrochemical photolysis of water at a semiconductor electrode,” *Nature*, vol. 238, no. 5358, pp. 37–+, 1972, m8526 Times Cited:7717 Cited References Count:5. [Online]. Available: [iGo to ISI://WOS:A1972M852600031](#)

- [90] T. Inoue, A. Fujishima, S. Konishi, and K. Honda, "Photoelectrocatalytic reduction of carbon-dioxide in aqueous suspensions of semiconductor powders," *Nature*, vol. 277, no. 5698, pp. 637–638, 1979, gj894 Times Cited:579 Cited References Count:13. [Online]. Available: [;Go to ISI://WOS:A1979GJ89400035](http://go ISI://WOS:A1979GJ89400035)
- [91] K. Hashimoto, H. Irie, and A. Fujishima, "TiO₂ photocatalysis: A historical overview and future prospects," *Japanese Journal of Applied Physics Part 1-Regular Papers Brief Communications & Review Papers*, vol. 44, no. 12, pp. 8269–8285, Dec 2005, 997CY Times Cited:671 Cited References Count:81. [Online]. Available: [;Go to ISI://WOS:000234223800003](http://go ISI://WOS:000234223800003)
- [92] R. Asahi, T. Morikawa, T. Ohwaki, K. Aoki, and Y. Taga, "Visible-light photocatalysis in nitrogen-doped titanium oxides," *Science*, vol. 293, no. 5528, pp. 269–271, Jul 13 2001, 452TK Times Cited:5008 Cited References Count:24. [Online]. Available: [;Go to ISI://WOS:000169875200049](http://go ISI://WOS:000169875200049)
- [93] B. Oregan and M. Gratzel, "A low-cost, high-efficiency solar-cell based on dye-sensitized colloidal TiO₂ films," *Nature*, vol. 353, no. 6346, pp. 737–740, Oct 24 1991, gl696 Times Cited:11568 Cited References Count:19. [Online]. Available: [;Go to ISI://WOS:A1991GL69600062](http://go ISI://WOS:A1991GL69600062)
- [94] M. Gratzel, "Photoelectrochemical cells," *Nature*, vol. 414, no. 6861, pp. 338–344, Nov 15 2001, 492CM Times Cited:4710 Cited References Count:49. [Online]. Available: [;Go to ISI://WOS:000172150700053](http://go ISI://WOS:000172150700053)
- [95] <http://nanocomposix.com/products>.
- [96] K. R. Catchpole and A. Polman, "Plasmonic solar cells," *Optics Express*, vol. 16, no. 26, pp. 21 793–21 800, Dec 22 2008, 390YX Times Cited:404 Cited References Count:40. [Online]. Available: [;Go to ISI://WOS:000262200700067](http://go ISI://WOS:000262200700067)
- [97] D. Duche, P. Torchio, L. Escoubas, F. Monestier, J. J. Simon, F. Flory, and G. Mathian, "Improving light absorption in organic solar cells by plasmonic contribution," *Solar Energy Materials and Solar Cells*, vol. 93, no. 8, pp. 1377–1382, Aug 2009, 465HQ Times Cited:81 Cited References Count:17. [Online]. Available: [;Go to ISI://WOS:000267573800028](http://go ISI://WOS:000267573800028)

Bibliography

- [98] M. D. Brown, T. Suteewong, R. S. S. Kumar, V. D’Innocenzo, A. Petrozza, M. M. Lee, U. Wiesner, and H. J. Snaith, “Plasmonic dye-sensitized solar cells using core-shell metal-insulator nanoparticles,” *Nano Letters*, vol. 11, no. 2, pp. 438–445, Feb 2011, 717LZ Times Cited:110 Cited References Count:38. [Online]. Available: [Go to ISI://WOS:000287049100023](#)
- [99] L. M. Peter, “The gratzel cell: Where next?” *Journal of Physical Chemistry Letters*, vol. 2, no. 15, pp. 1861–1867, Aug 4 2011, 801EL Times Cited:89 Cited References Count:62. [Online]. Available: [Go to ISI://WOS:000293419600004](#)
- [100] Y. Nishijima, K. Ueno, Y. Yokota, K. Murakoshi, and H. Misawa, “Plasmon-assisted photocurrent generation from visible to near-infrared wavelength using a au-nanorods/tio2 electrode,” *Journal of Physical Chemistry Letters*, vol. 1, no. 13, pp. 2031–2036, Jul 1 2010, 620OC Times Cited:94 Cited References Count:30. [Online]. Available: [Go to ISI://WOS:000279508200024](#)
- [101] Y. Tian and T. Tatsuma, “Mechanisms and applications of plasmon-induced charge separation at tio2 films loaded with gold nanoparticles,” *Journal of the American Chemical Society*, vol. 127, no. 20, pp. 7632–7637, May 25 2005, 928AX Times Cited:457 Cited References Count:30. [Online]. Available: [Go to ISI://WOS:000229244600070](#)
- [102] S. Wooh, Y. G. Lee, M. N. Tahir, D. Song, M. Meister, F. Laquai, W. Tremel, J. Bisquert, Y. S. Kang, and K. Char, “Plasmon-enhanced photocurrent in quasi-solid-state dye-sensitized solar cells by the inclusion of gold/silica core-shell nanoparticles in a tio2 photoanode,” *Journal of Materials Chemistry A*, vol. 1, no. 40, pp. 12 627–12 634, 2013, 231JZ Times Cited:1 Cited References Count:33. [Online]. Available: [Go to ISI://WOS:000325414000033](#)
- [103] P. Christopher, H. L. Xin, and S. Linic, “Visible-light-enhanced catalytic oxidation reactions on plasmonic silver nanostructures,” *Nature Chemistry*, vol. 3, no. 6, pp. 467–472, Jun 2011, 767HP Times Cited:107 Cited References Count:55. [Online]. Available: [Go to ISI://WOS:000290846300014](#)
- [104] D. Tsukamoto, Y. Shiraishi, Y. Sugano, S. Ichikawa, S. Tanaka, and T. Hirai, “Gold nanoparticles located at the interface of anatase/rutile tio2 particles as active plasmonic photocatalysts for aerobic oxidation,” *Journal of the American Chemical Society*, vol. 134, no. 14, pp.

- 6309–6315, Apr 11 2012, 922CQ Times Cited:69 Cited References Count:41. [Online]. Available: [iGo to ISI://WOS:000302524800040](#)
- [105] P. Christopher, H. L. Xin, A. Marimuthu, and S. Linic, “Singular characteristics and unique chemical bond activation mechanisms of photocatalytic reactions on plasmonic nanostructures,” *Nature Materials*, vol. 11, no. 12, pp. 1044–1050, Dec 2012, 041WO Times Cited:23 Cited References Count:50. [Online]. Available: [iGo to ISI://WOS:000311432600023](#)
- [106] W. B. Hou and S. B. Cronin, “A review of surface plasmon resonance-enhanced photocatalysis,” *Advanced Functional Materials*, vol. 23, no. 13, pp. 1612–1619, Apr 5 2013, 118IM Times Cited:15 Cited References Count:106. [Online]. Available: [iGo to ISI://WOS:000317019100002](#)
- [107] Z. H. Zhang, L. B. Zhang, M. N. Hedhili, H. N. Zhang, and P. Wang, “Plasmonic gold nanocrystals coupled with photonic crystal seamlessly on tio2 nanotube photoelectrodes for efficient visible light photoelectrochemical water splitting,” *Nano Letters*, vol. 13, no. 1, pp. 14–20, Jan 2013, 065IP Times Cited:22 Cited References Count:48. [Online]. Available: [iGo to ISI://WOS:000313142300003](#)
- [108] M. D. Xiao, R. B. Jiang, F. Wang, C. H. Fang, J. F. Wang, and J. C. Yu, “Plasmon-enhanced chemical reactions,” *Journal of Materials Chemistry A*, vol. 1, no. 19, pp. 5790–5805, 2013, 130RF Times Cited:4 Cited References Count:190. [Online]. Available: [iGo to ISI://WOS:000317936000001](#)
- [109] T. Ming, J. Suntivich, K. J. May, K. A. Stoerzinger, D. H. Kim, and Y. Shao-Horn, “Visible light photo-oxidation in au nanoparticle sensitized srtio3:nb photoanode,” *Journal of Physical Chemistry C*, vol. 117, no. 30, pp. 15 532–15 539, Aug 1 2013, 196WG Times Cited:1 Cited References Count:57. [Online]. Available: [iGo to ISI://WOS:000322807500009](#)
- [110] X. Li, X. N. Fu, and H. Yang, “Preparation and photocatalytic activity of eccentric au-titania core-shell nanoparticles by block copolymer templates,” *Physical Chemistry Chemical Physics*, vol. 13, no. 7, pp. 2809–2814, 2011, 715NF Times Cited:6 Cited References Count:76. [Online]. Available: [iGo to ISI://WOS:000286890500043](#)

Bibliography

- [111] Z. W. Seh, S. H. Liu, S. Y. Zhang, M. S. Bharathi, H. Ramanarayan, M. Low, K. W. Shah, Y. W. Zhang, and M. Y. Han, "Anisotropic growth of titania onto various gold nanostructures: Synthesis, theoretical understanding, and optimization for catalysis," *Angewandte Chemie-International Edition*, vol. 50, no. 43, pp. 10 140–10 143, 2011, 838GF Times Cited:18 Cited References Count:57. [Online]. Available: [iGo to ISI://WOS:000296274700013](#)
- [112] M. V. U. Kriebig, *Optical Properties of Metal Clusters*. Springer (Berlin), 1995.
- [113] L. M. Liz-Marzan, "Tailoring surface plasmons through the morphology and assembly of metal nanoparticles," *Langmuir*, vol. 22, no. 1, pp. 32–41, Jan 3 2006, 999SH Times Cited:609 Cited References Count:111. [Online]. Available: [iGo to ISI://WOS:000234410300009](#)
- [114] G. V. Hartland, "Optical studies of dynamics in noble metal nanostructures," *Chemical Reviews*, vol. 111, no. 6, pp. 3858–3887, Jun 2011, sp. Iss. SI 779CW Times Cited:125 Cited References Count:350. [Online]. Available: [iGo to ISI://WOS:000291756700006](#)
- [115] J. A. Schuller, E. S. Barnard, W. S. Cai, Y. C. Jun, J. S. White, and M. L. Brongersma, "Plasmonics for extreme light concentration and manipulation," *Nature Materials*, vol. 9, no. 3, pp. 193–204, Mar 2010, 557WN Times Cited:750 Cited References Count:120. [Online]. Available: [iGo to ISI://WOS:000274700900013](#)
- [116] A. Furube, L. Du, K. Hara, R. Katoh, and M. Tachiya, "Ultrafast plasmon-induced electron transfer from gold nanodots into tio2 nanoparticles," *Journal of the American Chemical Society*, vol. 129, no. 48, pp. 14 852–+, Dec 5 2007, 236HK Times Cited:149 Cited References Count:18. [Online]. Available: [iGo to ISI://WOS:000251293500010](#)
- [117] S. Mubeen, J. Lee, N. Singh, S. Kramer, G. D. Stucky, and M. Moskovits, "An autonomous photosynthetic device in which all charge carriers derive from surface plasmons," *Nature Nanotechnology*, vol. 8, no. 4, pp. 247–251, Apr 2013, 118ST Times Cited:28 Cited References Count:30. [Online]. Available: [iGo to ISI://WOS:000317046800009](#)
- [118] E. W. McFarland and J. Tang, "A photovoltaic device structure based on internal electron emission," *Nature*, vol. 421, no. 6923,

- pp. 616–618, Feb 6 2003, 642KH Times Cited:182 Cited References Count:9. [Online]. Available: [Go to ISI://WOS:000180803200037](#)
- [119] Z. Zhang and J. T. Yates, “Band bending in semiconductors: Chemical and physical consequences at surfaces and interfaces,” *Chemical Reviews*, vol. 112, no. 10, pp. 5520–5551, Oct 2012, 017YW Times Cited:54 Cited References Count:256. [Online]. Available: [Go to ISI://WOS:000309628100013](#)
- [120] H. M. Chen, C. K. Chen, C. J. Chen, L. C. Cheng, P. C. Wu, B. H. Cheng, Y. Z. Ho, M. L. Tseng, Y. Y. Hsu, T. S. Chan, J. F. Lee, R. S. Liu, and D. P. Tsai, “Plasmon inducing effects for enhanced photoelectrochemical water splitting: X-ray absorption approach to electronic structures,” *Acs Nano*, vol. 6, no. 8, pp. 7362–7372, Aug 2012, 995DU Times Cited:31 Cited References Count:59. [Online]. Available: [Go to ISI://WOS:000307988900097](#)
- [121] K. O. Aruda, M. Tagliacruzchi, C. M. Sweeney, D. C. Hannah, and E. A. Weiss, “The role of interfacial charge transfer-type interactions in the decay of plasmon excitations in metal nanoparticles,” *Physical Chemistry Chemical Physics*, vol. 15, no. 20, pp. 7441–7449, 2013, 135RL Times Cited:3 Cited References Count:79. [Online]. Available: [Go to ISI://WOS:000318306100001](#)
- [122] J. P. Spatz, S. Mssmer, C. Hartmann, M. Mller, T. Herzog, M. Krieger, H.-G. Boyen, P. Ziemann, and B. Kabius, “Ordered deposition of inorganic clusters from micellar block copolymer films,” *Langmuir*, vol. 16, no. 2, pp. 407–415, 2000. [Online]. Available: <http://pubs.acs.org/doi/abs/10.1021/la990070n>
- [123] T. Lohmueller, E. Bock, and J. P. Spatz, “Synthesis of quasi-hexagonal ordered arrays of metallic nanoparticles with tuneable particle size,” *Advanced Materials*, vol. 20, no. 12, pp. 2297–+, Jun 18 2008, 320XM Times Cited:58 Cited References Count:36. [Online]. Available: [Go to ISI://WOS:000257268500009](#)
- [124] R. Glass, M. Moller, and J. P. Spatz, “Block copolymer micelle nanolithography,” *Nanotechnology*, vol. 14, no. 10, pp. 1153–1160, Oct 2003, 738JV Times Cited:249 Cited References Count:34. [Online]. Available: [Go to ISI://WOS:000186284200016](#)
- [125] J. Szlachetko, M. Nachtegaal, E. de Boni, M. Willimann, O. Safonova, J. Sa, G. Smolentsev, M. Szlachetko, J. A. van Bokhoven, J. C. Dousse,

Bibliography

- J. Hoszowska, Y. Kayser, P. Jagodzinski, A. Bergamaschi, B. Schmitt, C. David, and A. Lucke, "A von hamos x-ray spectrometer based on a segmented-type diffraction crystal for single-shot x-ray emission spectroscopy and time-resolved resonant inelastic x-ray scattering studies," *Review of Scientific Instruments*, vol. 83, no. 10, Oct 2012, 1 043QZ Times Cited:15 Cited References Count:49. [Online]. Available: [jGo to ISI://WOS:000311562500006](http://www.isinet.org/WOS:000311562500006)
- [126] J. Szlachetko, M. Nachtegaal, J. Sa, J. C. Dousse, J. Hoszowska, E. Kleymenov, M. Janousch, O. V. Safonova, C. Konig, and J. A. van Bokhoven, "High energy resolution off-resonant spectroscopy at sub-second time resolution: (pt(acac)(2)) decomposition," *Chemical Communications*, vol. 48, no. 88, pp. 10 898–10 900, 2012, 018NF Times Cited:7 Cited References Count:35. [Online]. Available: [jGo to ISI://WOS:000309666900025](http://www.isinet.org/WOS:000309666900025)
- [127] Y. Joly, "X-ray absorption near-edge structure calculations beyond the muffin-tin approximation," *Physical Review B*, vol. 63, no. 12, pp. art. no.–125 120, Mar 15 2001, 416XW Times Cited:361 Cited References Count:30. [Online]. Available: [jGo to ISI://WOS:000167806600048](http://www.isinet.org/WOS:000167806600048)
- [128] <http://neel.cnrs.fr/spip.php?rubrique1007>.
- [129] L. Carroll, P. Friedli, P. Lerch, J. Schneider, D. Treyer, S. Hunziker, S. Stutz, and H. Sigg, "Ultra-broadband infrared pump-probe spectroscopy using synchrotron radiation and a tuneable pump," *Review of Scientific Instruments*, vol. 82, no. 6, Jun 2011, 786US Times Cited:8 Cited References Count:27. [Online]. Available: [jGo to ISI://WOS:000292334000002](http://www.isinet.org/WOS:000292334000002)
- [130] J. Sa, P. Friedli, R. Geiger, P. Lerch, M. H. Rittmann-Frank, C. J. Milne, J. Szlachetko, F. G. Santomauro, J. A. van Bokhoven, M. Chergui, M. J. Rossi, and H. Sigg, "Transient mid-ir study of electron dynamics in tio2 conduction band," *Analyst*, vol. 138, no. 7, pp. 1966–1970, 2013, 099DA Times Cited:3 Cited References Count:50. [Online]. Available: [jGo to ISI://WOS:000315598500007](http://www.isinet.org/WOS:000315598500007)
- [131] S. Mahshid, M. Askari, and M. S. Ghamsari, "Synthesis of tio2 nanoparticles by hydrolysis and peptization of titanium isopropoxide solution," *Journal of Materials Processing Technology*, vol. 189, no. 1-3, pp. 296–300, Jul 6 2007, 165SU Times Cited:60 Cited References Count:34. [Online]. Available: [jGo to ISI://WOS:000246326700040](http://www.isinet.org/WOS:000246326700040)

- [132] X. Y. Zhang, G. Smolentsev, J. C. Guo, K. Attenkofer, C. Kurtz, G. Jennings, J. V. Lockard, A. B. Stickrath, and L. X. Chen, "Visualizing interfacial charge transfer in ru-dye-sensitized tio₂ nanoparticles using x-ray transient absorption spectroscopy," *Journal of Physical Chemistry Letters*, vol. 2, no. 6, pp. 628–632, Mar 17 2011, 739AT Times Cited:17 Cited References Count:27. [Online]. Available: [iGo to ISI://WOS:000288685000021](#)
- [133] L. F. Mattheiss and R. E. Dietz, "Relativistic tight-binding calculation of core-valence transitions in pt and au," *Physical Review B*, vol. 22, no. 4, pp. 1663–1676, 1980, kg789 Times Cited:208 Cited References Count:29. [Online]. Available: [iGo to ISI://WOS:A1980KG78900018](#)
- [134] M. G. Mason, "Electronic-structure of supported small metal-clusters," *Physical Review B*, vol. 27, no. 2, pp. 748–762, 1983, qa407 Times Cited:670 Cited References Count:105. [Online]. Available: [iGo to ISI://WOS:A1983QA40700014](#)
- [135] H. Hakkinen, M. Moseler, and U. Landman, "Bonding in cu, ag, and au clusters: Relativistic effects, trends, and surprises," *Physical Review Letters*, vol. 89, no. 3, Jul 15 2002, 569JP Times Cited:375 Cited References Count:27. [Online]. Available: [iGo to ISI://WOS:000176599500014](#)
- [136] P. Zhang and T. K. Sham, "X-ray studies of the structure and electronic behavior of alkanethiolate-capped gold nanoparticles: The interplay of size and surface effects," *Physical Review Letters*, vol. 90, no. 24, Jun 20 2003, 692CM Times Cited:200 Cited References Count:24. [Online]. Available: [iGo to ISI://WOS:000183642800021](#)
- [137] R. F. Egerton, *Electron Energy-Loss Spectroscopy in the Electron Microscope*. Springer, 2011.
- [138] R. A. Ferrell, "Characteristic energy loss of electrons passing through metal foils .2. dispersion relation and short wavelength cutoff for plasma oscillations," *Physical Review*, vol. 107, no. 2, pp. 450–462, 1957, wb727 Times Cited:146 Cited References Count:22. [Online]. Available: [iGo to ISI://WOS:A1957WB72700024](#)
- [139] G. L. Hallett-Tapley, M. J. Silvero, M. Gonzalez-Bejar, M. Grenier, J. C. Netto-Ferreira, and J. C. Scaiano, "Plasmon-mediated catalytic oxidation of sec-phenethyl and benzyl alcohols," *Journal of Physical Chemistry C*, vol. 115, no. 21, pp. 10 784–10 790, Jun 2 2011, 768EQ

Bibliography

- Times Cited:16 Cited References Count:28. [Online]. Available: [Go to ISI://WOS:000290914700059](#)
- [140] N. E. Christensen, "Photoemission from au (111) and (110) - temperature effects," *Physical Review B*, vol. 20, no. 8, pp. 3205–3209, 1979, hu215 Times Cited:24 Cited References Count:24. [Online]. Available: [Go to ISI://WOS:A1979HU21500020](#)
- [141] N. E. Christensen and B. O. Seraphin, "Relativistic band calculation and optical properties of gold," *Physical Review B-Solid State*, vol. 4, no. 10, pp. 3321–+, 1971, k8526 Times Cited:357 Cited References Count:60. [Online]. Available: [Go to ISI://WOS:A1971K852600012](#)
- [142] R. Paniago, R. Matzdorf, G. Meister, and A. Goldmann, "Temperature-dependence of shockley-type surface-energy bands on cu(111), ag(111) and au(111)," *Surface Science*, vol. 336, no. 1-2, pp. 113–122, Aug 1 1995, rm715 Times Cited:174 Cited References Count:50. [Online]. Available: [Go to ISI://WOS:A1995RM71500016](#)
- [143] R. J. Ellingson, J. B. Asbury, S. Ferrere, H. N. Ghosh, J. R. Sprague, T. Q. Lian, and A. J. Nozik, "Dynamics of electron injection in nanocrystalline titanium dioxide films sensitized with [ru(4,4'-dicarboxy-2,2'-bipyridine)(2)(ncs)(2)] by infrared transient absorption," *Journal of Physical Chemistry B*, vol. 102, no. 34, pp. 6455–6458, Aug 20 1998, 117MX Times Cited:218 Cited References Count:15. [Online]. Available: [Go to ISI://WOS:000075786400002](#)
- [144] H. N. Ghosh, J. B. Asbury, and T. Q. Lian, "Direct observation of ultrafast electron injection from coumarin 343 to tio2 nanoparticles by femtosecond infrared spectroscopy," *Journal of Physical Chemistry B*, vol. 102, no. 34, pp. 6482–6486, Aug 20 1998, 117MX Times Cited:141 Cited References Count:52. [Online]. Available: [Go to ISI://WOS:000075786400007](#)
- [145] T. Berger, M. Sterrer, O. Diwald, E. Knozinger, D. Panayotov, T. L. Thompson, and J. T. Yates, "Light-induced charge separation in anatase tio2 particles," *Journal of Physical Chemistry B*, vol. 109, no. 13, pp. 6061–6068, Apr 7 2005, 912WS Times Cited:236 Cited References Count:56. [Online]. Available: [Go to ISI://WOS:000228111200006](#)
- [146] K. Takeshita, Y. Sasaki, M. Kobashi, Y. Tanaka, S. Maeda, A. Yamakata, T. Ishibashi, and H. Onishi, "Photophysics and

- electron dynamics in dye-sensitized semiconductor film studied by time-resolved mid-ir spectroscopy,” *Journal of Physical Chemistry B*, vol. 107, no. 17, pp. 4156–4161, May 1 2003, 671XR Times Cited:29 Cited References Count:36. [Online]. Available: [iGo to ISI://WOS:000182491000022](#)
- [147] O. Bram, A. Cannizzo, and M. Chergui, “Ultrafast fluorescence studies of dye sensitized solar cells,” *Physical Chemistry Chemical Physics*, vol. 14, no. 22, pp. 7934–7937, 2012, 943EB Times Cited:15 Cited References Count:36. [Online]. Available: [iGo to ISI://WOS:000304102200004](#)
- [148] K. J. Williams, C. A. Nelson, X. Yan, L. S. Li, and X. Y. Zhu, “Hot electron injection from graphene quantum dots to tio₂,” *Acs Nano*, vol. 7, no. 2, pp. 1388–1394, Feb 2013, 099KA Times Cited:3 Cited References Count:47. [Online]. Available: [iGo to ISI://WOS:000315618700057](#)
- [149] L. C. Du, A. Furube, K. Hara, R. Katoh, and M. Tachiya, “Ultrafast plasmon induced electron injection mechanism in gold-tio₂ nanoparticle system,” *Journal of Photochemistry and Photobiology C-Photochemistry Reviews*, vol. 15, pp. 21–30, Jun 2013, sp. Iss. SI 163PQ Times Cited:6 Cited References Count:110. [Online]. Available: [iGo to ISI://WOS:000320349800003](#)
- [150] R. O’Hayre, M. Nanu, J. Schoonman, and A. Goossens, “Mott-schottky and charge-transport analysis of nanoporous titanium dioxide films in air,” *Journal of Physical Chemistry C*, vol. 111, no. 12, pp. 4809–4814, Mar 29 2007, 148OI Times Cited:23 Cited References Count:40. [Online]. Available: [iGo to ISI://WOS:000245084100050](#)
- [151] L. Rassaei, M. Herrmann, S. N. Gordeev, and F. Marken, “Inter-particle charge transfer in tio₂-phytate films: Generator-collector gold-gold junction transients,” *Journal of Electroanalytical Chemistry*, vol. 686, pp. 32–37, Oct 15 2012, 065LW Times Cited:3 Cited References Count:46. [Online]. Available: [iGo to ISI://WOS:000313150800006](#)
- [152] V. K. Thorsmolle, B. Wenger, J. Teuscher, C. Bauer, and J. E. Moser, “Dynamics of photoinduced interfacial electron transfer and charge transport in dye-sensitized mesoscopic semiconductors,” *Chimia*, vol. 61, no. 10, pp. 631–634, 2007, 228FX Times

Bibliography

- Cited:21 Cited References Count:25. [Online]. Available: [Go to ISI://WOS:000250714100006](#)
- [153] Y. Chiba, A. Islam, Y. Watanabe, R. Komiya, N. Koide, and L. Y. Han, “Dye-sensitized solar cells with conversion efficiency of 11.1” *Japanese Journal of Applied Physics Part 2-Letters & Express Letters*, vol. 45, no. 24-28, pp. L638–L640, Jul 2006, 071YV Times Cited:859 Cited References Count:12. [Online]. Available: [Go to ISI://WOS:000239640700009](#)
- [154] M. K. Nazeeruddin, P. Pechy, and M. Gratzel, “Efficient panchromatic sensitization of nanocrystalline tio2 films by a black dye based on a trithiocyanato-ruthenium complex,” *Chemical Communications*, no. 18, pp. 1705–1706, Sep 21 1997, xx934 Times Cited:256 Cited References Count:7. [Online]. Available: [Go to ISI://WOS:A1997XX93400004](#)
- [155] J. C. Scaiano and K. Stampelcoskie, “Can surface plasmon fields provide a new way to photosensitize organic photoreactions? from designer nanoparticles to custom applications,” *Journal of Physical Chemistry Letters*, vol. 4, no. 7, pp. 1177–1187, Apr 4 2013, 122KR Times Cited:4 Cited References Count:77. [Online]. Available: [Go to ISI://WOS:000317317500021](#)
- [156] K. R. Li, M. I. Stockman, and D. J. Bergman, “Self-similar chain of metal nanospheres as an efficient nanolens,” *Physical Review Letters*, vol. 91, no. 22, Nov 28 2003, 747JR Times Cited:418 Cited References Count:11. [Online]. Available: [Go to ISI://WOS:000186801900049](#)
- [157] E. Hao and G. C. Schatz, “Electromagnetic fields around silver nanoparticles and dimers,” *Journal of Chemical Physics*, vol. 120, no. 1, pp. 357–366, Jan 1 2004, 757TK Times Cited:774 Cited References Count:59. [Online]. Available: [Go to ISI://WOS:000187577400045](#)
- [158] D. K. Gramotnev, D. F. P. Pile, M. W. Vogel, and X. Zhang, “Local electric field enhancement during nanofocusing of plasmons by a tapered gap,” *Physical Review B*, vol. 75, no. 3, Jan 2007, 131UJ Times Cited:50 Cited References Count:21. [Online]. Available: [Go to ISI://WOS:000243895400155](#)
- [159] N. Zhang, S. Q. Liu, X. Z. Fu, and Y. J. Xu, “Synthesis of m@tio2 (m = au, pd, pt) core-shell nanoconnposites with tunable photoreactivity,” *Journal of Physical Chemistry C*, vol. 115, no. 18,

Bibliography

- pp. 9136–9145, May 12 2011, 757ZB Times Cited:95 Cited References Count:87. [Online]. Available: [Go to ISI://WOS:000290127200036](#)
- [160] N. Zhang, S. Q. Liu, and Y. J. Xu, “Recent progress on metal core@semiconductor shell nanocomposites as a promising type of photocatalyst,” *Nanoscale*, vol. 4, no. 7, pp. 2227–2238, 2012, 909US Times Cited:51 Cited References Count:183. [Online]. Available: [Go to ISI://WOS:000301591300004](#)

Curriculum Vitae

Name: Giulia Tagliabue
Date of Birth: 21st June 1985
Place of Birth: Bologna, Italy
Citizenship: Italian

Education

04.2010-present **PhD Candidate**
at Laboratory of Thermodynamics in Emerging Technologies (LTNT), ETH Zurich, Switzerland

09.2009 **International Summer University on Renewable Energies**,
organized by *Helmholtz Zentrum Berlin* in Falera(Laax), Switzerland

09.2007-10.2009 **Master in Mechanical Engineering**
(110/110 cum laude and mention)
with major in Energy, at *University of Udine*, Italy

09.2004-10.2009 **Diploma Scuola Superiore dell'Universita' degli Studi di Udine** excellence institute to be frequented, upon admission, parallel to the standard university program. Includes additional semester courses and research projects with internal evaluation sessions.

09.2004-07.2007 **Bachelor in Mechanical Engineering**
(110/110 cum laude)
at *University of Udine*, Italy

8. Curriculum Vitae

Honors and Awards

2010	awarded as Best Master Candidate in Mechanical Engineering of the Year at <i>University of Udine</i> , Italy
02.2009	appointed the Erasmus Scholarship
2007,2008,2009	appointed the A. Rizzi Scholarship for the best student in Mechanical Engineering of each year, at <i>University of Udine</i> , Italy
09.2004	admitted at Scuola Superiore dell'Universita' degli Studi di Udine (10 available positions).

Research Experience

04.2010- <i>present</i>	PhD Candidate at Laboratory of Thermodynamics in Emerging Technologies (LTNT), ETH Zurich, Switzerland
10.2009-01.2010	Research Assistant at Laboratoire de Transfer de Chaleur et de Masse (LTCM), EPFL Lausanne, Switzerland
03.2009-09.2009	Master thesis at Laboratoire de Transfer de Chaleur et de Masse (LTCM), EPFL Lausanne, Switzerland

Teaching Experience

03.2011-08.2013	Teaching assistant bachelor courses <i>Thermodynamics I and II</i>
09.2010-03.2011	Teaching assistant master course <i>Thermodynamics of Novel Energy Conversion Technologies</i>

List of Publications

1. Three-dimensional confinement of light in deeply subwavelength gap-plasmon nanocavities - G Tagliabue, H Eghlidi, D Poulikakos - in preparation.
2. Rapid-Response Low Infrared Emission Broadband Ultrathin Plasmonic Light Absorber - G Tagliabue, H Eghlidi, D Poulikakos - submitted.
3. Tanghulu Particle Scaffolds with Extraordinary Thermal Conductivity - G. Hong, T. M. Schutzius, S. Zimmermann, B. Burg, J. Zuercher, T. Brunschweiler, G. Tagliabue, B. Michel, D. Poulikakos - submitted.

4. Proximal Gap Plasmon Nanoresonators in the Limit of Vanishing Inter-Cavity Separation - G Tagliabue, C. Holler, H Eghlidi, D Poulikakos - accepted in *Nanoscale* 2014.
5. Direct observation of charge separation on Au localized surface plasmons - G Tagliabue, J S, P Friedli, J Szlachetko, MH Rittmann-Frank, FG Santomauro, CJ Milne, H Sigg - *Energy & Environmental Science*, 6, (12), pp. 3584 – 3588, 2013.
6. Facile multifunctional plasmonic sunlight harvesting with tapered triangle nanopatterning of thin films - G Tagliabue, H Eghlidi, D Poulikakos - *Nanoscale* 5, (20), pp. 9957 – 9962, 2013
7. A micro particle shadow velocimetry (μ PSV) technique to measure flows in microchannels - S Khodaparast, N Borhani, G Tagliabue, JR Thome - *Experiments in Fluids* 54, (2), pp. 1 – 13, 2013

Conference Presentations and Posters

1. G. Tagliabue White light harvesting with a broadband plasmonic absorber Presentation at the ETH Graduate Symposium MaP (2014).
2. G. Tagliabue et al - Plasmonic Nanostructures for Improving Thin Film a:Si Solar Cell Efficiency Poster at MRS Fall Meeting 2011
3. G. Tagliabue et al - Ethanol Reforming Using Plasmonic Resonant Gold Nanoparticles: Thermocatalysis or Photocatalysis? Presentation at Symposium E, MRS Fall Meeting 2011

Patents

1. H. Eghlidi, G. Tagliabue, D. Poulikakos Thin film broadband plasmonic absorber (2013, pending)